January 2020

# First-Principles Studies Of Two-Dimensional Transition Metal Carbides For Spintronics And Energy Applications

Edirisuriya Mudalige Dilanga Siriwardane

# First-Principles Studies of Two-Dimensional Transition Metal Carbides for Spintronics and Energy Applications

by

Edirisuriya Mudalige Dilanga Siriwardane
Bachelor of Science, University of Colombo, Sri Lanka, 2011
Master of Science, Central Michigan University, USA, 2015

A Dissertation
Submitted to the Graduate Faculty
of the
University of North Dakota
in partial fulfillment of the requirements

for the degree of
Doctor of Philosophy

Grand Forks, North Dakota
August
2020

Name: Edirisuriya Mudalige Dilanga Siriwardane

Degree: Doctor of Philosophy

This document, submitted in partial fulfillment of the requirements for the degree from the University of North Dakota, has been read by the Faculty Advisory Committee under whom the work has been done and is hereby approved.

DocuSigned by:
Deniz Cakir
Name of Chairperson - Dr. Deniz Cakir

DocuSigned by:
Name of Member 2 - Dr. Nuri Oncel

DocuSigned by:
Name of Member 3 - Dr. Kanishka Marasinghe

DocuSigned by:
Name of Member 4 - Dr. Yen Lee Loh

DocuSigned by:
Mark Hoffmann
Name of Member 5 - Dr. Mark Hoffmann

This document is being submitted by the appointed advisory committee as having met all the requirements of the School of Graduate Studies at the University of North Dakota and is hereby approved.

DocuSigned by:
Chris Nelson
Chris Nelson
Dean of the School of Graduate Studies

7/13/2020
Date

# Permission

Title First-Principles Studies of Two-Dimensional Transition Metal Carbides for Spintronics and Energy Applications

Department Physics and Astrophysics

Degree Doctor of Philosophy

In presenting this dissertation in partial fulfillment of the requirements for a graduate degree from the University of North Dakota, I agree that the library of this University shall make it freely available for inspection. I further agree that permission for extensive copying for scholarly purposes may be granted by the professor who supervised my dissertation work or, in his absence, by the chairperson of the department or the dean of the Graduate School. It is understood that any copying or publication or other use of this dissertation or part thereof for financial gain shall not be allowed without my written permission. It is also understood that due recognition shall be given to me and to the University of North Dakota in any scholarly use which may be made of any material in my dissertation.

Edirisuriya Mudalige Dilanga Siriwardane
Date August, 2020

# TABLE OF CONTENTS

# LIST OF FIGURES

# LIST OF TABLES

# Acknowledgements

I would like to wholeheartedly express my gratitude to my advisor Dr. Deniz Çakır, for his continuous support on my research and for letting me explore new areas in computational material science. I am very appreciative that he had always found time to discuss the research, provide feedback and guidance.

I would like to thank my committee members Dr. Nuri Oncel, Dr. Kanishka Marasinghe, Dr. Yen Lee Loh, and Dr. Mark R. Hoffmann, for taking their time to review and evaluate this work, despite how busy their schedules were.

I would like to appreciate Dr. William Schwalm, Dr. Yen Lee Loh, Dr. Deniz Çakır, Dr. Mark R. Hoffmann, and Dr. Kathryn Thomasson for teaching me graduate-level Physics and Chemistry courses. Dr. Marasinghe, as the chair of the department, remarkably helped me since I came to UND. Dr. Oncel's group meetings were extremely helped me to enhance my oral presentation skills. Dr. Loh's guidance and encouragement always motivated me. I am very grateful to Kimberly Wickersham and the staff members, and my colleagues at the Department of Physics and Astrophysics for supporting me throughout my academic year.

I am especially thankful to UND for providing me graduate assistantships. I also want to express a special thanks to the ND EPSCoR DDA grant for providing financial support in 2018. Moreover, I'm grateful to Computational Research Center at UND, and also the Center for Nanoscale Materials (CNM) and Argonne Leadership Computing Facility (ALCF) at Argonne National Laboratory for providing computer resources.

In the end, I also want to thank our collaborators, Dr. Yen Lee Loh, Dr. Nuri Oncel and Dr. Surojit Gupta and their research groups at UND, and also Dr. Cem Sevik and his research group at Anadolu University in Turkey, Dr. François M. Peeters at the University of Antwerp in Belgium, and Dr. Rajendra P. Joshi and Dr. Neeraj Kumar at Pacific Northwest National Laboratory in the USA.

# Dedications

To my dad Sarath Siriwardena, to my mom Vinitha Perera,

and to my brother Pasindu Siriwardena,

who have always been my source of constant support and love.

# ABSTRACT

Next-generation spintronic nanoscale devices require two-dimensional (2D) materials with robust ferromagnetism. Among 2D materials, MXenes are favorable for spintronic applications due to their high electron conductivity, mobility, and chemical diversity. Since 2D materials have greater elastic strain limits than their bulk counterparts, their properties can be tuned effectively using strain engineering. In this dissertation, we discuss density functional theory (DFT) based first-principles studies on ferromagnetic MXenes for spintronics applications. In Chapter III, we investigated modifications in the structural, electronic, and magnetic properties produced by strain on 2D $Hf_2MnC_2O_2$ and $Hf_2VC_2O_2$ ferromagnetic semiconductors. The calculations in Chapter III reveal that the conduction bands near the Fermi-level are extremely sensitive to the biaxial and uniaxial strain. As a result, semiconductor-to-metal phase transitions occur at around 1-3 % biaxial compressive strain for both monolayers. At around 8-9 % biaxial tensile strain, those monolayers become half-metals. It could be shown that those results can be produced by applying uniaxial strain on Mn-based monolayer. In Chapter IV, surface defects were introduced to tune the electronic and magnetic properties of those two monolayers. Bare-$Hf_2MnC_2O_2$ nanosheet exhibits easy-plane anisotropy, whereas bare-$Hf_2VC_2O_2$ has easy-axis anisotropy. It could be found that defects change the anisotropy of Mn-based monolayer to easy-axis anisotropy. Moreover, the Curie temperature of $Hf_2MnC_2O_2H_{0.22}$ was predicted as 171 K by using the Monte Carlo simulations of the classical Heisenberg model .

Recently, extensive studies have been carried out to discover new techniques to improve the properties of the materials to meet the demand of high cycling stability, charge capacity, and energy density of rechargeable battery applications. The 2D materials have been highly investigated for energy storage due to their large surface areas, which facilitate enhanced ion adsorption. In this dissertation, several possible techniques were explored to modify the electrochemical properties of 2D battery

electrodes. Chapter V studied the B-doped-graphene (B-Gr) based systems to intercalate highly abundant Na and Mg to lower the production cost. The Na and Mg intercalated bare graphene bilayers are energetically not favorable. Nevertheless, we could show that B-Gr bilayers provide a considerable capacity (238 mAh/g for Na and 320 mAh/g for Mg). Na intercalated $T_2CO_2$/B-Gr, and B-Gr/B-Gr systems provide energy barriers as low as 0.46 and 0.18 eV, respectively. So far, hydroxyl, oxygen, and fluorine-terminated MXenes have been widely studied for energy storage applications. In Chapter VI, sulfur functionalized MXene structures (i.e., $M_2CS_2$ with M= Ti, Zr, Hf, V, Nb, Ta, Cr, Mo, and W) have been proposed as candidate materials to enhance battery performance. It was found that all the $M_2CS_2$ monolayers provide the energy barriers less than 0.22 eV for single Li adsorbed systems. Among the considered MXenes, $Ti_2CS_2$ provides the highest gravimetric capacity (417.4 mAh/g). Chapter VII introduced pillared $Ti_3C_2O_2$ bilayers for enhancing the ion storage capacity, minimizing the change in the interlayer distance between MXene layers and lowering the diffusion barrier of ions. Two different quinone molecules, namely 1,4-Benzoquinone ($C_6H_4O_2$) and Tetrafluoro-1,4-benzoquinone ($C_6F_4O_2$) were considered as the linkers between $Ti_3C_2O_2$ layers. Even though only a single Li layer can be intercalated between $Ti_3C_2O_2$ layers, quinone molecules provide enough space to store two layers of Li. Thus, high capacity can be expected. Moreover, pillared structures show a very lower diffusion barrier, which is around 0.3 eV, than that of $Ti_3C_2O_2$ bilayers without quinone molecules ($\approx$ 1.0 eV).

# CHAPTER I

# INTRODUCTION

## 1.1 Two-Dimensional Materials

Graphene is an atomically thick two-dimensional (2D) material that contains the hexagonal (honeycomb) crystal structure, as shown in Fig. 1.1 (a) and (b). A C atom contains four valence electron orbitals, which are 2s, $2p_x$, $2p_y$, and $2p_z$. The first three of them hybridized to form $sp^2$ orbitals and reside on the same plane. Those hybridized orbitals of six C atoms make $\sigma$ bonds with the nearest-neighbor atoms to form a honeycomb structure while $2p_z$ orbitals make $\pi$ bonds with each other to form a $\pi-$band.[1] Graphite is made of a large number of graphene layers that connected through van der Waals interactions. In 2004, Novoselov, Geim et al. managed to isolate graphene from graphite using mechanical exfoliation. Their groundbreaking discovery helped Andre Geim and Konstantin Novoselov to win the Nobel prize in 2010.[2–4] The $\pi$ bonds in graphene offer excellent electrical properties, while graphite shows weak electrical conductivity.

Even though graphene is the strongest material ever found and it is a good conductor, various applications of nanotechnology require 2D materials with distinct properties. As the examples, quantum computers are made of magnetic nanomaterials, but graphene does not show ferromagnetic or antiferromagnetic properties. And also, graphene cannot be used as a semiconductor, since it is a zero-bandgap material. Moreover, the centrosymmetric structure of graphene does not provide piezoelectricity. As a consequence, searching for new 2D materials with application-specific prop-

erties leads to synthesization or prediction of new monolayer materials. Among them, transition metal dichalcogenides (TMDs),[5–10] hexagonal group IV, II-IV and III-V compounds,[11] phosphorene family,[12–18] and transition metal carbides/carbonitrides (MXenes)[19] have attracted a growing research interest.

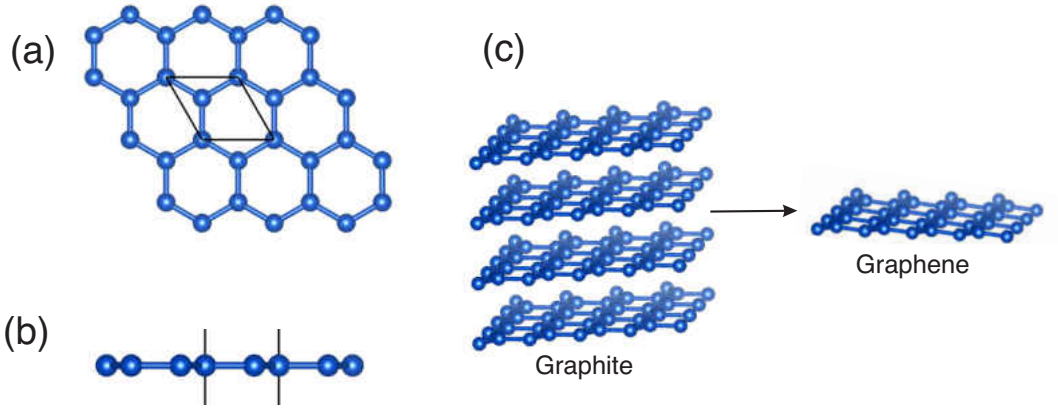


Figure 1.1: The (a) top and (b) bottom views of graphene, and (c) exfoliation of graphene using graphite.

### 1.1.1 Two-dimensional Transition Metal Carbides and Nitrides

The 2D transition metal carbides or/and nitrides (MXenes) have been vastly investigated due to their unique properties. The general formula of MXenes is $M_{n+1}X_nT_x$, where X indicates C and/or N, M is the early transition metal atoms like Sc, Ti, V, Cr, Zr and Nb, and T represents the surface termination.[20] Usually, the surfaces of those monolayers make bonds with F, O and OH due to the experimental conditions. MXenes can have three distinct formulas, namely $M_2XT_x$, $M_3X_2T_x$ and $M_4X_3T_x$, which contain two, three and four layers of transition metal atoms, respectively. $Ti_3C_2T_x$,[21] $Hf_3C_2T_x$,[22] $Ti_2CT_x$,[23] $Nb_4C_3T_x$[24] are some of the popular examples for MXenes with different number of layers. In addition to the single transition metal MXenes, stable double transition MXenes like $Hf_2MnC_2O_2$, $Hf_2VC_2O_2$, and $Ti_2MnC_2(OH)_2$ are also reported.[25]

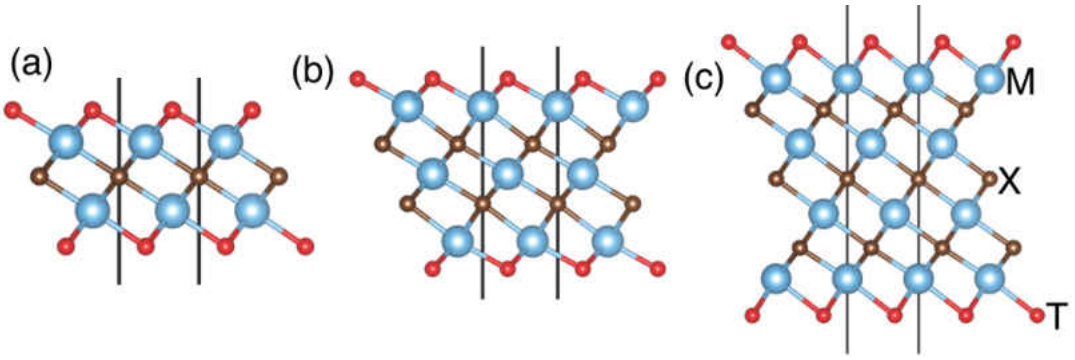


Figure 1.2: The side views of (a) $M_2XT_x$, (b) $M_3X_2T_x$ and (c) $M_4X_3T_x$ MXenes.

We selected MXenes in this research work due to the following reasons:

1. MXene metals exhibit excellent electronic conductivity[20]

2. MXenes have excellent mechanical and dynamical stability[20]

3. The electronic and magnetic properties of the MXenes can be easily tuned by various techniques like strain engineering, doping and surface modifications.[25–28]

MXene monolayers are produced by etching out A elements where A stands for group-A elements like Al, P and Ga, which are loosely bonded relative to M-X bonds in MAX phases.[29,30] MAX phases have a large family of ternary carbides and nitrides with hexagonal structure ,where space group is $P6_3/mmc$. Their general formula is $M_{n+1}AX_n$. As mentioned above, M represents an early transition metal, while X stands for C and/or N.[31] As an example, $Ti_2CO_2$ was successfully prepared from $Ti_2AlC$ phase by removing Al layers using hydrofluoric acid (HF) treatment as shown in Fig.1.3. As a result of washing out the byproducts using deionized water, $Ti_2C(OH)_2$ is produced. The chemical reactions 1.1 and 1.2 explain the production of $Ti_2C(OH)_2$ from $Ti_2AlC$. Converting $Ti_2C(OH)_2$ into $Ti_2CO_2$ was achieved by employing heat treatment.[23,32] The etching time, HF concentration, and reaction temperature vary according to the type of MAX phase during the MAX to MXene convertion.[20] As an illustration, 10% HF is required for 10 hours to produce $Ti_2CT_x$ at room temperature, while $Nb_2CT_x$ needs 50% HF for 90 hours at room

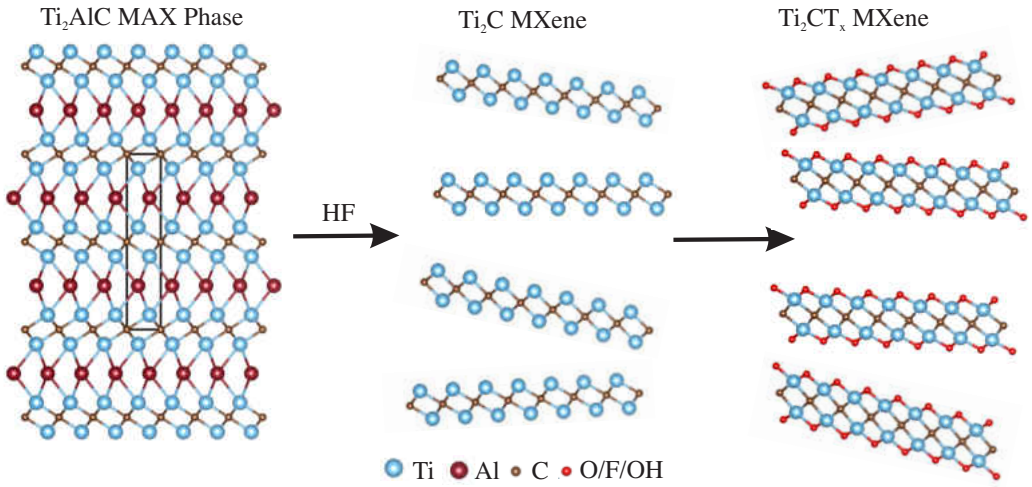


Figure 1.3: Synthesizing $Ti_2CT_x$ MXenes by selective etching using HF treatment. The side views of $Ti_2AlC$ bulk material, $Ti_2C$ MXene and $Ti_2CT_x$ MXene flakes are shown.

temperature.[31] It is also reported that ammonium hydrogen fluoride ($NH_4HF_2$) and ammonium fluoride ($NH_4F$) can be used to etching out A layers from MAX phases. For instance, $Ti_3C_2$ monolayers can be produced by applying the above solutions to the $Ti_3AlC_2$.[33–35]

$$Ti_2AlC + 3HF \rightarrow AlF_3 + \frac{3}{2}H_2 + Ti_2C \tag{1.1}$$

$$Ti_2C + 2H_2O \rightarrow Ti_2C(OH)_2 + H_2 \tag{1.2}$$

## 1.2 Two-Dimensional Materials for Spintronics Applications

The magnetic properties of materials are generated by the spin and orbital motions of the electrons. A spin creates a magnetic moment, which is approximately -9.284$\times$ $10^{-24}$ J/T. Figure 1.4 shows the density of states (DOS) distribution of the non-magnetic metals, ferromagnetic metals, and ferromagnetic half-metals at 0K temperature. Due to the Pauli exclusion principle, an orbital of an electon-shell can have

up to two electrons, and those two should have opposite spin directions (spin-up and spin-down). Since the spin-up and spin-down electrons generate the same magnetic moment with opposite directions, sum of the total magnetic moment is zero in an orbital occupied by two electrons. Hence, the filled electron shells do not contribute to magnetic properties. In non-magnetic materials, all the electron shells are filled, and the net magnetic moment is zero. Therefore, DOS of opposite spin directions are equal to each other as shown in Fig. 1.4 (a).[36] Instead, ferromagnetic (FM) materials contain partially filled electron-shells giving rise to spontaneous magnetization. To comply with the Hund's rule, unpaired electrons in partially filled electron-shells exist parallel to each other, thereby enhancing the net magnetization of FM materials. As illustrated by Fig 1.4 (c), only one type of spins in half-metals conduct, whereas the same material is an insulator or a semiconductor for the other spin orientation. In antiferromagnetic materials, half of the magnetic atoms prefer a specific spin direction and the other half is aligned in the opposite direction. Therefore, the total magnetic moment of an antiferromagnetic material is zero.

Paramagnetism is a type of magnetism where some materials produce induced internal magnetic fields by aligning their unpaired electrons in the direction of the applied magnetic field. Unlike in the ferromagnetic materials, the internal magnetic field of paramagnetic materials disappears when the external magnetic field is turned off. The Curie temperature ($T_C$) is the temperature above which magnetic materials lose their ferromagnetic properties and become paramagnetic materials. In order to keep the ferromagnetic properties of the materials in the devices, high Curie temperatures are preferred.

In spintronics, a spin degree of freedom is taken into account in addition to the charge of the electron. The current flow of classical electronic devices is manipulated by controlling the charge of the electrons. In contrast, spintronics uses the direction of spin to regulate the current flow.[37,38] As an example, giant magnetoresistance

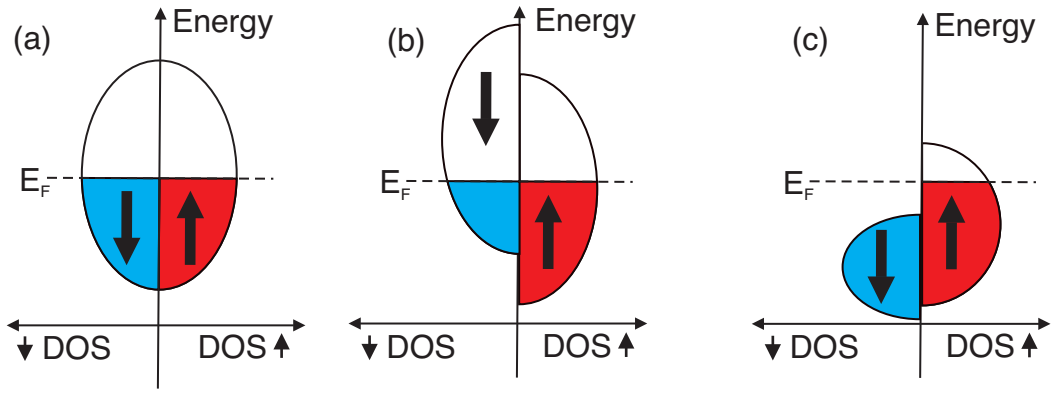


Figure 1.4: The spin-up and spin-down density of states (DOS) distribution of the (a) non-magnetic metal, (b) ferromagnetic metal and ferromagnetic half-metal at 0K temperature.[36]

(GMR) is used in spin valves to govern the devices' resistance. In spin valves, a non-magnetic conductor is sandwiched between two ferromagnetic conductors. The magnetization of the ferromagnetic layers can be parallel or antiparallel. In the case of parallel magnetization, spins parallel to the magnetization flow with low resistance(see Fig. 1.5). In contrast, the spins with opposite direction feel high resistance due to scattering inside the system. In the case of antiparallel magnetization, both spin-up and spin-down electrons scattered heavily. Thus, the resistance becomes very high.

Magnetoresistive random access memories (MRAM) contain arrays of spin-valve units. Coercivity is the resistance of a magnetic material to change the magnetization. It is the intensity of the applied magnetic field needed to decrease the magnetization of a ferromagnetic material to zero. Thus, it is hard to change the spin direction of ferromagnetic material with high coercivity. Each unit of an MRAM includes two FM layers, where one layer has high coercivity, and the other layer has low coercivity. The magnetization of the FM layer with high coercivity is fixed in a specific direction (pinned layer). Nevertheless, the direction of magnetization in the other FM layer can be altered easily (free layer). The 0-bit in a unit of MRAMs is formed by setting the magnetization of the two layers anti-parallel to each other. When both directions are parallel, 1-bit is generated.[39]

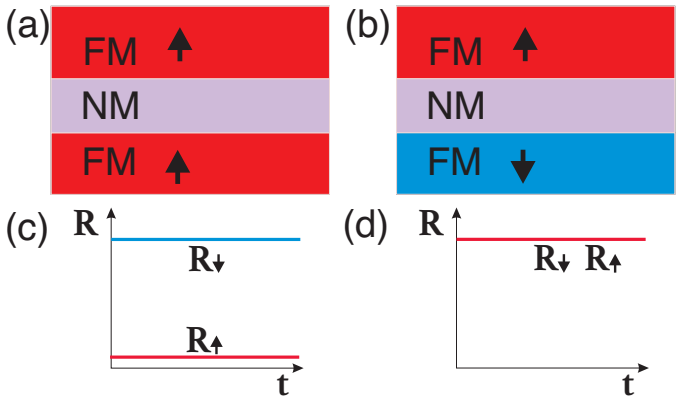


Figure 1.5: A schematic diagrams of a spin-valve where a non-magnetic metal (NM) is sandwiched between two ferromagnetic metals (FM). Here, FM materials with (a) parallel magnetization and (b) antiparallel magnetization are shown. The part (c) shows the resistances of spin-up and spin-down when magnetizations in magnets are parallel and the part (d) shows that for antiparallel case.

Another example of spintronics applications is a magnetic tunnel junction (MTJ). Instead of the nonmagnetic conductor in Fig. 1.5, an insulator is placed between the FM materials. The electrons can flow from one FM layer to the other FM layer when the thickness of the insulator is in the nano range. This phenomenon is called tunnel magnetoresistance. In MTJ, resistance is low (1), and high (0), when magnetization in two FM layers are parallel and antiparallel, respectively, as shown in Fig 1.5.[39]

Several ferromagnetic 2D materials were reported by previous research. It is theoretically predicted that MnB and $Fe_2Si$ monolayers have high Curie temperatures which are 345 and 780 K, respectively.[40] It has been reported that the double transition metal MXenes $Ti_2MnC_2(OH)_2$, $Ti_2MnC_2O_2$, $Hf_2MnC_2O_2$, and $Hf_2VC_2O_2$ are ferromagnetic monolayers. And also, the nitride MXenes $Mn_2NF_2$, $Mn_2NO_2$, $Mn_2N(OH)_2$, and $Cr_2NO_2$ have ferromagnetic groundstates.[25,41] Numerous studies have investigated modulating the magnetic properties of the $CrI_3$ monolayer which shows a long range magnetic order with a Curie temperature of 45K. Ferromagnetic-to-antiferromagnetic phase transition occurs in $CrI_3$ under tensile strain.[42] By producing $CrI_3/MoTe_2$ heterostructure, the Curie temperature increases up to around 60 K. $Fe_3GeTe_2$ is also a popular ferromagnetic monolayer which can be used to produce

$Fe_3GeTe_2$/hBN/$Fe_3GeTe_2$ magnetic tunnel junctions.

In a ferromagnetic material, the spins prefer to align in a certain crystallographic direction because the system has lower energy than when the spins arrange themself in other directions. This certain direction is called the easy axis. The spin direction, which exhibits the highest energy, is known as the hard axis. The magnetic anisotropy energy (MAE) is known as the energy required to divert the magnetic moment in a crystal from the easy to the hard axis of magnetization. High MAE is preferred since the energy required for demagnetization is large when the MAE is significant.[43] $CrI_3$,[44] $Fe_3GeTe_2$,[45] and $VSe_2$[45]monolayers exhibit 686, 920, 594 $\mu$eV relatively high MAE values, respectively.

## 1.3 Two-Dimensional Materials for Energy Storages

Rechargeable Lithium ion-batteries are extremely popular due to the high usage of portable devices in day-to-day life. As a solution to environmental pollution, electric cars are manufactured with rechargeable power sources. Figure 1.6 shows a schematic diagram of a battery made out of 2D materials. The batteries consist of two electrodes, namely anode (negative electrode) and the cathode (positive electrode), and also an electrolyte that is placed between the two electrodes. The ions in the rechargeable energy storages act as the energy carriers that flow from anode to cathode through the electrolyte during the discharging process. While the ions move inside the battery, the electrons flow from the anode to cathode through an electronics/electrical device that is connected to the battery from outside.[46]

The dominant anode material for the Lithium ion-batteries is graphite, while that for the cathode is $LiCoO_2$.[46] Despite its low cost and high capacity, these electrodes are suffering from reduced cycling rates and low electrical conductivity. Thus, finding novel materials for enhancing the properties of electrodes is a critical concern in the battery industry.

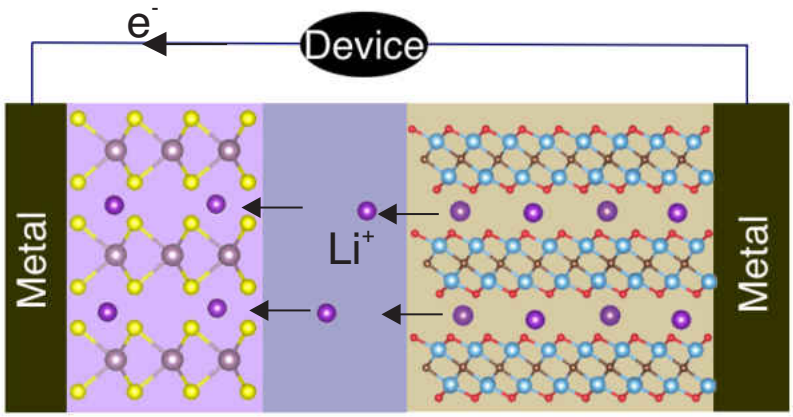


Figure 1.6: The schematic for showing ion and electron flows of a 2D battery made of 2D materials during the discharging process.

2D materials exhibit a larger surface area and a higher number of active sites for ion absorption compared to their bulk counter parts. Consequently, nanosheets are able to improve the capacity of the ion-storage devices. Reduced ion transport distances in 2D materials are helpful for fast ion diffusion kinetics, which is essential for batteries. Moreover, reduced volume change as compared to 3D counterparts (such as Si) during the charging/discharging process in 2D materials enhances the mechanical and electrochemical stability and cycle lifetime.[46–50] 2D materials like graphene, transition metal dichalcogenides (TMDs), transition metal oxides (TMO), early transition metal carbides and nitrides (MXenes) and phosphorene have been extensively investigated as electrodes for energy storage devices.[33,49–53]

MXenes have been specially utilized in energy storage and conversion applications such as lithium ion batteries and super-capacitors due to their favorable electronic properties.[20,54] $Ti_3C_2T_x$ is the first ever introduced MXene which was synthesized in 2011.[21] It is also the most investigated MXene as the electrode for ion-storage because $Ti_3C_2T_x$ free standing paper capacitors contain excellent volumetric capacitance around 350 $Fcm^{-3}$. $Ti_3C_2T_x$ nanosheets' outstanding volumetric capacitance,

which was proved by X-ray absorption spectroscopy studies,[20,33,55] surpasses the capacitance of ion-storage made of carbon double layers. Furthermore, it is compatible with the capacitance of activated graphene electrodes.[33] The density of carrier of $Ti_3C_2T_x$ was found as $8 \pm 3 \times 10^{21}$ $cm^{-3}$ and it's conductivity and mobility were determined as 2140 $Scm^{-1}$ and $0.7 \pm 0.2$ $cm^2$, respectively.[56] $Ti_2CT_x$ MXenes are the lightest MXenes available. Due to the light weight, $Ti_2CT_x$ MXenes exhibits 1.5 times higher gravimetric capacity for Li ions than that of $Ti_3C_2T_x$, even though both materials have the same surface chemistry.[33] It is reported that $Nb_4C_3T_x$ MXenes anodes offer 380 $mAhg^{-1}$ gravimetric capacity for Li at a current density 0.1 $Ag^{-1}$ after 100 cycles, while $Hf_3C_2T_x$ anodes provide 146 $mAhg^{-1}$ gravimetric capacity for Li at $200mAg^{-1}$ after 200 cycles.[56]

# CHAPTER II

# METHODOLOGY

## 2.1 The Many-Body Hamiltonian

The Hamiltonian for a material can be presented as a sum of Hamiltonians of nuclei ($\hat{H}_{\mathrm{n}}$) and electrons ($\hat{H}_{\mathrm{e}}$), and the potential energy due to interaction between electrons and nuclei ($\hat{V}_{\mathrm{en}}$) as shown in Eq. 2.1. $\hat{H}_{\mathrm{n}}$ and $\hat{H}_{\mathrm{e}}$ are formed with the kinetic energies ($T_{\mathrm{e}}$ and $T_{\mathrm{nuc}}$) and Coulomb interaction between electrons ($V_{\mathrm{ee}}$) and Coulomb interactions between nuclei ($V_{\mathrm{nn}}$) for a system with N number of nuclei and n number of electrons, as illustrated in Eq. 2.3 and 2.2.

$$\hat{H} = \hat{H}_{\mathrm{n}} + \hat{H}_{\mathrm{e}} + \hat{V}_{\mathrm{en}} \tag{2.1}$$

$$\hat{H}_{\mathrm{n}} = T_{\mathrm{n}} + V_{\mathrm{nn}} = -\sum_{i}^{N} \frac{h^2}{2M_i} \nabla^2_{\mathbf{R}_i} + \frac{1}{2} \sum_{i}^{N} \sum_{j,i\neq j}^{N} \frac{Z_i Z_j e^2}{|\mathbf{R}_i - \mathbf{R}_j|} \tag{2.2}$$

$$\hat{H}_{\mathrm{e}} = T_{\mathrm{e}} + V_{\mathrm{ee}} = -\sum_{i}^{N} \frac{h^2}{2m} \nabla^2_{\mathbf{r}_i} + \frac{1}{2} \sum_{i}^{n} \sum_{j,i\neq j}^{n} \frac{e^2}{|\mathbf{r}_i - \mathbf{r}_j|} \tag{2.3}$$

$$\hat{V}_{\mathrm{en}} = -\frac{1}{2} \sum_{i}^{N} \sum_{j}^{n} \frac{Z_i e^2}{|\mathbf{R}_i - \mathbf{r}_j|} \tag{2.4}$$

Born-Oppenheimer approximation neglects the motion of nuclei since the mass of nuclei is more than 1000 times greater than that of electrons. Thus, nuclei are considered as static particles and the total Coulomb interaction force between nuclei

is a constant. As a result, we can drop the kinetic energy of nuclei from the total Hamiltonian and compute the nuclear-nuclear interaction energy classically. Hence, the multi-electron Hamiltonian can be simplified to Eq. 2.5. $\hat{V}_{\text{en}}$ potential acts an external potential for electrons.[57]

$$\hat{H} = -\sum_{i}^{N} \frac{h^2}{2m} \nabla^2_{\mathbf{r}_i} - \frac{1}{2} \sum_{i}^{N} \sum_{j,i \neq j}^{n} \frac{Z_i e^2}{|\mathbf{R_i} - \mathbf{r_j}|} + \frac{1}{2} \sum_{i}^{n} \sum_{j,i \neq j}^{n} \frac{e^2}{|\mathbf{r}_i - \mathbf{r}_j|} \tag{2.5}$$

## 2.2 Hartree-Fock Theory

In a material with N number of electrons, there is a $3N$ number of degrees of freedom. A Solid contains a large number of electrons (around $10^{23}$). In order to solve the Schrödinger equation, the computers should solve $3N$ number of simultaneous equations. Currently, the computers are not capable of handling such a large number of systems of equations. Hartree-Fork theory consider the electrons as non-interacting particles. The Schrödinger equation of an electron can be written as in Eq. 2.6. Therefore, instead of considering $3N$ number of degrees of freedom for solving the Schrödinger equation, computers are able to compute the energy of the electron and wavefunction by using only 3 degrees of freedom.[57]

$$[-\frac{h^2}{2m} \nabla^2_{\mathbf{r}_i} + V_{\text{eff}(\mathbf{r})}] \psi_i(\mathbf{r}) = \epsilon_i \psi_i \tag{2.6}$$

$V_{\text{eff}}(\mathbf{r})$ is the effective potential which can be written as Eq. 2.7. The first term of the expression is the potential due to interaction between a given electron and the rest of the electrons of the solid. That was derived from the mean-field theory. The second term represents the external potential on an electron. The last term is the exchange interaction between the electrons. The electron density can be determined as $\rho_{i'}(\mathbf{r}') = \sum_i |\psi_{i'}|^2$.[57]

$$V_{\text{eff}}(\mathbf{r}) = \int \frac{e^2 \rho_{i'}(\mathbf{r}')}{|\mathbf{r} - \mathbf{r}'|} d\mathbf{r}' - \sum_j \frac{Z_j e^2}{|\mathbf{R_j} - \mathrm{r}|} - \sum_i [\int \frac{e^2 \psi_i^*(\mathbf{r}') \psi_{i'}(\mathbf{r}')}{|\mathbf{r} - \mathbf{r}'|}] d\mathbf{r}' \qquad (2.7)$$

Hartree-Fork theory provides an approximated solution to the many-body Schrödinger equation, where the total wavefunction ($\Psi$) can be given by a single Slater determinant of Spin-Orbitals ($\psi_i$). The example in Eq. 2.8 provides the Slater determinant of N number of electrons. As the Pauli exclusion principle suggests, the wavefunction of a fermion should be antisymmetric. The Slater determinant satisfies the antisymmetric property of the wavefunction.[57]

$$\Psi = \frac{1}{\sqrt{N!}} \begin{vmatrix} \psi_1(\mathbf{r}_1) & \psi_1(\mathbf{r}_2) & \cdots & \psi_1(\mathbf{r}_N) \\ \psi_1(\mathbf{r}_2) & \psi_2(\mathbf{r}_2) & \cdots & \psi_2(\mathbf{r}_N) \\ \vdots & \vdots & \ddots & \vdots \\ \psi_N(\mathbf{r}_1) & \psi_N(\mathbf{r}_2) & \cdots & \psi_N(\mathbf{r}_N) \end{vmatrix} \qquad (2.8)$$

The electrons avoid each other due to the Coulomb repulsion, and it affects the position of each electron. The Hartree-Fock method does not take into account the Coulomb correlation. Therefore, its solution does not provide the exact ground state energy of the system.[58] Thus, density functional theory was introduced with both exchange and correlation potentials to enhance the accuracy of the calculations.

## 2.3 Density Functional Theory

### 2.3.1 The Hohenberg-Kohn Theorems

Theorem 1: The external potential ($V_{\text{ext}}$ or $V_{\text{en}}$) can be determined uniquely by the ground state electron density ($\rho(\mathbf{r})$).[59]

Thus, we can write the total energy of a system as

$$E[\rho] = T[\rho] + E_{ee}[\rho] + E_{ne}[\rho] = F_{\mathrm{HK}}[\rho] + \int \rho(\mathbf{r}) V_{\mathrm{ext}}(\mathbf{r}) d\mathbf{r} \tag{2.9}$$

Here, the universal functional $F_{\mathrm{HK}}[\rho]$ is defined as $F_{\mathrm{HK}}[\rho] = T[\rho] + E_{ee}[\rho]$. The explicit form of $T[\rho]$ is unknown. And also, only the classical part of $E_{ee}[\rho]$, that is the Coulomb interaction between the electrons, is known. Thus, non-classical contribution ($E_{ncl}[\rho]$) is yet to be found.

$$E_{ee}[\rho] = \frac{e^2}{2} \int \int \frac{\rho(\mathrm{r})\rho(\mathrm{r}')}{|\mathbf{r} - \mathbf{r}'|} d\mathbf{r} d\mathbf{r}' + E_{ncl}[\rho] \tag{2.10}$$

Theorem 2: The variational principle provides ground state for $E[\rho]$, if and only if the input electron density $\rho(\mathbf{r}')$ is the true ground state density.[59]

Therefore, the total energy of a system is a upper bound for a trial electron density $\rho'$, if that is not the ground state density ($\rho$) as shown in Eq. 2.11

$$E[\rho'] = F_{\mathrm{HK}}[\rho'] + \int \rho'(\mathbf{r}) V_{\mathrm{ext}}(\mathbf{r}) d\mathbf{r} \geq E_0[\rho] \tag{2.11}$$

### 2.3.2 The Kohn-Sham equations

As explained before, the universal functional can be written as follows.

$$F[\rho] = T[\rho] + J[\rho] + E_{ncl}[\rho] \tag{2.12}$$

Since the expressions for kinetic and the non-classical energy terms are unknown, we are not able to directly use Eq 2.10. Instead, W. Kohn and L.J. Sham proposed that electrons can be treated as non-interacting particles and kinetic term can be written for N number of electrons as in Eq. 2.13 with wavefunctions of individual electrons ($\psi_i$).[60]

$$T_s = -\frac{\hbar^2}{2m}\sum_i^N \int \psi_i^* \nabla^2 \psi_i d\mathbf{r} \tag{2.13}$$

Since $T_S$ does not represent the true kinetic energy term and $E_{\text{ncl}}$ is unknown, they introduced the exchange-correlation energy ($E_{\text{XC}}$) as follows.[60]

$$E_{\text{XC}}[\rho] = (T[\rho] - T_S[\rho]) + E_{ncl}[\rho] \tag{2.14}$$

Khon-Sham equation is defined as the Schrödinger equation with single electron wave-function as illustrated by Eq. 2.15, where energy eigenvalue is denoted by $\epsilon_i$.

$$(-\frac{\hbar^2}{2m}\nabla^2 + V_{\text{ext}}(\mathbf{r}) + \frac{e^2}{2}\int \frac{\rho(\mathrm{r}')}{|\mathbf{r}-\mathbf{r}'|}d\mathbf{r} + \frac{\delta E_{\text{XC}}}{\delta\rho})\psi_i = \epsilon_i\psi_i \tag{2.15}$$

The total energy of a system can be written as follows using the Kohn–Sham density functional theory[60] .

$$E = -\frac{\hbar^2}{2m}\sum_i^N \int \psi_i^* \nabla^2 \psi_i d\mathbf{r} + \int V_{\text{ext}}(\mathbf{r})\rho(\mathbf{r})d\mathbf{r} + \frac{e^2}{2}\int\int \frac{\rho(\mathrm{r})\rho(\mathrm{r}')}{|\mathbf{r}-\mathbf{r}'|}d\mathbf{r}d\mathbf{r}' + E_{\text{XC}}[\rho] \tag{2.16}$$

### 2.3.3 Exchange-Correlation Functional

In order to calculate the ground state energy using Eq. 2.16, we want to approximate the exchange-correlation functional ($E_{\text{XC}}[\rho]$). Two of the well known methods in use are the local density approximation (LDA)[61] and the generalized gradient approximation (GGA).[62] In the LDA, it is assumed that $E_{\text{XC}}[\rho(\mathbf{r})]$ at the position $\mathbf{r}$ is equal to the energy due to the uniform electron gas which has the same density at $\mathbf{r}$. As a result, $E_{\text{XC}}[\rho(\mathbf{r})]$ can be written as

$$E_{\mathrm{XC}}[\rho(\mathbf{r})] = \int \rho(\mathbf{r})\epsilon_{\mathbf{XC}}^{LDA}[\rho(\mathbf{r})]d\mathbf{r} \tag{2.17}$$

Here, $\epsilon_{\mathbf{XC}}$ is the exchange-correlation energy per electron of the homogeneous electron gas. This expression was derived by considering the density of the electron in solid (inhomogeneous system) does not vary rapidly. The system can be split into small boxes with volume $d^3\mathbf{r}$. Thus, each box has a homogenous electron density which is equal to the local density $\rho(\mathbf{r})$ at the position $\mathbf{r}$. By multiplying the exchange-correlation energy per electron ($\epsilon_{\mathbf{XC}}$) and number of electrons at the position $\mathbf{r}$ ($\rho(\mathbf{r})d\mathbf{r}$), we can calculate the total exchange-correlation energy at a given $\mathbf{r}$. Integrating over the whole space gives us the total exchange-correlation energy ($E_{\mathrm{XC}}[\rho(\mathbf{r})]$). Monte Carlo simulations can be used to compute $\epsilon_{\mathbf{XC}}$ as a function of $\rho(\mathbf{r})$.[63]

One of the major disadvantages of the LDA method is that binding energy error is around 20% overestimation. This is too significant for chemical reaction calculations. The atomization energy of molecules is overestimated with large errors by LDA. For instance, the atomization energy of $CH_4$ and CO were predicted with 10.3 and 15.3 %, respectively.[63] Moreover, LDA underestimates the bond lengths and lattice parameters. As an example, LDA predicts the lattice constant of Si with 1.87% underestimation.[64] As a solution, the GGA method was introduced. With this method, we consider the gradients of the charge density in addition to $\rho(\mathbf{r})$ as follows:[63]

$$E_{\mathrm{XC}}[\rho(\mathbf{r})] = \int \rho(\mathbf{r})\epsilon_{\mathbf{XC}}^{GGA}[\rho(\mathbf{r}), \nabla\rho(\mathbf{r}]d\mathbf{r} \tag{2.18}$$

There are several popular GGA methods in use. One of the widely used GGA methods is the Perdew–Burke–Ernzerhof (PBE), which significantly lowers the atomization error of the molecules. The atomization energies of $CH_4$ and CO were estimated with 1.8% and 3.7% overestimations, which are much lower than the errors

produced by LDA, as explained before. The PBE method overestimates the lattice parameters and bond lengths with small errors. For Si, the lattice parameter is estimated with a 0.7 % error, which is a considerable improvement compared to the error produced by the LDA method.[64] But, it should be noted that PBE almost always overestimates the lattice constants. In order to lower the error, alternative GGA methods were introduced. Some of the methods are PBEsol,[65] AM05,[66] and WC.[67] The lattice parameter of Si was estimated by PBEsol, AM05, and WC with 0.16, 0, and 0.20 % underestimations, which are exceedingly lower than the errors from the LDA and PBE methods.[64]

## 2.4 Spin Density Functional Theory

The spin of each electron can be taken into account to describe the total electron density ($\rho$) with $\alpha$- and $\beta$-spins as mentioned in the following expression.[68]

$$\rho(\mathbf{r}) = \sum_{i}^{N} \int |\psi(\mathbf{r_1}, s_1, \mathbf{r_2}, s_2 ..... \mathbf{r}_N, s_N)|^2 d\mathbf{r_1} ds_1 .... d\mathbf{r}_N ds_N \tag{2.19}$$

If we replace $\mathbf{r_1}$ with a position $\mathbf{r}$ and $s_1$ with $s_{\alpha_1} = \frac{1}{2}$ and $s_{\beta_1} = -\frac{1}{2}$, it can be shown that $\rho(\mathbf{r})$ can be given as a sum of the electron densities of majority ($\rho_\alpha$) spins and minority ($\rho_\beta$) spins as follows.

$$\begin{aligned} \rho(\mathbf{r}) =& N \int |\psi(\mathbf{r}, \frac{1}{2}, \mathbf{r_2}, s_2 ..... \mathbf{r}_N, s_N)|^2 d\mathbf{r_2} ds_2 .... d\mathbf{r}_N ds_N \\ &+ N \int |\psi(\mathbf{r}, -\frac{1}{2}, \mathbf{r_2}, s_2 ..... \mathbf{r}_N, s_N)|^2 d\mathbf{r_2} ds_2 .... d\mathbf{r}_N ds_N \\ =& \rho_\alpha(\mathbf{r}) + \rho_\beta(\mathbf{r}) \end{aligned} \tag{2.20}$$

The spin density ($\Lambda(\mathbf{r})$) of a system is the difference between $\rho_\alpha$ and $\rho_\beta$ at a particular position $\mathbf{r}$ as shown in Eq. 2.21, where we use the Pauli matrix in z direction

($\sigma_z = \left(\begin{smallmatrix} 1 & 0 \\ 0 & -1 \end{smallmatrix}\right)$) to derive the expression.

$$\begin{aligned}\Lambda(\mathbf{r}) =& N \int \psi^*(\mathbf{r}, s_1, ...\mathbf{r}_N, s_N)\sigma_z(s_1)\psi(\mathbf{r}, s_1, ...\mathbf{r}_N, s_N)d\mathbf{r_2}ds_2....d\mathbf{r}_N ds_N \\ =& \rho_\alpha(\mathbf{r}) - \rho_\beta(\mathbf{r})\end{aligned} \tag{2.21}$$

The integrals of $\rho_\alpha(\mathbf{r})$ and $\rho_\beta(\mathbf{r})$ with respect to the volume provide the number of $\alpha$ ($N_\alpha$) and $\beta$ ($N_\beta$) electrons as $N_\alpha = \int \rho_\alpha(\mathbf{r})d^3(\mathbf{r})$ and $N_\beta = \int \rho_\beta(\mathbf{r})d^3(\mathbf{r})$.[68] Thus, the total magnetic moment ($M$) can be calculated as follows,

$$M = \frac{1}{2}\int \Lambda(\mathbf{r})d^3(r) = \frac{1}{2}(N_\alpha - N_\beta) \tag{2.22}$$

To generalize the Hohenberg-Kohn theorems for a system with $\alpha$ and $\beta$ electrons, external potential can be written as a function of both $\rho_\alpha$ and $\rho_\beta$. Thus, we can rewrite Eq. 2.11 for the ground state energy $E_0[\rho_\alpha, \rho_\beta]$ with ground state densities $\rho_\alpha$ and $\rho_\beta$ as,

$$E[\rho'_\alpha, \rho'_\beta] = F_{HK}[\rho'_\alpha, \rho'_\beta] + \int (\rho'_\alpha + \rho'_\beta)V_{\text{ext}}d(\mathbf{r}) \geq E_0[\rho_\alpha, \rho_\beta], \tag{2.23}$$

where $\rho'_\alpha$ and $\rho'_\beta$ are arbitrary densities for $\alpha$ and $\beta$ electrons, respectively. The total wavefunction is given by the Slater determinant $\Psi = |\psi_1^\alpha\chi_\alpha, \psi_1^\beta\chi_\beta, \psi_2^\alpha\chi_\alpha, \psi_2^\beta\chi_\beta.....|$, where $\chi$ represents the spin eigenfunctions. Finally, the Kohn-Sham equations in Eq. 2.15 can be rewritten as given in Eq. 2.24.

$$\begin{aligned}(-\frac{\hbar^2}{2m}\nabla^2 + V_{\text{ext}}(\mathbf{r}) + \frac{e^2}{2}\int \frac{\rho_\alpha(\mathrm{r}')}{|\mathbf{r} - \mathbf{r}'|}d\mathbf{r} + \frac{\delta E_{\text{XC}}}{\delta\rho_\alpha})\psi_i^\alpha =& \epsilon_i\psi_i^\alpha \\ (-\frac{\hbar^2}{2m}\nabla^2 + V_{\text{ext}}(\mathbf{r}) + \frac{e^2}{2}\int \frac{\rho_\beta(\mathrm{r}')}{|\mathbf{r} - \mathbf{r}'|}d\mathbf{r} + \frac{\delta E_{\text{XC}}}{\delta\rho_\beta})\psi_i^\beta =& \epsilon_i\psi_i^\beta\end{aligned} \tag{2.24}$$

## 2.5 Implementation of Density Functional Theory

### 2.5.1 The Bloch Theorem

The periodicity of a crystal lattice allows us to consider a periodic potential $V(\mathbf{r})$ with a translation vector $\mathbf{T}$ of the lattice as $V(\mathbf{r}) = V(\mathbf{r} + \mathbf{T})$. According to Bloch theorem, the wavefunction ($\psi_k(\mathbf{r})$) of a Schrödinger equation with the periodic potential can be given by

$$\psi_k(\mathbf{r}) = e^{i\mathbf{k}\cdot\mathbf{r}} u_k(\mathbf{r}), \tag{2.25}$$

where $u(\mathbf{r})$ is a periodic function with same periodicity $\mathbf{T}$ and $\mathbf{k}$ is the wave vector. Therefore, $u_k(\mathbf{r})$ can be written as $u_k(\mathbf{r}) = u_k(\mathbf{r} + \mathbf{T})$. Due to the periodicity of $u_k(\mathbf{r})$, it is useful to write it as a Fourier series,

$$u_k(\mathbf{r}) = \sum_G u_G e^{i\mathbf{G}\cdot\mathbf{r}}, \tag{2.26}$$

where $\mathbf{G}$ represent a set of reciprocal space vectors, which satisify $\mathbf{G} \cdot \mathbf{T} = 2\pi n$. Thus, we can use Eq. 2.25 and 2.26 to show that

$$\psi_k(\mathbf{r}) = \sum_G u_{G+k} e^{i(\mathbf{G}+\mathbf{k})\cdot\mathbf{r}}. \tag{2.27}$$

The eigenstates of the Hamiltonian are periodic in k-space. Therefore, for any vector $\mathbf{G}$ in reciprocal space,

$$\psi_k(\mathbf{r}) = \psi_{k+G}(\mathbf{r}). \tag{2.28}$$

As a result, all the wavefunctions of a lattice with periodic potential can be generated by considering the first Brillouin zone.[69–71] Kinetic energy cutoff ($E_{\text{cut}}$) of the Bloch functions is given by the $E_{\text{cut}} = \frac{\hbar^2}{2m}|k + G_{\text{cut}}|$, where $G_{\text{cut}}$ is the cutoff vec-

tor in reciprocal space. A sufficient $E_{\text{cut}}$ value should be provided to expand the wavefunctions within the Brillouin zone.

### 2.5.2 Brillouin Zone Sampling

In density functional theory, calculating various periodic functions like charge density are computed by integrating over the first Brillouin zone (see Fig. 2.30).[72] We assume that a periodic function $F(\mathbf{k})$ can be written as a Fourier series,

$$F(\mathbf{k}) = \sum_{j=1}^{m} F_j e^{i(\mathbf{k}\cdot\mathbf{R}_j)}, \tag{2.29}$$

To solve the integrations computationally, we replace $\frac{1}{\Omega_{\text{BZ}}}\int_{\text{BZ}}$ with a weighted sum over a large number of k-points as follows,

$$I = \frac{1}{\Omega_{\text{BZ}}}\int_{\text{BZ}} F(\mathbf{k})d\mathbf{k} = \sum_{\mathbf{k}} \omega_{\mathbf{k}} \sum_{j=1}^{m} F_j e^{i(\mathbf{k}\cdot\mathbf{R}_j)}. \tag{2.30}$$

The lowest Fourier component $F_0$ can be obtained by integrating over the whole Brillouin zone. In order to make it computationally possible, it should be approximated by a finite sum over k-points. Since the summation is carried out only up to $\mathbf{R_m}$, a discretization error depends on vanishing the Fourier components beyond $j = m$. Even though the calculations related to semiconductors and insulators can be done with high accuracy with the above method, there can be a high discretization error for metals since electron occupancy alters rapidly near the Fermi level. To minimize the error, we use special $k-$points set using Monkhorst and Pack[73] method as,

$$\begin{aligned} \mathbf{k}_{pqr} =& s_p\mathbf{b_1} + s_q\mathbf{b_2} + s_r\mathbf{b_3}, \\ s_p =& \frac{(2p - N_p - 1)}{2N_p}, \end{aligned} \tag{2.31}$$

where $b_i$ are the reciprocal lattice vectors while $N_p$ is the number of k points in $p$ direction.

We define symmetrized plane-waves as $A_j(\mathbf{k}) = \sum e^{i(\mathbf{k}\cdot\mathbf{R}_j)}$ and rewrite Eq. 2.30 with special number of $k-$points $(N)$ as,

$$I = \frac{1}{\Omega_{\mathrm{BZ}}} \int_{\mathrm{BZ}} F(\mathbf{k}) d(\mathbf{k}) = \sum_{i=1}^{N} \omega_{\mathbf{k}_i} F(\mathbf{k}_i) + \sum_{m=M+1}^{\infty} \sum_{i=1}^{N} \omega_{\mathbf{k}_i} F_m A_m(\mathbf{k}_i) = F_0. \qquad (2.32)$$

We solve this by finding a set of weights $(\omega_{\mathbf{k}_i})$ to satisfy $\sum_i w_i A(\mathbf{k}) = 0$. Thus, the higher terms $(m \geq M)$ vanishes. That is a reasonable assumption since the $F_m$ term decreases while $m$ increases, and it gradually becomes negligible.[72,74–77]

### 2.5.3 Pseudopotential Approximation

The pseudopotential is used as an approximated effective potential to replace all-electronic potential (real potential) in a way that pseudo-wavefunction can be represented by a significantly fewer number of Fourier components compared to the all-electron wavefunction (real wavefunction). The wavefunctions of the valence electrons are orthogonal to that of core electrons. The all-electron wavefunctions of valence electrons oscillate rapidly in the core region to comply with the orthogonality condition. As a result, there should be a substantial basis set to represent the wavefunctions in the core region, as can be seen in Fig. 2.1. In the pseudopotential approximation, the core orbitals are considered to be frozen, since the chemically active electrons exist only in the valence region. As a result, pseudopotential wavefunctions do not contain any node within the core region. Thus, a small basis set is enough due to the reduced number of electrons and the smooth curve of the pseudo-wavefunction. Beyond the cutoff radius, $\mathrm{R}_c$, which separates the core and valence regions, all-electron and pseudo- wavefunctions are identical, as illustrated by Fig 2.1.[78]

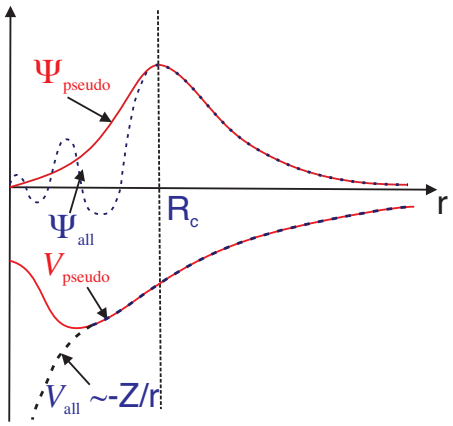


Figure 2.1: Schematic illustration of wavefunctions and their effective potentials. The pseudo-wavefunction ($\Psi_{\text{pseudo}}$) and pseudopotential ($V_{\text{pseudo}}$) are indicated by red lines. The all-electron wavefunction ($\Psi_{\text{all}}$) and potential ($V_{\text{all}}$) are represented by blue doted lines. The vertical doted line presents the cutoff radius ($\text{R}_\text{c}$).[79]

The pseudopotentials are classified according to the degree of hardness. When the required number of Fourier components is high, a pseudopotential is recognized as hard. Otherwise, it is considered soft. A high (low) cutoff energy is required for hard (soft) pseudopotentials. One of the well known members of the hard category is Norm-conserving pseudopotential. Norm-conserving pseudopotentials satisfy the norm conservation; i.e. $\int_o^{\text{R}_c} |\Psi_{\text{all}}|^2 d\text{r} = \int_o^{\text{R}_c} |\Psi_{\text{pseudo}}|^2 d\text{r}$.[79] Due to the high cutoff energy value required for norm-conserving potentials, the computations become time-consuming. As a solution, softer pseudopotentials are required. Ultra-soft pseudopotential (USP)[80] is one of the most popular soft pseudopotentials. The wavefunctions of USP in the core are formed with the smallest possible basis in order to make the calculations fast. Another popular pseudopotential is the projected augmented wave (PAW) method,[81,82] which provides higher accuracy than the USP approach. The following are the main two reasons for the high accuracy of the PAW approach.[74–77]

1. The smaller radial cutoffs than that of UPS are used in PAW.

2. PAW is able to reconstruct the exact wavefunctions with all the nodes in the core region.

## 2.6 Climbing Image Nudged Elastic Band Method

The energy barrier of the ions on a surface of the electrodes in this dissertation was found based on the climbing image nudged elastic band (CI-NEB) method. When an ion moves from one site to another, it chooses a minimum energy path (MEP). For MEP, there can be a saddle point which has the highest energy, as shown in Fig 2.3. That is also known as transition state ($x^{\dagger}$), which has energy $E^{\dagger}$. The transition rate for an ion which starting from an initial point at the local potential minimum (site A) and moving through a saddle point and ends at another site (site B) is given by Eq. 2.33, where $E^{\dagger}$ is the energy of the saddle point, $E^{\text{int}}$ is the energy at the initial state, $v_i$ are the normal mode frequencies, and $v_i^{\dagger}$ are the normal mode frequencies at the saddle point.[83,84]

$$k_{A\to B} = \frac{\prod_i^{3N} v_i^{\text{int}}}{\prod_i^{3N} v_i^{\dagger}} e^{-(E^{\dagger}-E^{\text{int}})/k_B T} \tag{2.33}$$

The above quantities can be calculated at zero temperature. The effects due to entropy can be included based on harmonic approximation. In the regular nudged elastic band (NEB) method, we consider several moments of the same ion/atom placed on the path. Those moments are known as images. The nearby images are connected with each other using elastic springs. The force acting on the images lie on the MEP is only pointing along the path. The forces applied perpendicular to the MEP is zero. The saddle points of the MEP have the maximum energy. MEP can have multiple minima in addition to the initial and finale states[83,84]

In order to comply with the above requirements, the forces applied perpendicular to the path is calculated, as $\mathbf{F}^{\perp} = -\nabla E(\mathbf{R}_i)^{\perp}$, based on the energy on the surface (see Fig 2.2). Here, $\mathbf{R}_i$ denotes the position of $i^{\text{th}}$ image of the elastic band. The forces parallel to the path is calculated using the parallel component of the force applied by the spring (i.e., $\mathbf{F}^{\parallel}_{i,\text{spring}}$). Thus, only the spring forces manage the spacing between

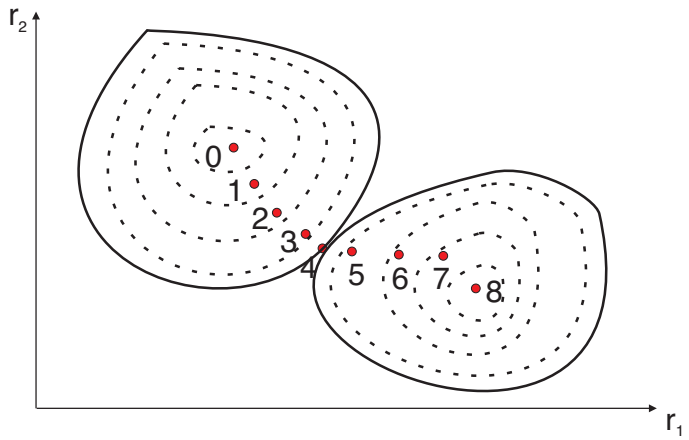


Figure 2.2: Schematic diagram of a 2D energy surface is shown in the figure. Here, red dots represent the positions of images, dotted lines are the energies lower than the energy of the transition state, and the solid lines represent the energy of transition state. The transition state is at location number 4.

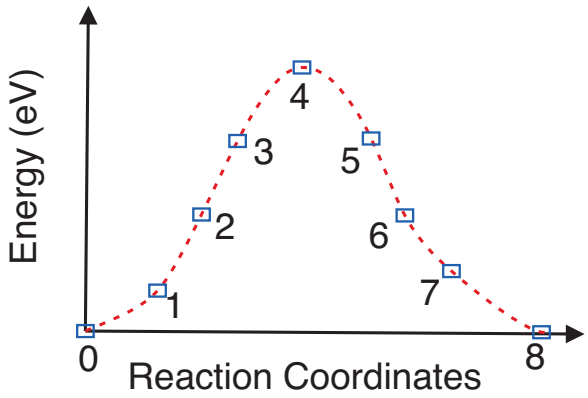


Figure 2.3: Energy as a function of reaction coordinates from CI-NEB method for the schamtic illustration in Fig. 2.2.

the images which are positioned on the MEP. When the image $i$ is located on the MEP, $\mathbf{F}^{\perp} = -\nabla E(\mathbf{R}_i)^{\perp} = 0$.

The total force acting on an image can be given by

$$\mathbf{F}_i = \mathbf{F}^{\parallel}_{i,\text{spring}} - \nabla E(\mathbf{R}_i)^{\perp}. \tag{2.34}$$

The perpendicular component based on true force can be calculated using

$$\nabla E(\mathbf{R}_i)^{\perp} = \nabla E(\mathbf{R}_i) - \nabla E(\mathbf{R}_i) \cdot \hat{\tau}, \tag{2.35}$$

where, $\hat{\tau}$ is the unit vector parallel to the tangent at $i^{th}$ image. The parallel component of the force applied by a spring with spring constant, $k$, can be determined based on

$$\mathbf{F}^{\parallel}_{i,\text{spring}} = k(|\mathbf{R}_{i+1} - \mathbf{R}_i| - |\mathbf{R}_i - \mathbf{R}_{i-1}|)\hat{\tau}. \tag{2.36}$$

The saddle point of the MEP is calculated by employing interpolation. In the case of having a narrow energy barrier, there can be several images near the saddle point. As a result, interpolation can be inaccurate for finding the saddle point. To minimize this error, the climbing image NEB was introduced. First, the regular NEB method will be performed for several iterations and will find the image with maximum energy ($i_{\text{max}}$). Then, the force on that image is calculated based on

$$\mathbf{F}_i = -\nabla E(\mathbf{R}_i) + 2(\nabla E(\mathbf{R}_{i_{\text{max}}}) \cdot \hat{\tau}_{i_{\text{max}}})\hat{\tau}_{i_{\text{max}}}. \tag{2.37}$$

Therefore, the image with maximum energy is independent of the other images and their springs. The above expression allows the climbing image to move up along the elastic band and move down the true potential surface. CI-NEB and NEB are carried out using iterative minimization. The optimization of MEP is done based on the velocity Verlet algorithm.[83,84]

# CHAPTER III

# ENGINEERING STRAIN OF $Hf_2MC_2O_2$ (M=Mn,V) MXenes

## 3.1 Introduction

Introducing approaches to control the magnetic states in the robust ferromagnetic materials is crucial in quantum information devices.[41,85] Strain engineering can be effectively applied to 2D materials due to the high elastic strain limits of nanosheets as compared to their bulk counterparts.[85–87] Strain engineering has been exploited to tune numerous properties of 2D materials like graphene, transition metal dichalcogenides (TMDs), MXenes, and phosphorene.[85,87–93] Enhanced magnetic moments have been observed in T-$VS_2$[90] and $WTe_2$[94] TMDs and also in $Ti_2C$ and $V_2N$ MXenes[95] under biaxial tensile strain. It has been reported that ferromagnetism in Li-doped $TiO_2$ nanosheets can be tuned via uniaxial strain.[96]

The double transition metal MXenes are synthesized using $M_2M'AX_2$ MAX phases which were first discovered by Liu *et al.* by introducing $Cr_2TiAlC_2$. In those structures, M′ transition metal is sandwiched between two transition metal carbide (M-C) layers.[97,98] Anasori *et al.* predicted more than 20 stable double-M MXenes with $M_2M'C_2$ and $M_2M'_2CX_2$ structures using density functional theory (DFT).[97] It is found that the electronic and magnetic properties of those double-M MXenes can be manipulated employing different surface terminations. As an example, even though $Hf_2MnC_2O_2$ is a ferromagnetic semiconductor with a high Curie temperature,

$Hf_2MnC_2(OH)_2$ is an antiferromagnetic metal while $Hf_2MnC_2F_2$ is an antiferromagnetic semiconductor, respectively.[25] It is reported that $Hf_3C_2O_2$ MXenes were synthesized successfully,[99] and also manipulating the electrical conductivity of those materials were theoretically investigated.[22]

In this research work, the main motivation behind choosing the $Hf_2MnC_2O_2$ and $Hf_2VC_2O_2$ 2D materials is that the both monolayers show the semiconductor and ferromagnetic characteristics simultaneously. According to the spin polarized DFT calculations, both materials posse high Curie temperatures greater than 800 K, which are well above the room temperature. This indicates that those nanosheets are promising materials for spintronic applications.[25]

## 3.2 Computational Methods

Density functional theory based first principle calculations were performed employing Projected Augmented Wave (PAW) method[81,82] as implemented in Vienna *ab initio* Simulation Package (VASP).[74–77] Perdew-Burke-Ernzerhof (PBE)[100,101] pseudo potentials in Generalized Gradient Approximation (GGA) method was used to include the Exchange-Correlation potential. A plane wave basis set with energy threshold value of 400 eV was considered in the calculations. The energy convergence criteria was set to $10^{-6}$ eV and the force convergence criteria for the ionic steps is set to $10^{-2}$ eV/Å. A vacuum space of around 20 Å was used in order to avoid the interaction between neighboring sheets. The Brillouin zone integration for the unit cell was performed using a Gamma-centered $12 \times 12 \times 1$ Monkhorst-Pack $k$-mesh. A very dense $k$-mesh of $24 \times 24 \times 1$ was used for Density of States (DOS) calculations. The strong correlations of the unfilled $d$ orbitals in the transition metals of the two monolayers were taken into account using the on-site coulomb potential U.[102] The U potentials were taken from the previous work done by Dong *et al.* for Hf, Mn and V as 2, 4 and 3 eV, respectively.[25] The spin polarized calculations were carried out

to investigate the properties of ferromagnetic and anti-ferromagnetic phases, where a $2 \times 1$ super-cell is considered for the latter phases. The validity of our calculations were verified by performing HSE06[103] calculations for the selected systems. Both DFT+U and HSE06 predict the same magnetic ground state. The elastic constant calculations were carried out by employing density functional perturbation theory (DFPT) as implemented in VASP.[104]

## 3.3 Biaxial Strain Effects on $Hf_2MnC_2O_2$ and $Hf_2VC_2O_2$ 2D Materials

### 3.3.1 Strain and Structure

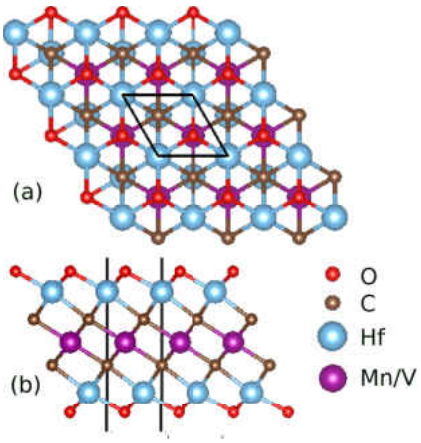


Figure 3.1: (a) Top and (b) side views of $Hf_2MnC_2O_2$ and $Hf_2VC_2O_2$ 2D materials.

$Hf_2MnC_2O_2$ and $Hf_2VC_2O_2$ double transition metal MXenes have hexagonal structure with space group P-32/m1. Figure 3.1 shows that Mn and V atoms sandwiched between two O-Hf-C layers. The GGA+U calculations provide that these monolayers have ferromagnetic ground state and unstrained structure lattice constant for $Hf_2MnC_2O_2$ is 3.253 Å and that for $Hf_2VC_2O_2$ is 3.224 Å, in a good agreement with literature.[25] The biaxial strain applied was calculated employing $\frac{(a-a_0)}{a_0}$, where $a_0$ and $a$ are the unstrained and strained lattice constants, respectively. Here, a negative

value indicates compressive strain, while a positive value is used for tensile strain. These hexagonal unit-cells consist two Hf atoms and one Mn or V atom. While tensile strain is applied, the angle made by these three atoms decreases as shown in Fig. 3.2. On the contrary, compressive strain increases the angles. This is mainly due to the Poisson's effect, which compresses (expands) the system in out of plane direction when a tensile (compressive) strain is applied in the in-plane direction. It is worth noticing that all bond lengths increase (decrease) with tensile (compressive) strain. The higher slopes of Mn-C and V-C bond length curves relative to that of other bonds in Fig. 3.2 implies that strain effects on those Mn-C and V-C bonds are significant than other bonds. These kind of structural changes highly influence on the electronic and magnetic properties as discussed in the sections 3.3.2 and 3.3.3.

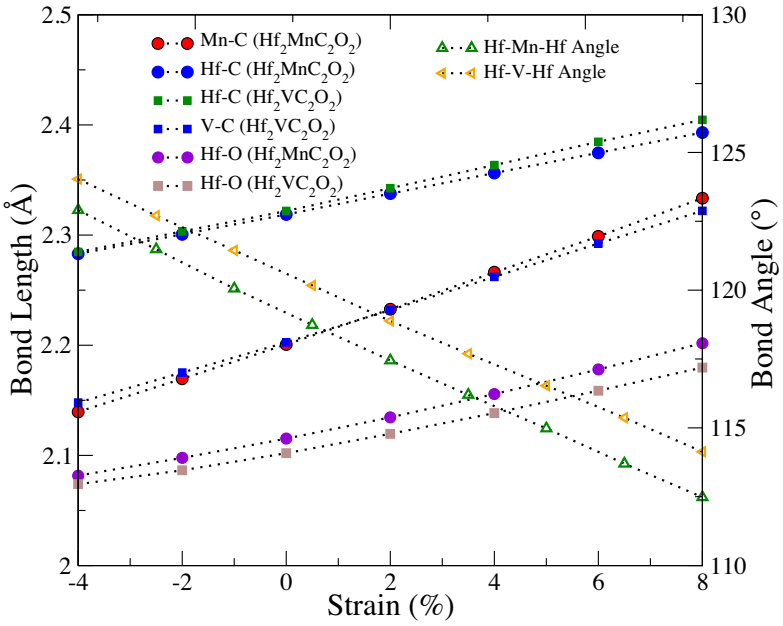


Figure 3.2: Variation of bond angles and lengths as a function of biaxial strain.

To determine the elastic limits of the both materials, stress was calculated as a function of biaxial strain by employing the equation $\sigma = \frac{1}{2V_0}\frac{\partial E}{\partial \epsilon}$, where $E$ is the total energy, $V_0$ is the volume of the strain-free monolayer and $\epsilon$ is the biaxial strain.[105] It is obtained that $Hf_2MnC_2O_2$ and $Hf_2VC_2O_2$ are able to sustain stress values up to 54.6

GPa and 56.2 GPa, respectively as shown in Fig. 3.3(b). The corresponding critical biaxial tensile strain values calculated from maximum stress values are about 17% and 13%, respectively. At the critical strain, the calculated stress reaches its maximum value and starts to decrease with further increase of strain. The surface Young's modulus ($Y_{2D}$) and the Poisson's ratios ($\mu$) of a hexagonal 2D structure can be determined using the elastic constants according to the relation, $Y_{2D} = (C_{11}^2 - C_{12}^2) / C_{11}$, where $C_{11}$ and $C_{12}$ are the elastic constants, which represent longitudinal compression and transverse expansion. Since the both monolayers has a considerable thickness (t), we converted the surface Young's modulus ($Y_{2D}$) into a more conventional form using $Y_{3D} = Y_{2D}/t$.[86] In oder to calculate the layer thickness (t), multilayer configurations (see Fig. A4 in Appendices) with van der Waals interactions, which is implemented by DFT-D3 with Becke-Jonson damping, is considered.[106,107] The thickness is calculated as the monomer thickness,[22] which are 8.94 Å for Mn based monolayer and 9.28 Å for V based monolayers. $C_{11}$ and $C_{12}$ values for $Hf_2MnC_2O_2$ are 388.2 GPa and 87.6 GPa, respectively. Those values obtained for $Hf_2VC_2O_2$ are 402.4 GPa and 107.6 GPa, respectively. Thus, the calculations show that the elastic modulus, $Y_{3D}$, for $Hf_2MnC_2O_2$ is 368.5 GPa while it is calculated as 373.6 GPa for $Hf_2VC_2O_2$. The Young's modulus of those two monolayers are considerably higher than that of well-known 2D materials such as MoS2 with 270,[108] WS2 with 270,[108] $Ti_3CT_x$ (T is the surface termination) with 330 ± 30 GPa[109] and graphene oxide with 200 GPa.[110]

The in-plane Poisson's ratio ($\nu$) for the hexagonal structure was calculated according to the expression $\nu = C_{12}/C_{11}$.[86] It was found that $\nu$ is 0.22 for $Hf_2MnC_2O_2$ and 0.26 for $Hf_2VC_2O_2$. The out of plane Poisson's ratio ($\nu_\perp$) can be given by the equation $\nu_\perp = -(\Delta t / t) / (\epsilon_{11} + \epsilon_{22})$. Here, $\Delta t$, $\epsilon_{11}$ and $\epsilon_{22}$ are the change of layer thickness, strain in zigzag and armchair directions, respectively.[111] The $\nu_\perp$ is calculated by averaging the obtained values under the uniaxial strains between -1% and 1% in armchair and zigzag directions on the rectangular supercell (see Fig. A3 in

Appendices). It is found that both $Hf_2VC_2O_2$ and $Hf_2MnC_2O_2$ has the same $\nu_\perp$ value (0.38).

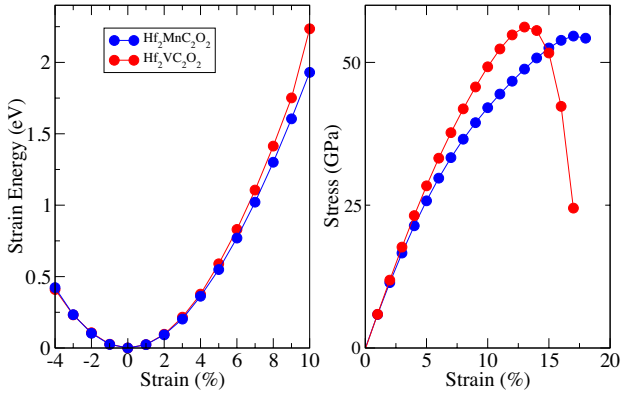


Figure 3.3: (a) Strain energy and (b) stress as function of strain. Strain energy is the difference between total energy of the strained monolayer and strain free monolayer.

### 3.3.2 Electronic Properties

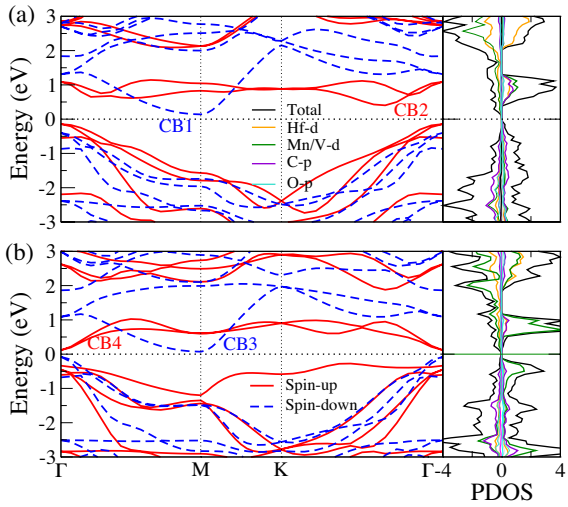


Figure 3.4: Electronic band structures and Density of States (DOS) of unstrained (a) $Hf_2MnC_2O_2$ and (b) $Hf_2VC_2O_2$ 2D materials. Fermi energy marks zero energy.

Next, we discussed the electronic properties as a function of applied biaxial strain. As can be seen in Fig. 3.4(a), unstrained $Hf_2MnC_2O_2$ is an indirect band gap ferromagnetic semiconductor with a band gap of 0.282 eV, where the conduction band minimum (CBM) and the valence band maximum (VBM) are at the Γ and M points,

respectively. Our value is slightly ($\sim$ 0.045 eV) greater than the published data.[25] It is clear that the two lowest conduction bands of $Hf_2MnC_2O_2$ shift towards either lower or higher energies depending on type and size of strain (Fig. 3.5). For simplicity, these two bands are named as CB1 and CB2. These bands together with VBM are mainly originated from Hf and Mn -*d* and C-*p* orbitals. As is expected, HSE06 calculations provides a larger band gap of 0.484 eV. CBM and VBM are located at the same positions as obtained from DFT+U calculations (See Fig. A2 and TABLE A1 in Appendices). Comparing the band structures calculated using different functionals, apart from band gap values, DFT+U and HSE06 give very similar band structures. However, DFT calculations with GGA compute very different band structures and lower magnetic moments. Due to self-interaction error, DFT-GGA calculations tend to predict metallic behaviors (See Fig. A1 and TABLE A1 in Appendices).

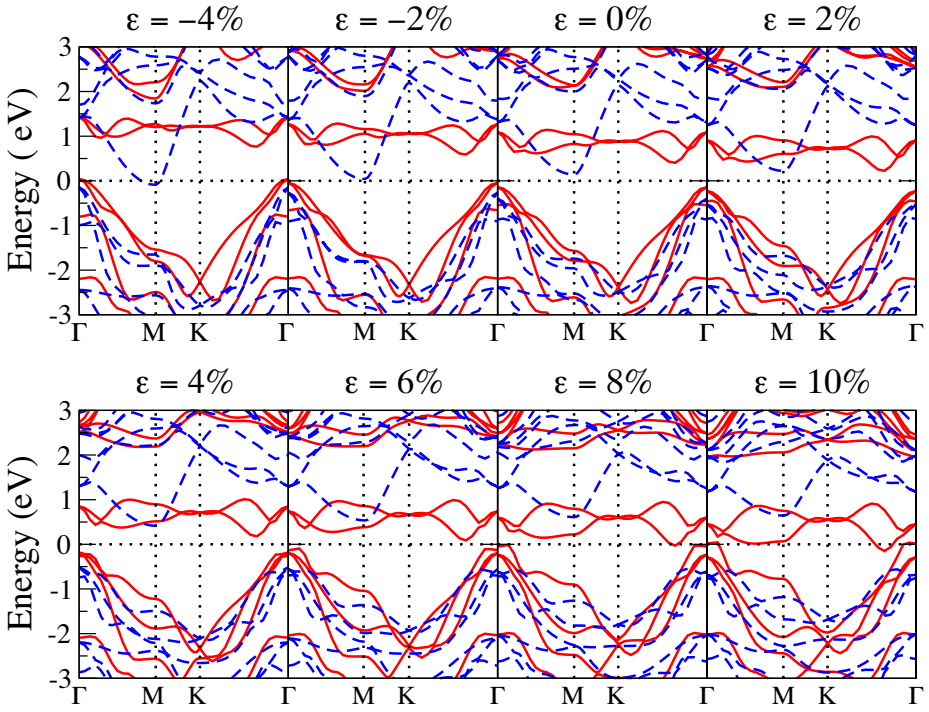


Figure 3.5: The calculated spin-resolved band structure of $Hf_2MnC_2O_2$ for different biaxial strain values. The red and blue lines represent the spin-up and spin-down bands, respectively.

As the tensile strain is increased, CB1 (CB2) shifts to higher (lower) energies.

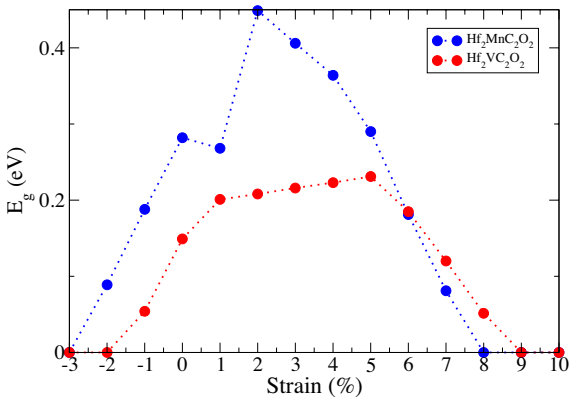


Figure 3.6: Variation of band gap as a function of strain

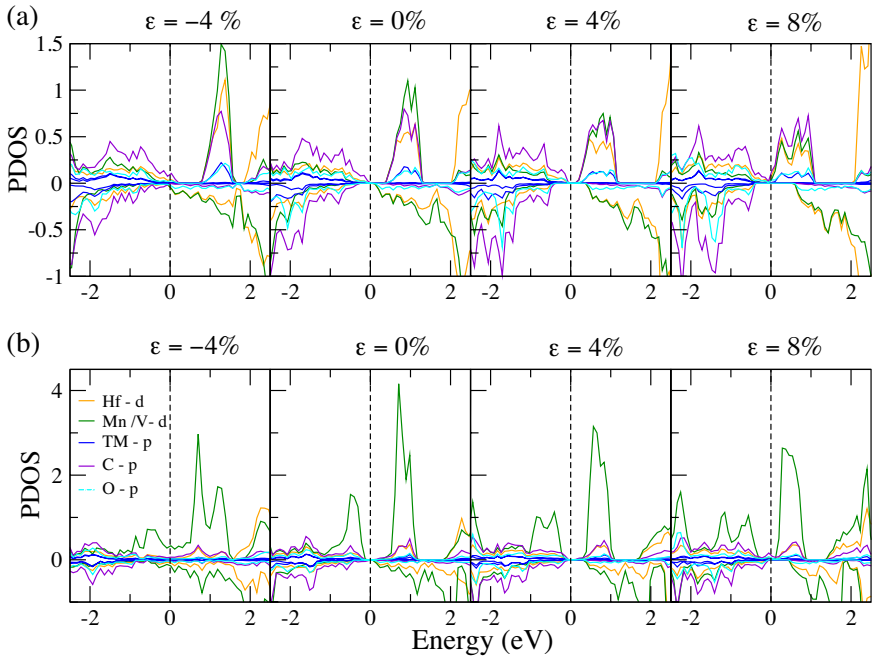


Figure 3.7: Partial Density of States (PDOS) for (a) $Hf_2MnC_2O_2$ and (b) $Hf_2VC_2O_2$ monolayers with -4% , 0%, 4% and 8% biaxial strains. Fermi energy marks zero energy.

As a result of tensile strain, CBM position starts to appear between K and Γ points. Competition between CB1 and CB2 determine the band gap. When the tensile strain $\leq$ 2%, band-gap rises due to the shifting of CB1 to higher energy levels. Henceforth, band gap diminishes, since the CB2 band moves downward, and eventually crosses the Fermi level for the larger tensile strain values (Figs. 3.5 and 3.6). At a strain of 8%, $Hf_2MnC_2O_2$ becomes a semi-metal, since the VBM and CBM touches the

Fermi-level. After strain of 8%, a semiconductor to metal transition occurs (Fig. 3.5). Figure 3.2 indicates that Hf-Mn-Hf angle becomes narrower with tensile strain, whereas Hf-C and Mn-C bond lengths stretch. Hence, the tensile strain enhances the coupling between the transition metal (TM)-*d* orbitals, while weakening the coupling of TM-*d* and C-*p* orbitals. While a compressive strain is applied, Hf-Mn-Hf bond angle increases and Hf-C and Mn-C bond lengths decrease. This allows the TM-*d* orbitals to couple weakly, although C-*p* orbitals couple with TM-*d* orbitals strongly. The band gap of $Hf_2MnC_2O_2$ becomes smaller owing to decrease of the CB1 band energy and increase of higher valence band energy. These bands start crossing the Fermi-level when the compressive strain is around -4%. Our calculations obtained using HSE06 also provide zero band gap for -4% strain while larger band gap (0.665 eV) at 4% strain where DFT+U provides 0.268 eV band gap (see TABLE A1 in Appendices).

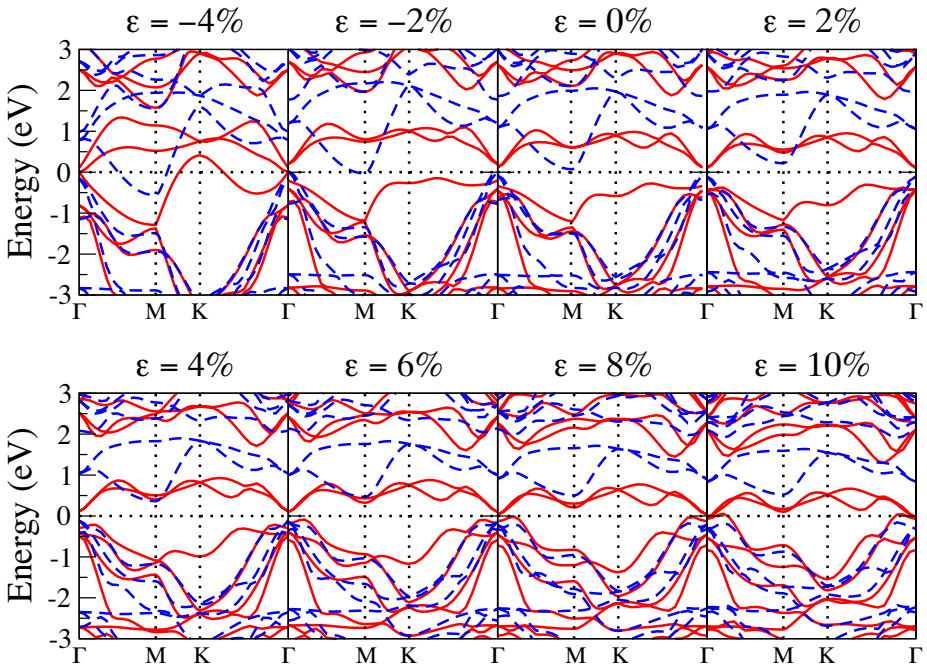


Figure 3.8: The calculated spin-resolved band structure of $Hf_2VC_2O_2$ for different biaxial strain values. The red and blue lines represent the spin-up and spin-down bands, respectively.

Table 3.1: The charge transfer $\Delta q$ for each atom are mentioned for strained and unstrained $Hf_2MnC_2O_2$ and $Hf_2VC_2O_2$ 2D materials.

| Material | Property | -4% | -2% | 0% | 2% | 4% |
|---|---|---|---|---|---|---|
| $Hf_2MnC_2O_2$ | $\Delta q_{Hf}$(e) | 3.948 | 3.949 | 3.948 | 3.948 | 3.936 |
| | $\Delta q_{O}$(e) | -1.999 | -2.003 | -2.014 | -2.030 | -2.017 |
| | $\Delta q_{C}$(e) | -2.737 | -2.717 | -2.686 | -2.652 | -2.632 |
| | $\Delta q_{Mn}$(e) | 1.564 | 1.535 | 1.489 | 1.453 | 1.426 |
| $Hf_2VC_2O_2$ | $\Delta q_{Hf}$(e) | 3.948 | 3.944 | 3.924 | 3.941 | 3.951 |
| | $\Delta q_{O}$(e) | -1.995 | -1.998 | -1.991 | -2.014 | -2.032 |
| | $\Delta q_{C}$(e) | -2.936 | -2.916 | -2.896 | -2.877 | -2.862 |
| | $\Delta q_{V}$(e) | 1.951 | 1.924 | 1.915 | 1.900 | 1.883 |

The unstrained $Hf_2VC_2O_2$ is an indirect band gap semiconductor with a small band gap of 0.15 eV while HSE06 provides 0.422 eV gap. The VBM and the CBM are at the Γ and M points, respectively. Two lowest conduction bands are named as CB3 and CB4 as shown in Fig. 3.4(b). CB3 energy band is mainly formed by TM-*d* orbitals, whereas V-*d*, Hf-*d* and C-*p* states are hybridized to form the CB4 energy band. Not like CB2 in the band structure of $Hf_2MnC_2O_2$, CB4 does not shift much. The HSE06 calculations also confirm this behavior as shown in Fig. A2 in Appendices. At 2% compressive strain, this material becomes a half metal, where spin-down states cross the Fermi level, although spin-up states make a 0.34 eV band gap. It is clear that the semiconductor to metal transition occurs when a compressive strain is applied. On the contrary, tensile strain enhances the band gap until a strain of 2%. Then, the band gap remains between 0.2 eV and 0.3 eV up to 6%. When biaxial strain exceeds 6%, the band gap starts to decreases and disappears at around 9% tensile strain. Valence band crosses the Fermi-level at around 9% tensile strain, which converts $Hf_2VC_2O_2$ into a half metal. Both HSE06 and DFT+U studies show that $Hf_2VC_2O_2$ become a metal under small compressive strain. But, HSE06 always provide higher band gap values. For instance, 0.422 eV and 0.630 eV are obtained for 0% and 4% strains, respectively (see TABLE A2 in Appendices).

Our calculations also show that strain engineering can be exploited to switch the

order of spin-up and spin-down bands. For instance, while spin-down electrons in CB1 band of $Hf_2MnC_2O_2$ dominate the conduction at 0% strain, a tensile strain of 4% makes the spin-up electrons main charge carriers for conduction. This suggests that by controlling strain over a $Hf_2MnC_2O_2$ based spintronic device, we can tune, for instance, magnetoresistance.

Table 3.2: The hole ($m_h^*$) and electron ($m_e^*$) effective masses in units of free electron mass ($m_0$) in $\Gamma - M$ (M), $\Gamma - K$ (K) and $M - K$ (L) directions under tensile strain for $Hf_2MnC_2O_2$ and $Hf_2VC_2O_2$ monolayers. And also, the conduction band which is used to calculate the $m_e^*$ values are mentioned.

| Material | Strain(%) | $m_{hM}^*$ | $m_{eM}^*$ | $m_{hK}^*$ | $m_{eK}^*$ | $m_{hL}^*$ | $m_{eL}^*$ |
|---|---|---|---|---|---|---|---|
| $Hf_2MnC_2O_2$ | 0 | 1.10 | $2.19_{CB1}$ | 0.95 | $1.16_{CB2}$ | 0.67 | $0.30_{CB1}$ |
| | 2 | 0.94 | $2.34_{CB1}$ | 0.84 | $1.09_{CB2}$ | 0.58 | $0.36_{CB1}$ |
| | 4 | 0.89 | $2.21_{CB2}$ | 0.97 | $0.91_{CB2}$ | 0.48 | $0.35_{CB1}$ |
| | 6 | 0.56 | $2.45_{CB2}$ | 0.50 | $0.51_{CB2}$ | 0.46 | $1.34_{CB2}$ |
| $Hf_2VC_2O_2$ | 0 | 0.45 | $2.46_{CB3}$ | 0.37 | $0.54_{CB4}$ | 1.93 | $0.28_{CB3}$ |
| | 2 | 0.93 | $0.43_{CB4}$ | 0.84 | $0.51_{CB4}$ | 2.04 | $0.34_{CB3}$ |
| | 4 | 0.89 | $0.28_{CB4}$ | 0.97 | $0.49_{CB4}$ | 1.40 | $0.37_{CB3}$ |
| | 6 | 0.56 | $0.47_{CB4}$ | 0.55 | $0.32_{CB4}$ | 0.87 | $0.90_{CB4}$ |

The Bader charge analysis are carried out to study the effect of strain on the charge transfer between the each type of chemical species in both monolayers.[112] TABLE 3.1 reveals that the transition metals lose charge, whereas O and C gain due to their higher electronegativity than that of transition metal atoms. Mn atom loses less charge as compared to V. In unstrained systems, there is a difference of around 0.5 $e^-$ between $\Delta q_{Mn}$ and $\Delta q_V$. And also, C in $Hf_2VC_2O_2$ acquires more charge than that of C in $Hf_2MnC_2O_2$. This indicates that there is a higher charge transfer between V and C than Mn and C. This partially explains the higher mechanical stability of $Hf_2VC_2O_2$ as compared to $Hf_2MnC_2O_2$. As tensile strain is applied, Mn and V (C) lose (gain) less charge as a result of increasing Mn-C bond lengths. However, compressive strain shortens these bond lengths. Consequently, $\Delta q_{Mn}$, $\Delta q_V$ and $\Delta q_C$ increase. It is interesting that $\Delta q_{Hf}$ and $\Delta q_O$ variations are negligible in both tensile and compressive strain cases.

$$\vec{m}^* = \hbar^2 (\frac{\partial^2 E}{\partial k^2})^{-1} \vec{e}_{\vec{k}} \tag{3.1}$$

The effective mass ($m^*$) is calculated using Eq. 3.1 where the derivatives are taken along $\vec{k} = k\vec{e}_{\vec{k}}$. $m^*$ is calculated at the band edges along the particular directions. According to this simple expression, the effective mass is inversely propositional to the band curvature. $m^*$ of electrons and holes along the $\Gamma-$M, $\Gamma-$K and M$-$K directions are studied for both unstrained and strained monolayers, which exhibit semiconductor properties. It was found that the tensile strain can be exploited to modify the effective masses (TABLE 3.2). For electrons, this is due to applying external strain that can be used to switch the energy order of CB1 and CB2 bands of $Hf_2MnC_2O_2$ and also CB3 and CB4 bands of $Hf_2VC_2O_2$, changing electrical conductance accordingly. The subscript M, K and L in TABLE 3.2 indicate the $\Gamma-$M, $\Gamma-$K and M$-$K directions, respectively. The electron effective masses of both unstrained materials in the M$-$K direction are less than half of the values of that in the $\Gamma-$M direction. This is mainly because CB1 and CB3 are more flat in the $\Gamma-$M direction as compared to that in the M$-$K direction. Since CBMs of both materials are at the M point, M$-$K direction will be preferable for the electron transport in strain free condition. We observed that applied tensile strain lowers (increases) the CB2 (CB1) band. When tensile strain is equal or greater than 4%, the energy order of CB1 and CB2 is switched. Since these bands have different band dispersions, we are able to modify electronic transport properties of electrons. In $Hf_2MnC_2O_2$, VBM remains close to the $\Gamma$ point. There is no significant change in $m^*_{\mathrm{hM}}$ and $m^*_{\mathrm{hK}}$ while strain is applied. Similarly, due to switching of energy order of the CB3 and CB4 bands for tensile strain values greater than 2% in V based monolayer, the effective mass of electron becomes less than half of the value at 0% strain in the $\Gamma-$M direction. This is attributed to the different curvature of CB3 and CB4. The former is flatter than the latter at the band edges.

### 3.3.3 Magnetic Properties

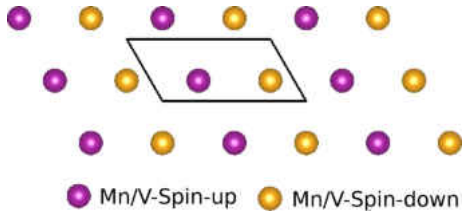


Figure 3.9: Antiferromagnetic configuration for $Hf_2MnC_2O_2$ and $Hf_2VC_2O_2$ under biaxial strain. Since the Mn/V atoms are the main contributors for the magnetism of respective systems, only Mn/V atoms are shown.

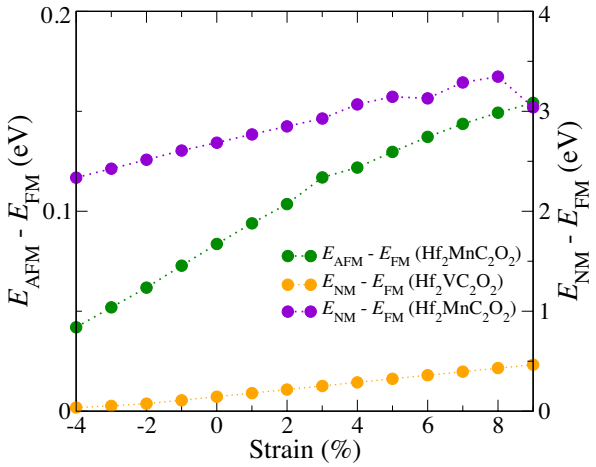


Figure 3.10: $E_{\mathrm{NM}} - E_{\mathrm{FM}}$ and $E_{\mathrm{AFM}} - E_{\mathrm{FM}}$ as a function of strain for $Hf_2MnC_2O_2$ and $Hf_2VC_2O_2$. Here, $E_{\mathrm{AFM}} - E_{\mathrm{FM}}$ for V based monolayer is not shown since it always provides $E_{\mathrm{FM}} \approx E_{\mathrm{NM}}$.

Mn, V and Hf in $Hf_2MnC_2O_2$ and $Hf_2VC_2O_2$ are at 4+ oxidization state.[25] The spontaneous magnetic moment in the ferromagnetic phase is mainly contributed by the $t_{2g}$ states of the $3d$ orbitals of the $Mn^{4+}$ and $V^{4+}$ ions because the unpaired electrons of those ions resides in $t_{2g}$ states. The electronic configurations of $Mn^{4+}$, $V^{4+}$ and $Hf^{4+}$ are $[Ar]3d^3$, $[Ar]3d^1$ and $[Ar]3d^0$, respectively.[25] The magnetic moment on C atoms are anti-parallel to that of Mn and V atoms as can be seen in Fig. 3.12. After taking all the contributions from each atom into account, total magnetic moment under 0% and tensile strain in ferromagnetic phase becomes 3.00 $\mu_{\mathrm{B}}$ and 1.00 $\mu_{\mathrm{B}}$ for $Hf_2MnC_2O_2$ and $Hf_2VC_2O_2$, respectively.

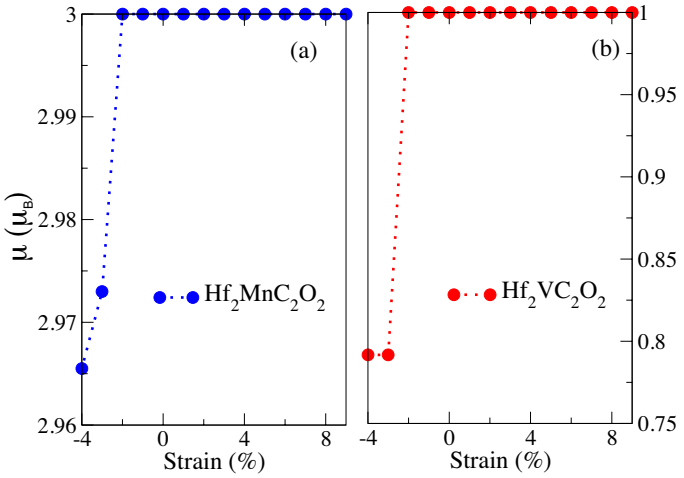


Figure 3.11: Variation of the total magnetic moment ($\mu$) in (a) $Hf_2MnC_2O_2$ and (b) $Hf_2VC_2O_2$ under biaxial strain.

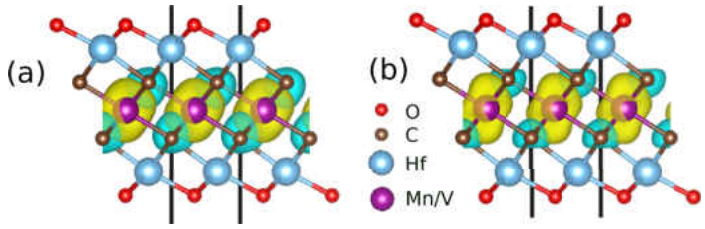


Figure 3.12: The magnetic spin density of (a) $Hf_2MnC_2O_2$ and (b) $Hf_2VC_2O_2$ strain free 2D materials.Yellow and blue represent spin up and down, respectively.

On the contrary, under biaxial compressive strain, total magnetic moment ($\mu$) starts diminishing in both materials when compressive strain exceeds 3%. This is different from the well-known MXenes like $Ti_2C$, $Ti_2N$, $V_2C$ and $V_2N$, where the $\mu$ is higher under compressive strains.[113] These strain effects are much significant in $Hf_2VC_2O_2$, where $\mu$ at -4% strain is 0.2 $\mu_B$ less than that of unstrained material (Fig.3.11). However, in $Hf_2MnC_2O_2$, $\mu$ at -4% strain is only 0.03 $\mu_B$ less than the value at 0%. As seen in Fig. 3.2, Mn-C and V-C bond lengths decrease while biaxial compressive strain increases. Due to its high electronegativity, the C atom is able to attract electrons from Mn easily, when the bond length decreases. Moreover, the Bader charge analysis confirms that there is more charge transfer from Mn and V atoms to the C atoms at compressive strains as explained in the section 3.3.2. Thus, Mn and V lose unpaired electrons and this reduces the total magnetic moment.

HSE06 calculations also agree with our total magnetic moment calculations, as shown in TABLE A1 and A2 in the Appendices.

To reveal the magnetic ground state of $Hf_2MnC_2O_2$ and $Hf_2VC_2O_2$ as a function of biaxial strain, the energy difference between magnetic states (FM, AFM and NM) were calculated. In order to calculate $E_{\mathrm{AFM}}$ values, different supercell structures with collinear AFM configurations such as $1 \times 2$, $2 \times 1$, $2 \times 2$, and $1 \times \sqrt{3}$ can be proposed as discussed in Dong *et al.*.[25] It is clear from Fig.3.1, that the Mn and V atoms reside on the same layer in the respective MXenes. If all the atoms except Mn/V atoms are neglected due to the negligible contribution for the total magnetic moment, Mn/V atoms resemble a hexagonal pattern as shown in Fig. 3.9. Therefore, due to the hexagonal symmetry of the Mn/V layers, all these supercells represent the same AFM configuration. It should be mentioned, that MXenes with two layers of Mn atoms, such as $Mn_2NO_2$, provide different AFM configurations due to the inter-layer and intra-layer exchange coupling.[41] Since the biaxial strain does not change the symmetry of $Hf_2MnC_2O_2$ and $Hf_2VC_2O_2$ MXenes, where only the intra-layer interactions are available between Mn/V atoms, we considered only the $2\times1$ structure as shown in Fig. 3.9. And also, it should be mentioned that even non-collinear AFM phases provide the same energy per unit formula.[25] Our calculations show, that the unstrained $Hf_2MnC_2O_2$ is a ferromagnetic material with $E_{\mathrm{AFM}} - E_{\mathrm{FM}} \approx 0.0795$ eV, while $E_{\mathrm{NM}} - E_{\mathrm{FM}}$ is close to 2.614 eV. Here, $E_{\mathrm{FM}}$, $E_{\mathrm{AFM}}$ and $E_{\mathrm{NM}}$ are the total energies for ferromagnetic, anti-ferromagnetic and non-magnetic states, respectively. For $Hf_2VC_2O_2$, AFM state does not exist and we have $E_{\mathrm{NM}} - E_{\mathrm{FM}} = E_{\mathrm{AFM}} - E_{\mathrm{FM}}$, which is 0.137 eV. In order to investigate the energy difference between magnetic states as function of strain, we varied biaxial strain within the range of [-4%, 9%] and calculated $E_{\mathrm{AFM}} - E_{\mathrm{FM}}$ and $E_{\mathrm{NM}} - E_{\mathrm{FM}}$ as shown in Fig. 3.10. As biaxial tensile strain increases, the $E_{\mathrm{AFM}} - E_{\mathrm{FM}}$ difference increases as well, indicating that ferromagnetic state becomes more stable with applied strain.

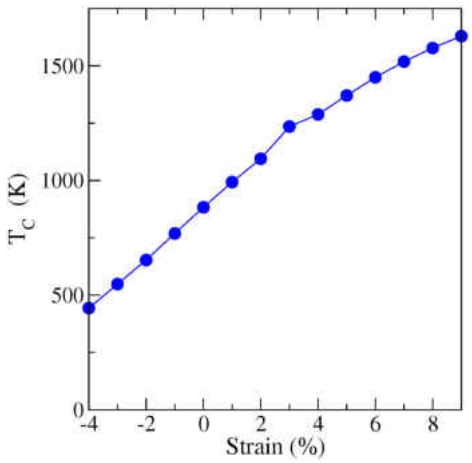


Figure 3.13: Variation of the Curie temperature ($T_C$) in $Hf_2MnC_2O_2$ under biaxial strain.

In order to investigate how the biaxial strain affects on the Curie temperature ($T_C$) of the $Hf_2MnC_2O_2$ monolayer, the total spin exchange interaction is taken into account by using the Hamiltonian, $\hat{H}$, in equation 3.2. Here, J is the nearest neighbor interaction parameter, and also $\hat{S}_i$ and $\hat{S}_j$ are the spin-angular momentum operators at $i^{th}$ and $j^{th}$ sites.[25,114] As explained before, only $Mn^{4+}$ ions contribute for spontaneous magnetic moments. Therefore, by considering the 6 nearest neighbors of the $Mn^{4+}$ in the unit cell of the monolayer, we are able to obtain the expressions 3.3 and 3.4 for the total energy per unit cell in ferromagnetic ($E_{\mathrm{FM}}$) and anti-ferromagnetic ($E_{\mathrm{AFM}}$) phases. In equations 3.3 and 3.4, $E_0$ is the energy of the nonmagnetic state. Thus, the difference between those two energies can be employed to find J using the equation $\mathrm{J} = (E_{\mathrm{AFM}} - E_{\mathrm{FM}})/4\mu^2$. Finally, $T_C$ for an infinitely large hexagonal monolayer can be estimated by applying the equation 3.5 where $k_B$ is the Boltzmann constant.[25,115] Unstrained Mn based monolayer provides $T_C$ of 836 K. It is clear that enhanced $T_C$ can be obtained due to higher $E_{\mathrm{AFM}} - E_{\mathrm{FM}}$ energy difference under tensile strain. For instance, $T_C$ of Mn based monolayer become 1094 K and 1288 K at 2% and 4% strains, respectively. Thus, $Hf_2MnC_2O_2$ becomes a half metal with enhanced Curie temperature at 8% strain where only the spin-up electron bands show metallic properties (see Fig. 3.5 and Fig. 3.13). Therefore, strained $Hf_2MnC_2O_2$ can

be a prominent material for future spintronic applications.

$$\hat{\mathrm{H}} = -\sum_{i,j} \mathrm{J}\hat{S}_i \cdot \hat{S}_j \tag{3.2}$$

$$E_{\mathrm{FM}} = E_0 - 3\mathrm{J}\mu^2 \tag{3.3}$$

$$E_{\mathrm{AFM}} = E_0 + \mathrm{J}\mu^2 \tag{3.4}$$

$$T_C = 3.642\frac{\mathrm{J}\mu^2}{k_B} \tag{3.5}$$

As shown in Fig. 3.4, the spin splitting due to magnetic exchange field can be seen in both unstrained materials. While tensile strain is applied, the spin-up states move towards the Fermi level and the spin-down states move away from the Fermi level (see Fig. 3.5 and Fig. 3.8). As a result of extended bond lengths under tensile strain, C-$p$ and Mn-$d$ interaction becomes weaker. Consequently, Mn-$d$ electrons are much localized at $Mn^{4+}$ ions, and spin polarization becomes stronger.

### 3.3.4 Conclusions

In summary, we investigated the impact of biaxial compressive and tensile strain on the structural, electronic and magnetic properties of $Hf_2MnC_2O_2$ and $Hf_2VC_2O_2$ monolayers. We showed that Mn- and V-based structures are able to sustain the stress values as large as 54.6 GPa and 56.2 GPa, respectively. Both materials become metals, when compressive strain is larger than 2%, and tensile strain is larger than 9%. For strain values within [-4%, 9%], band gap of Mn-based system can reach up to 0.45 eV, whereas that of V based system rises up to 0.23 eV at most. A semiconductor to half metal transition occurs at around 2% biaxial compressive strain and 8% tensile strain for $Hf_2VC_2O_2$ and at around 8% tensile strain for $Hf_2MnC_2O_2$. The effective

mass of electrons can be tuned by strain due to change of band order of the lowest energy conduction bands in both monolayers. It can be proved that Hf-M′-Hf angle and M′-C bond length variation (M′ is Mn or V) of respective systems mainly cause modulation of the electronic and magnetic properties. We found that higher the compressive strain, lower the total magnetic moment is in both systems. This can be attributed to the high charge transfer from Mn and V atoms to C atoms. The Curie temperature ($T_C$) is highly tunable with respect applied strain. $T_C$ can be increased to 1577 K from 836 K by applying a 8% tensile strain for $Hf_2MnC_2O_2$. Such a robust magnetism and tunable electronic properties ensures that the considered MXenes are promising candidates for spintronic applications.

## 3.4 Uniaxial Strain Effects on $Hf_2MnC_2O_2$ 2D Material

### 3.4.1 Strain and Structure

Table 3.3: The elastic constants $C_{11}$, $C_{22}$, $C_{12}$, monolayer thickness (t) and 3D Young's modulus ($Y_{3D}$) values under -4%, 0%, 4% and 8% uniaxial strains.

| | **zig-zag (x)** | | | | **armchair (y)** | | | |
|---|---|---|---|---|---|---|---|---|
| Strain (%) | -4 | 0 | 4 | 8 | -4 | 0 | 4 | 8 |
| $C_{11}$ (GPa) | 429.7 | 385.2 | 328.1 | 258.5 | 407.9 | 385.2 | 312.9 | 214.7 |
| $C_{22}$ (GPa) | 394.3 | 384.9 | 373.4 | 347.8 | 386.5 | 384.9 | 381.7 | 382.1 |
| $C_{12}$ (GPa) | 91.8 | 88.2 | 82.4 | 82.5 | 104.7 | 88.2 | 82.4 | 83.6 |
| t (nm) | 0.911 | 0.901 | 0.894 | 0.888 | 0.910 | 0.901 | 0.894 | 0.887 |
| $Y_{3Dx}$ (GPa) | 408.3 | 364.9 | 309.9 | 238.9 | 379.6 | 364.9 | 295.1 | 196.4 |
| $Y_{3Dy}$ (GPa) | 374.6 | 364.7 | 352.7 | 321.4 | 359.6 | 364.7 | 359.9 | 349.5 |

In order to apply uniaxial strain, the rectangular cell structure for $Hf_2MnC_2O_2$ shown in Fig. 3.14 was considered. The GGA+U calculations give the optimized monolayer lattice parameters as $a_0 = 3.253$Å and $b_0 = 5.634$Å. As can be seen in Fig. 3.14 (b), Mn is sandwiched between two O-Hf-C layers where O is the surface termination. Thus, there are four Hf, four O, four C, and two Mn atoms in the rectangular simulation cell where Hf makes bonds with both C and O atoms while

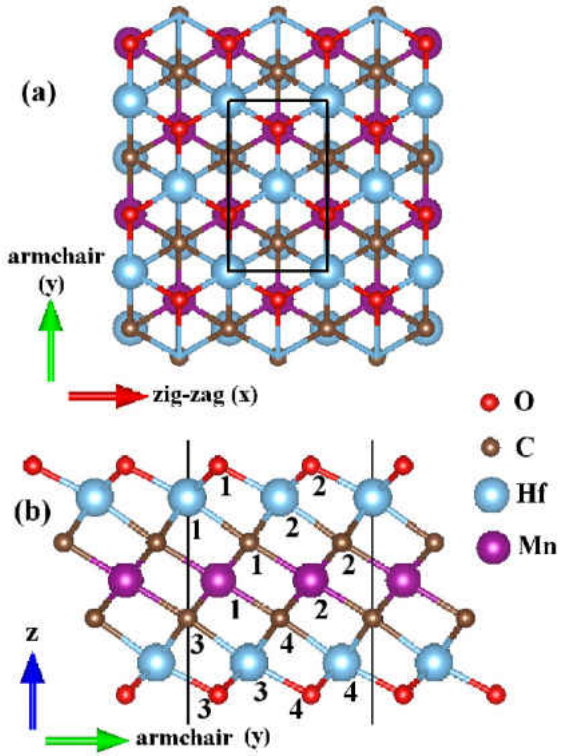


Figure 3.14: (a)Top and (b)side views of $Hf_2MnC_2O_2$ monolayer.

Mn makes bonds only with C atoms. The computed Hf-C, Mn-C and Hf-O bond lengths are 2.319, 2.201, and 2.115 Å, respectively.

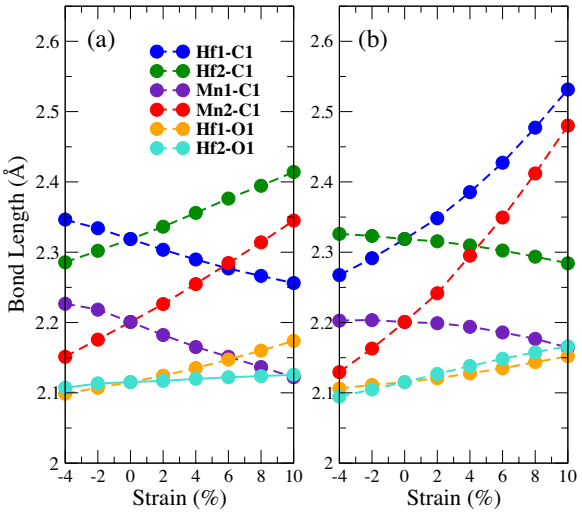


Figure 3.15: Variation of the bond lengths under uniaxial strain in the (a) $x$ and (b) $y$ directions.

Strain is applied in the zig-zag ($\epsilon_x$) or armchair ($\epsilon_y$) directions as $\epsilon_x = \frac{a-a_0}{a_0}$ and

$\epsilon_y = \frac{b-b_0}{b_0}$ where $a$ and $b$ are the lattice constants of the strained monolayer in the $x$ and $y$ directions, respectively. Due to the symmetry, studying Hf1-O1, Hf2-O1, Hf1-C1, Hf2-C2, Mn1-C1 and Mn2-C1 is sufficient for investigating the variation of the bond lengths due to the applied uniaxial strain. As can be seen in Fig. 3.15(a), transition metal (TM)-C bond lengths change differently according to the direction of uniaxial strain. For instance, Hf1-C1 and Mn1-C1 increase under tensile strain in the $y$ direction whereas those quantities decrease under tensile strain in the $x$ direction. On the contrary, Hf2-C1 and Mn2-C1 bond lengths rise (decline) as tensile strain is applied in the $x$ ($y$) direction. These distinct behaviors exist due to the Poisson effect where the structure contracts (expands) in one direction when a tension (compression) is applied in the perpendicular direction. Our calculations show that the Poisson ratio is around 0.22, which indicates that the bond length change in the opposite direction due to the strain is very small. Despite the fact that TM-C bond lengths are behaving differently as above, both Hf-O bond lengths increase (decrease) under uniaxial tensile (compressive) strain applied in the zig-zag and armchair directions.

The strain energy ($E_s$) under uniaxial strain is calculated using $E_s = E - E_0$ where $E$ is the total energy of the strained material and $E_0$ is the total energy of the strain-free material. The stress is calculated as a function of strain using the equation $\sigma = \frac{1}{V_0}\frac{\partial E}{\partial \epsilon_i}$ where $V_0$ is the volume of the strain-free monolayer and $\epsilon_i$ is the strain in the direction $i$ ($x$ or $y$). Here, the thickness (6.961 Å) was considered as the distance between two oxygen layers. As was illustrated by Fig. 3.16, the monolayer is able to handle higher stress values when the uniaxial strain is applied in the zig-zag direction. This is due to the fact that TM-C bond lengths do not increase much at higher tensile strains in the $x$ direction compared to that in the $y$ direction as illustrate in Fig. 3.2. Thus, at higher strains in the $y$ direction, bond lengths become weaker. The ultimate stress in the $x$ direction is 46.3 GPa while that in the $y$ direction is 35.7 GPa. Moreover, the corresponding ultimate strain is 18% in both directions.

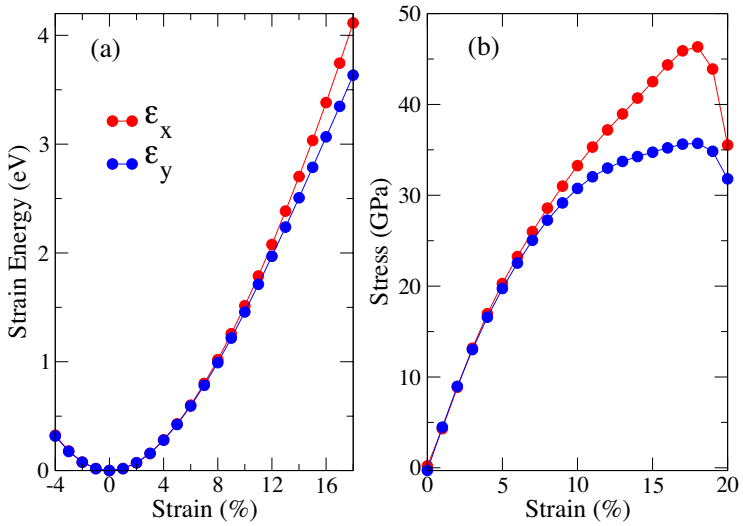


Figure 3.16: (a) Strain energy per formula unit and (b) stress as a function of uniaxial strain in the zig-zag and armchair directions.

The surface Young's modulus $Y_{2D}$ in the $x$ and $y$ directions for a rectangular structure can be calculated using Eq. 3.6 and Eq. 3.7 where the elastic constants $C_{11}$ and $C_{22}$ are the axial compression moduli in the $x$ and $y$ directions, respectively, and $C_{12}$ is the transverse expansion modulus:[86]

$$Y_{2Dx} = \frac{C_{11}C_{22} - C_{12}^2}{C_{22}} \tag{3.6}$$

$$Y_{2Dy} = \frac{C_{11}C_{22} - C_{12}^2}{C_{11}} \tag{3.7}$$

Since the thickness changes under uniaxial strain (see TABLE 3.3), we normalized $Y_{2D}$ as $Y_{3D} = Y_{2D}/t$ and the elastic constants as $C_{ij} = C_{ij(2D)}/t$ where $i$ and $j$ are 1 and 2, respectively. The thicknesses are calculated by considering multilayer configurations with van der Waals interactions as defined by DFT-D3 with Becke-Jonson damping.[106,107] Thus, TABLE 3.3 provides the Young's modulus values and the elastic constants in GPa. At 0% strain, $C_{11} = C_{22} = 385$ GPa and $Y_{3Dx} = Y_{3Dy} = 365$ GPa due to the hexagonal symmetry of the strain-free $Hf_2MnC_2O_2$ monolayer. When uniaxial strain is applied, those quantities are no longer equal ($C_{11} \neq C_{22}$ and $Y_{3Dx} \neq Y_{3Dy}$),

since the symmetry is broken. At 8% strain in either direction, there is a significant difference between $x$ and $y$ components of $Y_{3D}$, where the latter is higher than the former. Thus, stiffness will be low in the zig-zag direction, when a high uniaxial tension is applied ($Y_{3Dx} = 238.9$ GPa at $\epsilon_x = 8\%$ and $Y_{3Dx} = 196.4$ GPa at $\epsilon_y = 8\%$ ). Even though stiffness declines in both directions under tension due to bond weakening, there is still a remarkably high stiffness ($Y_{3Dy} > 310$ GPa) in the armchair direction at 8% strains compared to that in the zig-zag direction.

### 3.4.2 Electronic Properties

The band structures were obtained by considering the high-symmetry points of the rectangular supercells, i.e. Γ (0,0,0), X (0.5,0,0), S (0.5,0.5,0) and Y (0,0.5,0), under uniaxial strains applied in the zig-zag ($\epsilon_x$) and armchair ($\epsilon_y$) directions as shown in Fig. 3.18. Strain-free $Hf_2MnC_2O_2$ is a semiconductor with an indirect band gap of 0.282 eV. The conduction band minimum (CBM) resides at the S point, while the valence band minimum (VBM) resides at the Γ point. As strain is applied, the lower three bands (see Fig. 3.17), namely CB1, CB2, and CB3, shift considerably as illustrated in Fig. 3.18. DOS calculations reveal that TM-$d$ and O-$p$ states hybridize to form CB1, while TM-$d$ orbitals together with $p$ orbitals of Hf, C, and O hybridize to construct CB2 and CB3. CB1 band is occupied by the spin-up electrons while CB2 and CB3 bands are occupied by the spin-down electrons, as shown in Fig. 3.17.

TABLE 3.5 reveals that $Hf_2MnC_2O_2$ monolayer remains an indirect-band-gap semiconductor under tensile strain in the zig-zag direction. While tensile strain rises in this direction, CB1 does not move noticeably with respect to the top of the valence band until strain of 4%. Thus, band gap remains between 0.28 eV and 0.24 within $\epsilon_x$ =0% to $\epsilon_x$ =4% range, as shown in Fig. 3.20. After $\epsilon_x = 4\%$, the bottom of CB2 becomes CBM, which appears at Y point. Since CB2 moves towards the valence band as tensile strain rises further in the zig-zag direction, there is a sudden band

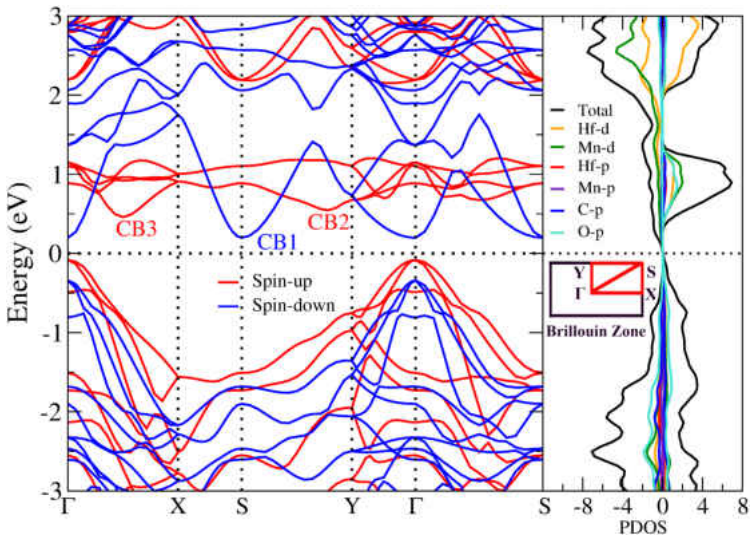


Figure 3.17: Spin-resolved electronic band structure and partial density of states (DOS) for strain free rectangular super-cell of $Hf_2MnC_2O_2$ monolayer. Fermi energy marks zero energy.

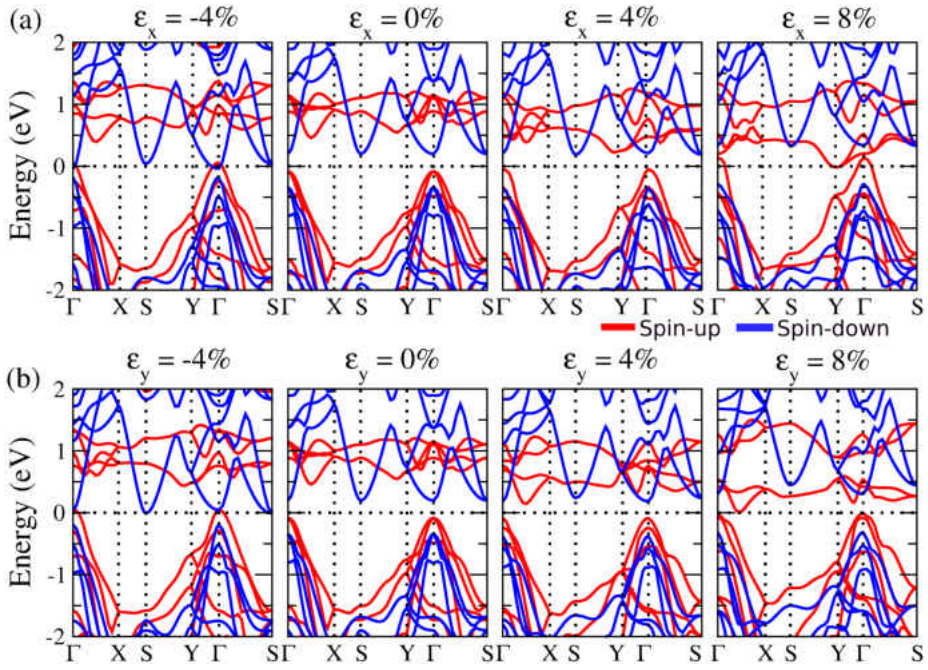


Figure 3.18: The calculated spin-resolved band structure of $Hf_2MnC_2O_2$ for different uniaxial strain values in (a) zig-zag and (b) armchair directions. Spin-up and spin-down bands are in red and blue, respectively. Fermi energy marks zero energy.

gap drop after $\epsilon_x = 4\%$. the CB2 and valence band start crossing the Fermi level at $\epsilon_x = 7\%$. At $\epsilon_x = 7\%$, only the bands with spin-up electrons cross the Fermi level. As a consequence, $Hf_2MnC_2O_2$ becomes a half-metal, where spin-down electron bands

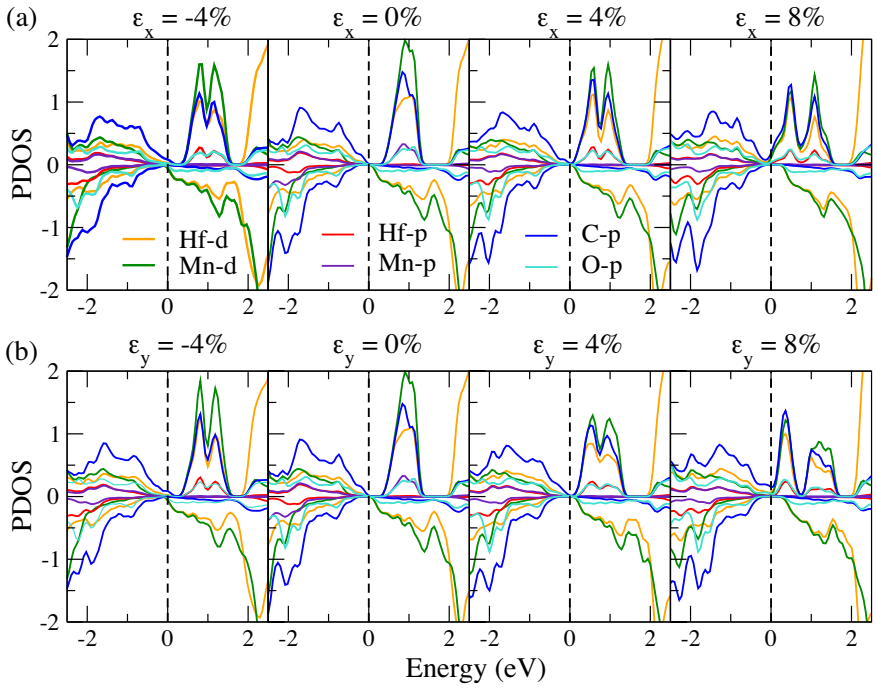


Figure 3.19: The calculated Partial Density of States (PDOS) of $Hf_2MnC_2O_2$ for different uniaxial strain values in (a) zig-zag and (b) armchair directions. Fermi energy marks zero energy.

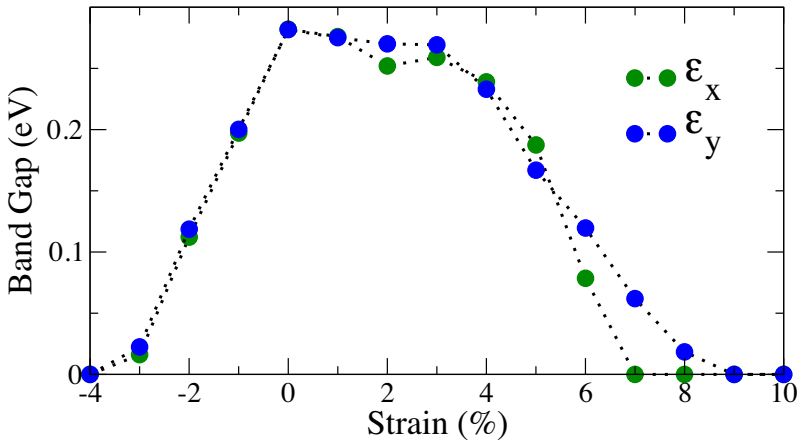


Figure 3.20: Variation of band gap as a function of strain.

make a band gap of 0.61 eV. The partial density of states (PDOS) studies show that even though the main contributor in conduction bands of spin-up electrons near the Fermi level is Mn-d orbitals at 0% strain, Mn-d, Hf-d and C-p contribute under tensile strains. The contributions from each orbital for the valence bands near the Fermi level barely changes as strain is applied (see Fig. 3.19).

Table 3.4: The average Bader charge transfer $\Delta q$ for each atom are mentioned for strained and unstrained $Hf_2MnC_2O_2$.

| | Property | -4% | -2% | 0% | 2% | 4% | 8% |
|---|---|---|---|---|---|---|---|
| zig-zag | $\Delta q_{Hf}$(e) | 3.937 | 3.937 | 3.939 | 3.938 | 3.943 | 3.861 |
| | $\Delta q_O$(e) | -2.001 | -2.007 | -2.011 | -2.011 | -2.023 | -2.058 |
| | $\Delta q_C$(e) | -2.687 | -2.674 | -2.669 | -2.660 | -2.652 | -2.635 |
| | $\Delta q_{Mn}$(e) | 1.504 | 1.489 | 1.480 | 1.466 | 1.464 | 1.426 |
| armchair | $\Delta q_{Hf}$(e) | 3.939 | 3.939 | 3.939 | 3.936 | 3.815 | 3.859 |
| | $\Delta q_O$(e) | -2.004 | -2.007 | -2.011 | -2.009 | -2.014 | -2.093 |
| | $\Delta q_C$(e) | -2.690 | -2.680 | -2.669 | -2.659 | -2.521 | -2.474 |
| | $\Delta q_{Mn}$ | 1.511 | 1.496 | 1.480 | 1.463 | 1.439 | 1.417 |

Table 3.5: The position of the conduction band minimum (CBM) for each 2D material under uniaxial strain in the zig-zag ($x$) and armchair ($y$) directions. VBM resides always at the Γ point.

| Strain (%) | $CBM_x$ | $CBM_y$ |
|---|---|---|
| -3 | Γ | S |
| -2 | Γ | S |
| -1 | Γ | S |
| 0 | S | S |
| 1 | S | Γ |
| 2 | S | Γ |
| 3 | S | Γ |
| 4 | S | Γ-X |
| 5 | Y | Γ-X |
| 6 | Y | Γ-X |
| 7 | - | Γ-X |
| 8 | - | Γ-X |

Even though the band gap of $Hf_2MnC_2O_2$ changes in a similar way under the strain in the armchair direction (see Fig. 3.20), the CBM appears at the different k-points as illustrated in TABLE 3.5. For the strains greater than 3% in this direction, the CBM resides between Γ and X points since CB3 reaches the Fermi level. Similar to the case of zig-zag direction, the spin-up electron bands are populated near the Fermi level at higher strains. Thus, $Hf_2MnC_2O_2$ turns into a half-metal at $\epsilon_y = 9\%$ with a band gap of 0.82 eV made by the bands with spin-down electrons.

It is clear that there is a sharp drop in band gap when compressive strain is applied

on the monolayer in either direction. CB1 forms the CBM which appears at the Γ point from $\epsilon_x = \epsilon_y$ = -1% to -3%. CB1 moves downward and crosses the Fermi-level at $\epsilon_x = \epsilon_y$ = -4%. Since a very small portion of the bottom of the conduction band and the top of the valence bands crosses the Fermi level, $Hf_2MnC_2O_2$ is a semi-metal at $\epsilon_x = \epsilon_y$ = -4%. Bottom of CB1 and VBM move towards each other to reduce the separation between the anti-bonding and bonding states. Since Hf-O bond lengths become shorter at negative strains, TM-*d* and O-*p* bonding enhances.

Materials like $Hf_2MnC_2O_2$ monolayers require special attention due to the presence of partially filled d orbitals.[116] The Hartree electron-electron repulsion potential in DFT implies how an electron interacts with the electron-density of the system. Since the electron-density contains the charge of that electron as well, an unphysical self interaction energy is present in the total energy.[84,117,118] This self interaction error is significant in the transition metal atoms where the unpaired electrons are delocalized to minimize the self-interaction.[84] Our GGA calculations in Fig. A6 show that all the strained $Hf_2MnC_2O_2$ monolayers are metallic systems (see Appendices) as a result of delocalization of unpaired *d*-electrons. To overcome this issue, GGA+U method utilizes the on-site Coulomb potential (U), which localizes the transition metal electrons in the partially filled energy states. Furthermore, HSE06 calculations constitute the nonlocal Hartree-Fock exchange potential to minimize the effects of so called self interaction.[119,120] Thus, both GGA+U and HSE06 methods prove that the strain-free $Hf_2MnC_2O_2$ nanosheets are semiconductors, and it retains the semiconductor properties at 4% strains in both zig-zag and armchair directions, as illustrated by Fig. A7 (see Appendices). As mentioned in the TABLE S1 and S2, hybrid functional calculations provide higher band gaps. For instance, 0.484 eV and 0.324 eV band gaps are obtained for $\epsilon_x = 0\%$ and $\epsilon_x = 4\%$, respectively. On the contrary, GGA+U provides smaller band gap values of 0.282 eV and 0.239 eV at $\epsilon_x = 0\%$ and $\epsilon_x = 4\%$, respectively. HSE06 method confirms that bands are shifting in the same way as in

GGA+U method. Thus, zero band gaps exist under $\epsilon_x = \epsilon_y$ =-4% and $\epsilon_x$ =8% and also a small band gap ($\approx$ 0.103 eV) exists when $\epsilon_y$ =8% due to bands shifting.

Band structure variations are directly related to the charge transfer in each atomic species. Thus, we studied the Bader charge analysis for several strain values in the zig-zag and armchair directions, as mentioned in TABLE 3.4.[112] It is clear from TABLE 3.4 that the structural variations under compression in either direction considerably affect the charge transfer of Mn and C atoms as compared to those of Hf and O atoms. Small compressive strains alter $\Delta q_{\mathrm{Mn}}$ and $\Delta q_{\mathrm{C}}$ noticeably as compared to $\Delta q_{\mathrm{Hf}}$ and $\Delta q_{\mathrm{O}}$. This is mainly because of considerable shortening of Mn1-C1 and Mn2-C1 bond lengths, while uniaxial compression is applied in the $x$ and $y$ directions respectively (see Fig. 3.2). However, Hf-O bond length change within 0% to -4% is relatively small. At large tensile strains, less charge transfer for Hf, Mn and C atoms can be seen due to the fact that charges are more localized when the bond strengths become weaker.

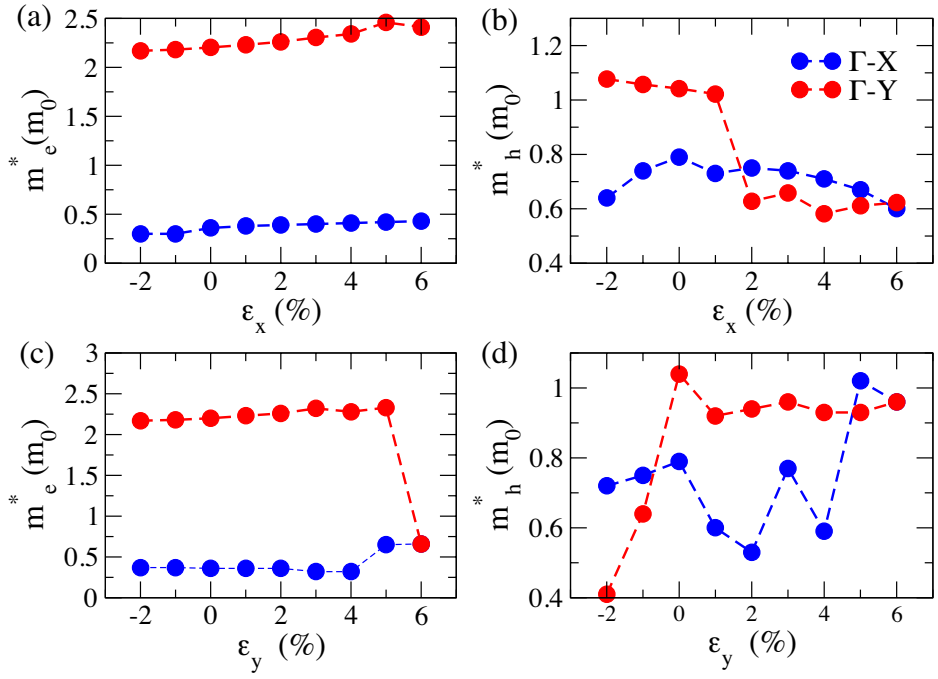


Figure 3.21: Variation of the effective mass ($m^*$) of (a) electrons and (b) holes under uniaxial strain in the zigzag direction ($\epsilon_x$) and $m^*$ of (c) electrons and (d) holes under uniaxial strain in the armchair direction ($\epsilon_y$). Here, $m_0$ is the rest mass of electron.

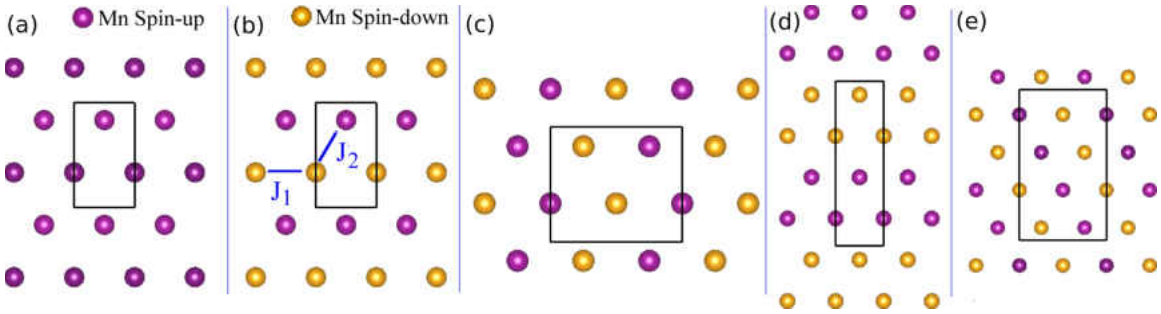


Figure 3.22: (a) FM, (b) AFM1, (c) AFM2, (d) AFM3 and (e) AFM4 spin configurations with rectangular super-cells indicated. Only Mn atoms are considered, since contribution for magnetic moment from other atoms are negligible.

We computed the effective masses of electrons and holes as a function of uniaxial strain using the equation 3.1. The high symmetric directions $\Gamma-X$ and $\Gamma-Y$ in reciprocal lattice correspond to the armchair and zig-zag directions in real space, respectively. Thus, by calculating the effective mass of electrons and holes in $\Gamma-X$ and $\Gamma-Y$ directions, we are able to find a preferable direction for carrier transport. Regardless of the strain direction, $Hf_2MnC_2O_2$ monolayer is a semiconductor in the strain range of [-2%, 6%]. Thus, this strain region was considered for $m^*$ calculations of this 2D material. For unstrained $Hf_2MnC_2O_2$, the effective masses of electrons and holes are larger along the $\Gamma-Y$ direction, since the bottom of CB1 in the $\Gamma-Y$ direction is flatter than that in the $\Gamma-X$ direction. When strain is applied in the zig-zag direction, $m_e^*$ remains around $0.3m_0$-$0.4m_0$ in the $\Gamma-X$ direction, while $m_e^*$ is between $2m_0$ and $2.5m_0$ in the other direction. Same kind of behavior of $m_e^*$ can be seen for $\epsilon_y$ case, except at 6% strain, where $m_e^*$ is approximately same in both directions as a result of change in energy order of CB1 and CB2. Therefore, as evidenced by Fig. 3.21, the armchair direction will be the most preferable direction for the electron transport.

### 3.4.3 Magnetic Properties

According to GGA+U calculations, the total magnetic moment ($\mu$) per formula unit is $3.00\mu_B$ ($\mu_B$ is the Bohr magneton). The main contribution to $\mu$ is from the Mn atom, which is in the +4 oxidation state. Our spin-polarized calculations show that contributions from other ions are negligible. The electronic configuration for $Mn^{4+}$ is [Ar] $3d^3$. The uncoupled 3d electrons occupy the $t_{2g}$ states ($d_{xy}$, $d_{yz}$, and $d_{xz}$), while the $e_g$ states ($d_{x^2}-d_{y^2}$ and $d_{z^2}$) are empty.[25] The magnetic moment behaves approximately in the same way under uniaxial strain in both directions [see Fig.3.23(a)]. While tension does not affect $\mu$, compressive strain decreases $\mu$ starting at around $-2\%$. This can be attributed to the increased charge transfer from Mn atom to C atom under compression as mentioned in the TABLE 3.4. Thus, Mn atoms lose electrons, while C atoms gain them under compressive strain. $\mu$ becomes 2.986 $\mu_B$ at $\epsilon_x = \epsilon_y = -4\%$. Since the magnetic moment change is negligible, we can assume that magnetic moment is approximately constant within this range of strain. Our HSE06 calculations also show a constant magnetic moment throughout this range of strain, as stated in TABLE A3 and A4 (see Appendices).

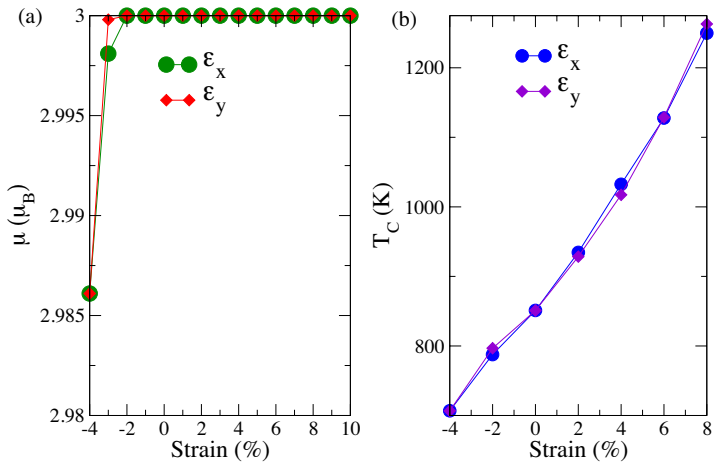


Figure 3.23: (a) The total magnetic moment and (b) Curie temperature ($T_C$) of $Hf_2MnC_2O_2$ as functions of strain

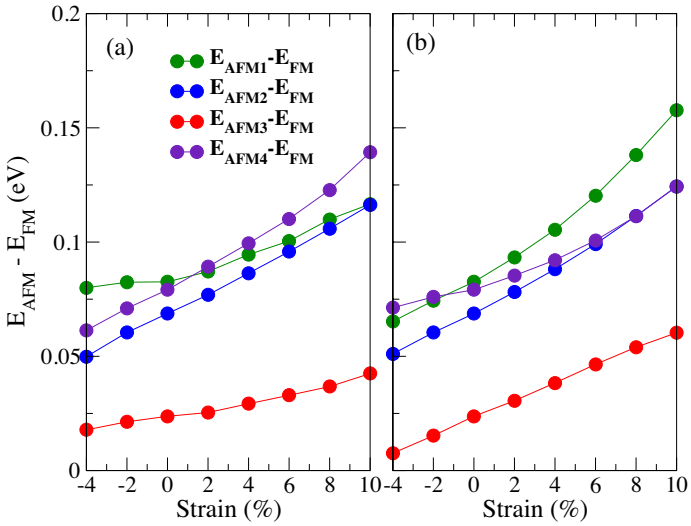


Figure 3.24: The energy differences per formula unit between each AFM and FM phases ($E_{\mathrm{AFM}} - E_{\mathrm{FM}}$) in the (a) zig-zag and (b) armchair directions.

In order to find the magnetic ground state of the monolayer at each strain applied, we calculated the total energies for various ferromagnetic (FM), antiferromagnetic (AFM), and non-magnetic (NM) configurations as illustrated in Fig. 3.22. In the AFM1 configuration [Fig. 3.22(b)], spin-down Mn atoms form straight lines, whereas in AFM2 [Fig. 3.22(c)] they form zig-zag lines. AFM3 [Fig. 3.22(d)] has spin-down stripes that are two sites thick. AFM4 [Fig. 3.22(e)] is the same as AFM1 rotated by 120°. As shown in Fig. 3.24 and A8 (see Appendices), we find that $E_{\mathrm{FM}}$ has the lowest than energy compared to any of the other configurations. Thus the ground state is ferromagnetic under uniaxial strain within the range $-4\%$ to $10\%$. $E_{\mathrm{NM}} - E_{\mathrm{FM}}$ is higher than 2.3 eV whereas $E_{\mathrm{AFM}} - E_{\mathrm{FM}}$ is always very low (less than 0.2 eV).

We approximated the magnetic behavior of $Hf_2MnC_2O_2$ by a classical spin-half Ising model on a triangular lattice, with strain-induced anisotropy. The Hamiltonian is[121]

$$H = E_0 - J_1 \sum_{\langle ij \rangle_x} \sigma_i \sigma_j - J_2 \sum_{\langle ij \rangle_{\mathrm{diag}}} \sigma_i \sigma_j, \tag{3.8}$$

where $\sigma_i = \pm 1$ are Ising spins, $\langle ij \rangle_x$ indicates that the sum is over nearest neighbors

in the horizontal $x$ direction, $\langle ij \rangle_{\text{diag}}$ indicates nearest neighbors in other directions, $J_1$ and $J_2$ are couplings along horizontal and diagonal directions as shown in Fig. 3.22, and $E_0$ represents the non-magnetic part of the energy. According to Eq. 3.8, the energies of the spin configurations in Fig. 3.22(a,b,e) are

$$E_{\text{FM}} = E_0 - J_1 - 2J_2 \tag{3.9}$$

$$E_{\text{AFM1}} = E_0 - J_1 + 2J_2 \tag{3.10}$$

$$E_{\text{AFM4}} = E_0 + J_1. \tag{3.11}$$

Solving for the couplings yields $J_1 = \frac{1}{4}(2E_{\text{AFM4}} - E_{\text{AFM1}} - E_{\text{FM}})$ and $J_2 = \frac{1}{4}(E_{\text{AFM1}} - E_{\text{FM}})$, which allows us to infer $J_1$ and $J_2$ from the results of DFT energy calculations. Thus, we obtain $J_1$ and $J_2$ as a function of uniaxial strain $\varepsilon_x$ or $\varepsilon_y$.

We used the above Ising model to predict the finite-temperature magnetic behavior of $Hf_2MnC_2O_2$ monolayer. Although Ising models on two-dimensional lattices can be solved using analytic methods,[122] here we used Monte Carlo methods (in particular the Wolff single-cluster algorithm[123]), which are easily generalized to multilayers or 3D models. $T_c$ increases with increasing strain, as shown in Fig. 3.23(b). As illustrated by Fig. 3.23, $T_c$ becomes greater than 1200 K while it converts into a half-metal under the uniaxial tension higher than 8%. Thus, $Hf_2MnC_2O_2$ monolayer can be transformed into an immensely useful material in the spintronic applications.

### 3.4.4 Conclusions

A first principle study based on density functional theory was carried out on $Hf_2MnC_2O_2$ ferromagnetic semiconductors to study the structural, electronic and magnetic property variations. According to the direction of uniaxial strain, different bond lengths are altered differently. It is clear that TM-C bonds are weakened significantly by the tension in the armchair direction compared to the tension in the zig-zag direction.

Thus, the maximum stress that the system can handle becomes lower when the tension is applied in the armchair direction. The tension (compression) in both directions lowers (enhances) the Young's modulus. As a result of conduction bands shifting under uniaxial strain, variation of CBM location can be observed while VBM always resides at the $\Gamma$ point. Consequently, indirect-to-direct band gap transition occurs in 1% to 3% range of tension in armchair direction. $Hf_2MnC_2O_2$ monolayer becomes a half-metal at $\epsilon_x = 7\%$ and $\epsilon_y = 9\%$. Semiconductor-to-metal transition occurs at $\epsilon_x = \epsilon_y = -4\%$. Our effective mass calculations show that armchair direction in real space will be preferable for electron transport due to the narrow band edges in $\Gamma-X$ direction of the reciprocal space. Moreover, the magnetic moment remains constant (there is only a negligible change) within -4% to 10% strain range. It is found that Curie temperature is highly tunable under uniaxial strain. For instance, $T_C$ is around 706 K at -4% in both directions while it is greater than 1200 K at 8% strain.

# CHAPTER IV

# ENGINEERING SURFACE DEFECTS OF $Hf_2MC_2O_2$ (M=Mn,V) MXenes

## 4.1 Introduction

Two-dimensional (2D) ferromagnetic materials are highly desirable for nanoscale spintronic devices due to their low thickness, high flexibility, high carrier mobility and enhanced spin-orbit coupling.[124,125] In the absence of spin-orbit coupling (SOC), the quantum Hamiltonian is invariant under global rotations of all spins. This continuous symmetry implies the existence of long-wavelength low-frequency Goldstone modes. Thermal occupation of these modes destroys long-range magnetic order at any finite temperature in dimensions $d \leq 2$ (the Mermin-Wagner theorem). For stable magnetic ordering, the continuous symmetry must be broken so that the Goldstone modes become "gapped" or "massive." Fortunately, 2D materials possess inherent spatial anisotropy due to their layered nature. This spatial anisotropy and the SOC conspire to induce magnetic anisotropy in spin space, such that some spin directions are favored over others.[126] Easy-axis anisotropy breaks the O(3) continuous symmetry down to a discrete $Z_2$ (Ising) symmetry, which permits ferromagnetic ordering below a finite Curie temperature, with a transition in the 2D Ising universality class. The magnetic anisotropy energy (MAE) also serves as a barrier to spin reversal.[127] As a consequence, 2D materials with easy-axis anisotropy and high MAE are highly desired for spintronic applications. (We note that other mechanisms exist for gapping

the Goldstone modes.[128]) Easy-plane anisotropy is less useful, as it reduces the O(3) symmetry to O(2) symmetry, which is still a continuous symmetry, so long-range order is still prohibited.

Finding 2D ferromagnetic materials with strong magnetic anisotropy is a major challenge for designing effective spintronics devices.[129] So far, only a few number of 2D materials with high MAEs have been reported. $CrI_3$ 2D flakes, which have a relatively high MAE of 686 $\mu$eV per Cr atom,[44] have been experimentally realized by mechanical exfoliation.[130] $Cr_2Ge_2Te_6$ ferromagnetic insulator nanosheets have uniaxial magnetic anisotropy and a Curie temperature of about 61 K.[131] $Fe_3GeTe_2$ ferromagnetic monolayers have a high MAE value of 920 $\mu$eV per Fe atom.[45] Another monolayer material, $VSe_2$, has been grown on graphite or $MoS_2$ by beam epitaxy,[132] and it has a high MAE of about 594 $\mu$eV.[133]

Various methods like strain engineering[134] and surface and atomic manipulation[28,135,136] have been proposed for increasing magnetic anisotropy. Theoretical investigations have found that the anisotropy of nitride MXenes can be tuned by changing the surface termination. For instance, 2D $Mn_2NO_2$ exhibits easy-axis anisotropy whereas $Mn_2NF_2$ has easy-plane anisotropy;[135] the MAE of 2H-$VSe_2$ increases from 0.594 meV to 0.746 meV under 2% compressive strain;[133] and also, 4% compressive strain enhances the MAE of 1T-$FeCl_2$ by 36.77% relative to that of an unstrained monolayer.[137]

In this chapter we study two families of double-transition-metal MXenes in the presence of surface defects. We calculate structural and electronic properties using density functional theory (DFT). We investigate magnetic properties by fitting DFT energies using classical Heisenberg models with single-site anisotropy and doing Monte Carlo simulations on such models. The calculations based on Heisenberg models indicate that the Curie temperatures determined in Chapter III based on Ising models are overestimated. Our main results, summarized in Table 4.4, are:

- Defects can drive transitions from semiconductor to metal or even half-metal.
- Magnetic moments are dominated by contributions from the 3d transition metal ions ($Mn^{4+}$ or $V^{4+}$).
- Defects modify magnetic moments ($\mu$) by as much as $\pm 25\%$.
- Defects modify magnetic anisotropies ($K$) by as much as 500%, and can change the sign of $K$.
- Defects modify exchange couplings between individual magnetic centers ($J_{ij}$) by as much as $\pm 90\%$.
- Due to the above, defect engineering can change a material such as $Hf_2MnC_2O_2$, predicted to have no long-range order at any $T > 0$, into one such as $Hf_2MnC_2O_2H_{0.22}$, which we predict to have $T_c \approx 171$ K.

## 4.2 Computational Methods

DFT calculations with spin-orbit coupling (SOC) were carried out using the Vienna *ab initio* Simulation Package (VASP)[74–77] with a plane wave basis set with Projected Augmented Wave (PAW) method.[81,82] Perdew-Burke-Ernzerhof (PBE)[100,101] pseudopotentials in the Generalized Gradient Approximation (GGA) method was taken into account with the energy cutoff value of 520 eV in the calculations. The energy convergence criterion was $10^{-8}$ eV, and the force convergence criterion of the ionic steps was set to $10^{-7}$ eV/Å, respectively. To avoid the interaction between periodic images of monolayers, a vacuum space of around 15 Å was set in the $c$-axis direction. A Γ-centered 12×12×1 Monkhorst-Pack $k$-mesh was used to sample the the Brillouin zone to relax the the unit cells of $Hf_2MnC_2O_2$ and $Hf_2VC_2O_2$ nanosheets. To calculate the band structures and magnetic anisotropy energies, a 24×24×1 $k-$mesh was considered. The O vacancies and the H adatoms were introduced on the surfaces of

3×3 supercells. First, the structure of the supercells was optimized with a 4×4×1 $k$-mesh. Then, the band structure and magnetic anisotropy calculations were carried out for the supercells with a 8×8×1 $k$-mesh. GGA with the strong on-site Coulomb interaction of localized $d$ electrons of the transition metal atoms were treated by using the Coulomb potential (U) method (GGA+U).[102] The U potentials were set to 2 eV for Hf and 4 eV for Mn and 3 eV for V.[25]

## 4.3 Results

### 4.3.1 Defects and Structure

We consider two types of defects: oxygen vacancies (where an O atom is removed from the top or bottom layers of the material) and hydrogen adatoms (where an extra H atom bonds to an O atom to form an OH group). We focus on arrangements of defects that preserve the six-fold symmetry of the material, to avoid numerical inaccuracies due to asymmetrical supercells. We consider defects within a $3 \times 3$ supercell, as shown in Fig. 4.1. Since the top and the bottom layers are identical, we show only one of the layers in the figure. The numerals 1 and 2 in the figure denote possible defect sites T1 and T2 on the top layer and sites B1 and B2 on the bottom layer. For single defects, all surface sites are equivalent; we use site T1. For two defects, the second defect was located at the sites T2, B1, or B2. The possible configurations for two defects are T1T2, T1B1, T1B2. In the T1B1 configuration, the second defect occupies the site right below the first defect (T1).

The energies of these configurations (from DFT without SOC) are compared in Table 4.1. It is always energetically favorable for both defects to reside on opposite surfaces of the nanosheet. For the HfMn material the T1B2 configuration always has the lowest energy. However, for two oxygen vacancies ($Hf_2VC_2O_{1.78}$) the T1B2 configuration is favored, whereas for two hydrogen adatoms ($Hf_2VC_2O_2H_{0.22}$) the

Table 4.1: Relative energies for double-defect configurations (per $3 \times 3$ supercell). Lowest-energy configurations are indicated by zeroes.

| Material | $\Delta E$(T1T2) (eV) | $\Delta E$(T1B2) (eV) | $\Delta E$(T1B1) (eV) |
|---|---|---|---|
| $Hf_2MnC_2O_{1.78}$ | 0.4018 | 0 | 0.4144 |
| $Hf_2MnC_2O_2H_{0.22}$ | 0.0348 | 0 | 0.0116 |
| $Hf_2VC_2O_{1.78}$ | 0.1173 | 0 | 0.1326 |
| $Hf_2VC_2O_2H_{0.22}$ | 0.0835 | 0.1154 | 0 |

T1B1 configuration is preferred. All further calculations were performed for these minimum-energy configurations.

The O vacancy formation energies ($E_{\text{form}}$) and the H adsorption energies ($E_{\text{ad}}$) were calculated using

$$\Delta E_{\text{form}} = \frac{1}{n}\left(9E_{\text{Hf}_2\text{MC}_2\text{O}_{2-n/9}} - 9E_{\text{Hf}_2\text{MC}_2\text{O}_2} + \frac{n}{2}E_{\frac{1}{2}\text{O}_2}\right),$$

$$\Delta E_{\text{ad}} = \frac{1}{n}\left(9E_{\text{Hf}_2\text{MC}_2\text{O}_2\text{H}_{n/9}} - 9E_{\text{Hf}_2\text{MC}_2\text{O}_2} - \frac{n}{2}E_{\frac{1}{2}\text{H}_2}\right).$$

Here, $E_{\text{Hf}_2\text{MC}_2\text{O}_{2-n/9}}$ and $E_{\text{Hf}_2\text{MC}_2\text{O}_2\text{H}_{n/9}}$ are the total energies of the systems with $n$ vacancies and $n$ adatoms respectively, while $E_{\text{Hf}_2\text{MC}_2\text{O}_2}$ is the energy of the original MXene material, and $E_{\frac{1}{2}\text{O}_2}$ and $E_{\frac{1}{2}\text{H}_2}$ are the energies per atom of isolated dioxygen and dihydrogen, respectively. The results in Table 4.2 show that the formation and adsorption energies do not change much with defect concentration. The negative $E_{\text{ad}}$ values suggest that spontaneous H adsorption is possible.

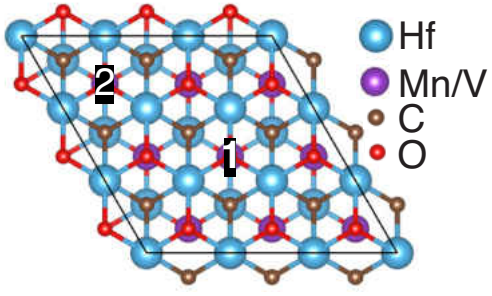


Figure 4.1: Defect sites T1 and T2 on the top layer (and B1 and B2 on the bottom layer) within a $3 \times 3$ supercell considered in this paper.

Table 4.2: Oxygen vacancy formation energies ($E_{\text{form}}$) and hydrogen adsorption energies ($E_{\text{ad}}$) per $3 \times 3$ supercell at two defect concentrations.

| Material | $\Delta E_{\text{form}}$ (eV) | $\Delta E_{\text{ad}}$ (eV) |
|---|---|---|
| $Hf_2MnC_2O_{1.89}$ | 5.569 | – |
| $Hf_2MnC_2O_2H_{0.11}$ | – | -1.769 |
| $Hf_2MnC_2O_{1.78}$ | 5.475 | – |
| $Hf_2MnC_2O_2H_{0.22}$ | – | -1.781 |
| $Hf_2VC_2O_{1.89}$ | 5.570 | – |
| $Hf_2VC_2O_2H_{0.11}$ | – | -1.835 |
| $Hf_2VC_2O_{1.78}$ | 5.392 | – |
| $Hf_2VC_2O_2H_{0.22}$ | – | -1.917 |

Table 4.3: Defect-induced strain ($\epsilon$) and band gap ($E_g$) for two 2D materials with different defect concentrations

| Material | $\epsilon(\%)$ | $E_g$ (eV) |
|---|---|---|
| $Hf_2MnC_2O_2$ | 0 | 0.282 |
| $Hf_2MnC_2O_{1.89}$ | -0.14 | 0 |
| $Hf_2MnC_2O_2H_{0.11}$ | -0.14 | 0 |
| $Hf_2MnC_2O_{1.78}$ | -0.19 | 0 |
| $Hf_2MnC_2O_2H_{0.22}$ | -0.01 | 0 |
| $Hf_2VC_2O_2$ | 0 | 0.150 |
| $Hf_2VC_2O_{1.89}$ | -0.04 | 0 |
| $Hf_2VC_2O_2H_{0.11}$ | 0.04 | 0 |

### 4.3.2 Electronic Properties

Our electronic bandstructure analysis with GGA+U+SOC calculations reveals that both materials are semiconductors, with band gaps 0.282 eV and 0.150 eV for $Hf_2MnC_2O_2$ and $Hf_2VC_2O_2$, respectively. Previous studies, based on spin-polarized calculations, found that the conduction bands near the Fermi levels of these materials are highly sensitive to the in-plane strains.[25–27] The valence-band maximum (VBM) and conduction-band minimum (CBM) of both monolayers are located at the Γ and K high-symmetry points in reciprocal space, as shown in Fig 4.2. Thus these 2D materials are indirect bandgap semiconductors.

Figure 4.2 shows that all single-defect and double-defect systems in this study are

Table 4.4: **Magnetic properties predicted for MXenes with and without surface defects.** Here, $\mu$ is the magnetic moment per formula unit and MAE is the magnetic anisotropy energy per formula unit calculated from DFT. Anisotropy parameters $K_1$ and $K_2$ and nearest-neighbor exchange couplings $J_1, \ldots, J_9$ were inferred from an energy mapping analysis. (The table shows the spread of $J$ values from smallest to largest.) Curie temperatures $T_c$ were calculated using Monte Carlo simulations of the classical Heisenberg model with anisotropy. "BKT" indicates that the material may exhibit a Berezinskii-Kosterlitz-Thouless transition to quasi-long-range magnetic order, but true long-range order only occurs at $T = 0$. Dashes indicate unperformed calculations.

| Material | $\mu$ ($\mu_B$) | MAE ($\mu$eV) | Anisotropy | $K_1$ ($\mu$eV) | $K_2$ ($\mu$eV) | Range of $J$ (meV) | $T_c$/K |
|---|---|---|---|---|---|---|---|
| $Hf_2MnC_2O_2$ | 3.00 | 56.77 | easy-plane | −57.11 | 0.10 | 20.4 | BKT |
| $Hf_2MnC_2O_{1.89}$ | 2.98 | 21.04 | easy-axis | 17.92 | 3.12 | 13 to 23 | 141 |
| $Hf_2MnC_2O_2H_{0.11}$ | 2.88 | 51.66 | easy-axis | 51.49 | 0.18 | 9 to 28 | 159 |
| $Hf_2MnC_2O_{1.78}$ | 3.00 | 165.33 | easy-plane | −226.9 | 74.71 | – | BKT |
| $Hf_2MnC_2O_2H_{0.22}$ | 2.77 | 144.44 | easy-axis | 69.97 | 0.40 | 0 to 38 | 171 |
| $Hf_2VC_2O_2$ | 1.00 | 9.48 | easy-axis | 8.63 | 0.85 | 18.8 | 141 |
| $Hf_2VC_2O_{1.89}$ | 1.00 | 53.51 | easy-axis | 41.66 | 11.97 | – | – |
| $Hf_2VC_2O_2H_{0.11}$ | 0.91 | 24.28 | easy-axis | 26.11 | −1.847 | – | – |

metallic (unlike the parent compounds, which are semiconductors). By comparing the band structures with and without defects, we can see that upper bands in the valence region shift to the conduction region, whereas lower conduction bands move towards the valence region. Thus, those displaced bands cross the Fermi level. The density of states (DOS) plots in Fig. 4.3 illustrate that the spin-up bands near the Fermi level result from hybridization of the Hf-d, Mn/V-d, and C-p orbitals, whereas the spin-down bands close to the Fermi level are mainly due to the transition metal-d orbitals. Removing O atoms or adding H atoms causes the conduction bands to shift down below the Fermi level, driving a semiconductor-to-metal phase transition. In the band structure of $Hf_2MnC_2O_2H_{0.11}$ in Fig. 4.2, only the spin-down electron bands cross the Fermi level, indicating this material is a half-metal.

### 4.3.3 Magnetic Properties

Our DFT calculations find that $Hf_2MnC_2O_2$ has a magnetic moment of $3\mu_B$ per formula unit while $Hf_2VC_2O_2$ has a moment of $1\mu_B$. See Table 4.4. Moreover, the magnetic moment on each Hf atom is negligible. This is consistent with all transition

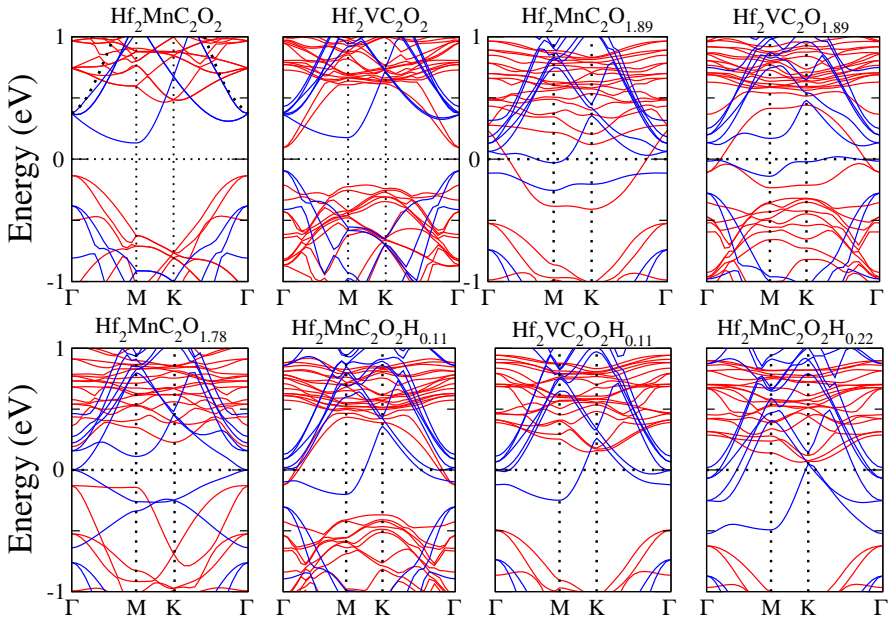


Figure 4.2: Spin-resolved band structures, calculated without SOC, for $Hf_2MnC_2O_2$ and $Hf_2VC_2O_2$ nanosheets with H adatoms or O vacancies. Red (blue) curves indicate spin-up (spin-down) bands. In some cases the system is half-metallic, with only spin-down bands crossing the Fermi level.

metal atoms being in the +4 oxidation state: $Hf^{4+}$ ions have lost all four valence electrons, whereas $Mn^{4+}$ retains 3 valence electrons and $V^{4+}$ retains 1. Hence it is rational to assume that the magnetic properties are dominated by the Mn or V atoms.[25]

For the purpose of constructing effective spin models, we designate every Mn/V atom as a magnetic center. There are nine such centers in a $3 \times 3$ supercell. The total magnetic moment associated with each center is calculated by integrating the magnetization (from the VASP output file) over the Wigner-Seitz cell of that center (i.e., over a hexagonal prism centered on the Mn/V atom). This scheme ensures that all the magnetization is accounted for, i.e., assigned to exactly one magnetic center. (This is in contrast to VASP's built-in routine, which integrates the magnetization over Wigner-Seitz spheres that may overlap, and may not fill space.)

In the absence of defects, every Mn center has the same magnetic moment ($3\mu_B$). Defects produce spatial fluctuations as shown in Fig. 4.4, generally of the order of

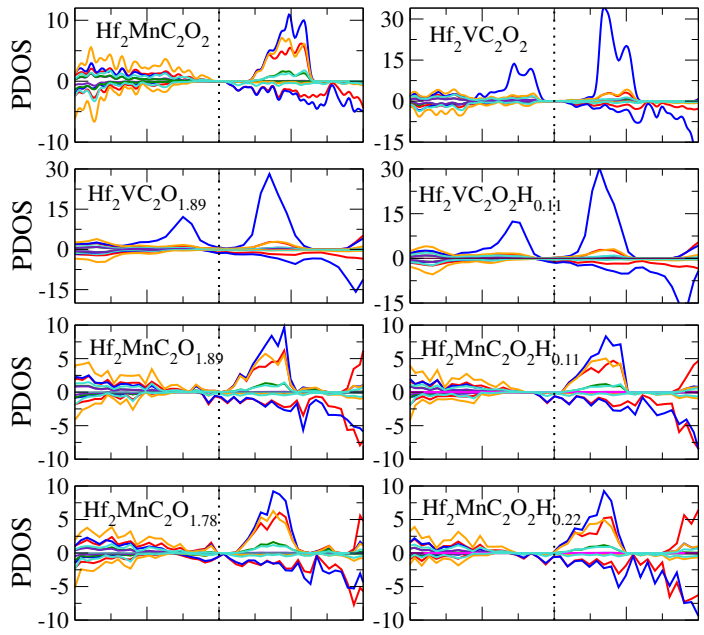


Figure 4.3: Partial densities of states of $Hf_2MnC_2O_2$ and $Hf_2VC_2O_2$ nanosheets with and without defects.

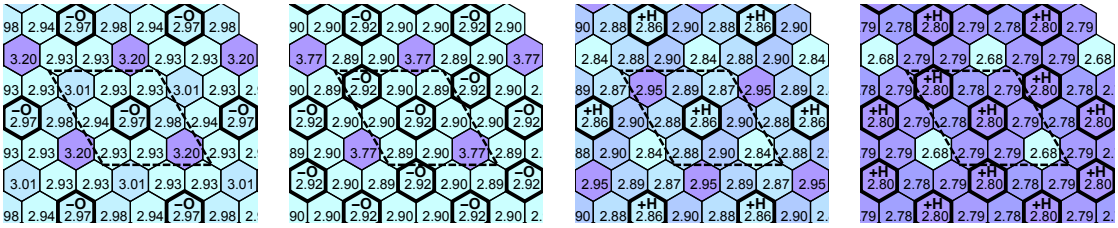

(a) 1 O vacancy (b) 2 O vacancy (c) 1 H adatom (d) 2 H adatoms

Figure 4.4: Magnetic moments in the 2D MXenes $Hf_2MnC_2O_{2-n/9}$ and $Hf_2MnC_2O_2H_{n/9}$ with 1 or 2 oxygen vacancies or hydrogen adatoms. Locations of these defects are indicated by labels ($-$O and +H). The magnetic moment associated with each $Mn^{4+}$ magnetic center is integrated over a Wigner-Seitz hexagonal prism as described in the text.

$0.1\mu_B$, in a manner consistent with the reduced symmetry of the system. A defect (e.g., O vacancy) on one surface reduces the $S_6$ symmetry axis to a $C_3$ axis. Also, the defect has the strongest effect *not* on the Mn center directly below it, but instead on the Mn center that appears to be the second neighbor. This suggests that magnetic effects are transmitted by the presence of slanted O–Hf–C–Mn chains, in a pattern with 3-fold symmetry. This explains why the magnetic centers at the far corners of the unit cell carry different moments in Fig. 4.4(a) and (c). In the case of $Hf_2MnC_2O_{1.78}$,

shown in Fig. 4.4(b), the removal of electronegative O atoms results in significantly increased electron density on the Mn atoms, increasing the magnetic moment up to 3.77 $\mu_{\mathrm{B}}$.

We define the magnetic anisotropy energy $\mathrm{MAE}(\theta, \phi)$ as the energy (per formula unit) when all spins are parallel with direction described by zenith angle $\theta$ (w.r.t. the $c$ axis) and azimuthal angle $\phi$. For a structure with hexagonal symmetry the leading terms in the MAE are

$$\mathrm{MAE}(\theta, \phi) = K_0 + K_1 \sin^2 \theta + K_2 \sin^4 \theta. \tag{4.1}$$

The nature of the anisotropy can be described as easy-axis (if $K_1 > 0$ and $K_2 > 0$) or easy-plane (if $K_1 < 0$ and $K_2 < 0$).

We performed DFT calculations, including spin-orbit coupling, where all spins were constrained to be at angle $\theta$ to the $c$ axis, for various values of $\theta$. Energies are plotted relative to the minimum energy. The MAE plots for the defect-free materials $Hf_2MnC_2O_2$ and $Hf_2VC_2O_2$ are shown in Fig. 4.5. The maximum MAE of $Hf_2MnC_2O_2$ and $Hf_2VC_2O_2$ are 56.77 $\mu$eV and 9.48 $\mu$eV; see Table 4.4. The larger MAE of $Hf_2MnC_2O_2$ can be partly attributed to the difference in atomic number $Z$, since MAE is directly proportional to $Z^4$. However, $Hf_2VC_2O_2$ has easy-plane anisotropy (minimum energy when $\theta = 90°$) whereas $Hf_2VC_2O_2$ has easy-axis anisotropy (minimum energy when $\theta = 0°$ or 180°). We obtained the parameters $K_1$ and $K_2$ for each material by fitting $\mathrm{MAE}(\theta, \phi)$ to a quadratic polynomial in $\sin^2 \theta$ (see Table 4.4).

It is clear that MAE is profoundly sensitive to surface defects. Adding H atoms to the $Hf_2MnC_2O_2$ surface switches the magnetic anisotropy from easy-plane to easy-axis and increases its magnitude significantly. Adding O vacancies causes large, non-monotonic changes in the magnetic anisotropy.

We first considered the defect-free materials $Hf_2MnC_2O_2$ and $Hf_2VC_2O_2$. As ex-

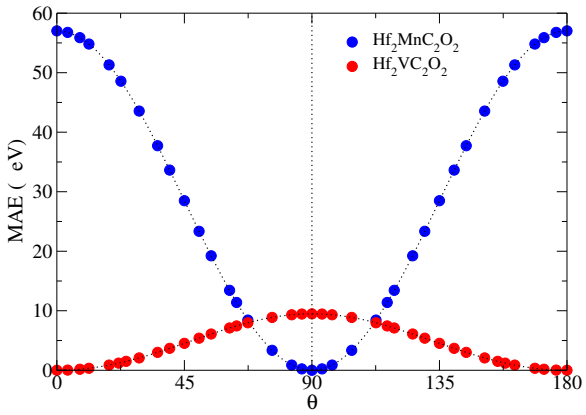


Figure 4.5: MAE of the defect-free MXenes as a function of $\theta$ when $\phi = 0$, calculated using DFT with SOC.

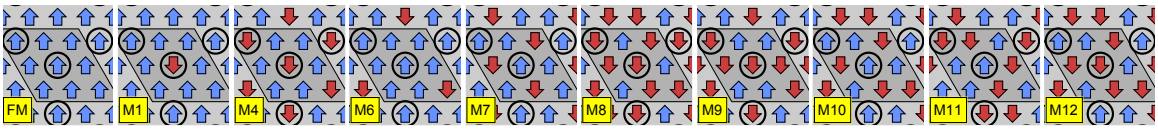


Figure 4.6: The 10 ferromagnetic and ferrimagnetic spin configurations used in the energy mapping analysis. Energies were calculated using DFT and used to fit effective exchange couplings $J_1, \ldots, J_9$ in a classical Heisenberg model. Defect sites ("1" and "2") are indicated by black circles.

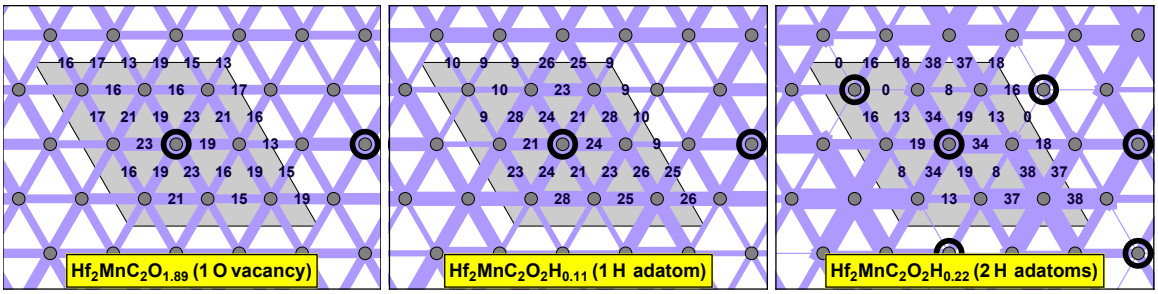


Figure 4.7: Exchange couplings $J_{ij}$ in the effective Heisenberg models for $Hf_2MnC_2O_{1.89}$, $Hf_2MnC_2O_2H_{0.11}$, and $Hf_2MnC_2O_2H_{0.22}$. In each case the nine symmetry-inequivalent nearest-neighbor exchange couplings $J_1, \ldots, J_9$ were determined by matching to DFT energies. Bold circles indicate defect locations. Line thicknesses and numbers indicate $J_{ij}$ (in meV). All couplings are ferromagnetic. The parent compound $Hf_2MnC_2O_2$ has a single coupling $J = 20.4$ meV; adding defects produces a pattern of strong and weak couplings, which raises the overall $T_c$.

plained above, the magnetic moment is dominated by the Mn/V atoms, which forms a single-layer hexagonal lattice. Although the crystal structure does not have $C_6$ symmetry, projecting it onto a single plane converts the $S_6$ axes into $C_6$ axes, so all

nearest-neigbor exchange couplings must be equivalent by symmetry. DFT calculations were performed with Mn/V spins in ferromagnetic configurations and collinear antiferromagnetic configurations (with alternating spins along the $a$ direction). For each spin configuration, the atomic positions and unit cell area were relaxed. The DFT energies (not shown) were used to determine the classical Heisenberg ferromagnetic nearest-neighbor exchange coupling $J$ in a standard energy mapping analysis.

Next, we considered the materials with 1 or 2 defects per $3 \times 3$ supercell. The supercell contains 27 nearest-neighbor bonds, but since the defect patterns preserve some $C_3$ symmetry axes, there are only 9 independent nearest-neighbor exchange couplings $J_1, \ldots, J_9$. We performed DFT calculations with Mn/V spins in 10 ferromagnetic and collinear ferrimagnetic configurations, as shown in Fig. 4.6. These configurations were selected to produce 10 linearly independent equations, allowing us to solve for $J_1, \ldots, J_9$ as well as a constant non-magnetic contribution to the energy, $E_0$. In principle, the single-spin anisotropy parameters $K_1$ and $K_2$ may also vary from site to site; however, the magnetic anisotropies are very small (of the order of $\mu$eV), and their main observable effect is to stabilize ferromagnetic order through the collective behavior of large patches of spins. Therefore it is justifiable to average the anisotropy over the entire supercell, which is implicit in the MAE calculations described in the previous section.

## 4.4 Conclusions

We have studied the electronic and magnetic properties of $Hf_2MnC_2O_2$ and $Hf_2VC_2O_2$ MXenes with surface defects (H adatoms and O vacancies), using density functional theory and Monte Carlo simulations. We find that defects have a significant influence on the band structures, magnetic moments, magnetic anisotropy, and exchange couplings. Defects shift the conduction bands down, driving semiconductor-metal transitions. In particular, $Hf_2MnC_2O_{1.78}$, $Hf_2MnC_2O_2H_{0.11}$, and $Hf_2VC_2O_2H_{0.22}$

(with defects located as described in the text) are predicted to be half-metals. Bare $Hf_2VC_2O_2$ has easy-axis anisotropy; bare $Hf_2MnC_2O_2$ has easy-plane anisotropy, but adding defects can change this to easy-axis anisotropy. Of the materials studied here, $Hf_2MnC_2O_2H_{0.22}$ is the most promising, with a predicted Curie temperature of about 171 K due to a combination of easy-axis anisotropy and a connected network of enhanced exchange couplings.

# CHAPTER V

# B-DOPED-GRAPHENE BASED ELECTRODES FOR Na- AND Mg-ION BATTERY APPLICATIONS

## 5.1 Introduction

Rechargeable ion-storage is one of the key concern for various applications, including electric vehicles, portable electronic devices, and power grids.[46,56] Lithium-ion batteries (LIBs) and Lithium-ion capacitors (LICs) have been widely studied for ion-storage devices as a result of their high specific capacity, energy density and power density, and lightweight.[46,138–140] Lack of availability and high cost of Li resources and safety concerns influence on discovering alternative mediums of storing Na and Mg. Na-ion batteries (SIBs) are the most popular substitution since Na is a low cost material with high abundance and availability.[46,53,141,142] Mg is also highly considered because of its bi-valency, i.e. two electrons are released from each Mg atom during the discharge process, whereas only one electron is involved in each of its Li and Na counterparts. Thus, magnesium ion batteries (MIBs) are able to store twice as much energy as than LIBs and SIBs. Mg is also a highly abundant and low cost material while the Mg atom is a lightweight atom which makes a promising element in ion-storage devices.[46,143,144]

$Ti_2CT_x$, which shows high volumetric capacity, is one of the lightest MXenes reported.[145] It was experimentally discovered that $Ti_2CT_x$ based electrodes exhibit excellent electrochemical performance.[20,146] Nevertheless, the delaminated MXene

nanosheets form bulk MXene flakes owing to restacking, which causes capacity fading.[147–149] As a solution to the issue of restacking of MXene sheets, the addition of carbon-related nanomaterials, such as carbon nanotubes (CNT) and nanosheets (graphene), between the MXene layers was introduced. These proposed sandwich-like structures not only prevent restacking but also enhance the capacity and the conductivity of electrodes.[20,139,148–150] It is also observed that oxygen-related surface terminations, like OH and O, provide increased capacity compared to F based termination.[56] Among OH and O functional groups, O terminated MXenes show higher binding energy between ions and the electrode. That is important to prevent forming bulk materials of intercalated ions such as bulk Li and Na.[151] Thus, among the different $Ti_2CT_x$ monolayers, $Ti_2CO_2$ can be chosen as the best material for ion-storage applications. Moreover, in order to enhance the properties of graphene based materials, doping with heteroatoms, like B, N, F, and O, is identified as an effective method to modulate the electronic and electrochemical properties. Substituting C with B is convenient due to the similar atomic sizes, which minimize the strain formed by doping. B-doped-graphene (B-Gr) sheet has been identified as a promising anode for potassium ion-battery applications with high specific capacity (546 $mAhg^{-1}$) with a low diffusion barrier (0.07 eV).[152] It has also been reported that doping graphene with B enhances the conductivity by altering the band structure.[152–155]

In this work, by considering all the above facts, we selected $Ti_2CO_2$/B-doped-graphene (B-Gr) heterostructure and B-Gr bilayer, as the electrodes for intercalating Na and Mg. Despite the fact that Na and Mg intercalated bare graphene bilayer electrodes are not energetically stable,[156–158] we are able to show that these ions can be stored in B-doped graphene bilayers with reasonable binding energies. It is already theoretically suggested that Na intercalation in the bilayer and multi-layer B-Gr sheets with high B concentration ($\approx 33\%$) is possible.[142] However, in this work, a moderate B concentration ($\approx 8\%$) was considered. This is a critical concentration

under which (such as 4%) the intercalation capacity of B-Gr bilayer largely reduces, showing the vital role of B concentration to enhance storage capacity. Mg inserted systems was found to show smaller interlayer distance change ($\leq 0.5$Å) than that of Na intercalated counterparts, indicating that Mg electrodes considered can be more stable against restacking during the charging/discharging process. The Na and Mg intercalated systems provide maximum average voltages higher than 1.2 V and 0.75 V, respectively. The gravimetric storage capacities computed for all systems are greater than 240 mAh/g$^{-1}$.

## 5.2 Computational Methods

We performed density functional theory (DFT) calculations based on Vienna itab initio simulation package (VASP),[74–77] where plane-wave basis set was used with a 500 eV energy cutoff. The electron-ion interaction was taken into account by using projected augmented wave (PAW) method.[81,82] The generalized gradient approximation (GGA) based exchange-correlation potential was considered with the Perdew-Burke-Ernzerhof (PBE) pseudopotentials.[100,101] The convergence criteria for energy and force were set to $10^{-5}$ eV and 0.001 eV/Å, respectively. We used a vacuum space of at least 15 Åin order to prevent the spurious interaction along the $z$-direction (vacuum direction). The $\Gamma$ centered 5×5×1, and 12×12×1 Monkhorst-Pack $k$-meshes were considered for the structural optimization of $Ti_2CO_2$ $(4 \times 4)$/B-Gr $(5 \times 5)$ and B-Gr/B-Gr $(2\sqrt{3} \times 2\sqrt{3})$ super-cell structures, respectively. In order to realize lower intercalated ion concentrations for B-Gr bilayers, a single ion intercalated $4\sqrt{3} \times 4\sqrt{3}$ supercell was considered. For all other Na/Mg concentrations, a $2\sqrt{3} \times 2\sqrt{3}$ B-Gr supercell was used (see Appendices). We included van der Waals (vdW) interactions for heterostructures and the bilayers using the DFT-D3 method, including Becke-Jonson damping.[106,107] The charge transfer from ions to the nanosheets was studied using Bader charge analysis.[159] The climbing image nudged elastic band (CI-NEB)

method, which is implemented in the VASP transition state tools, was employed with nine images (including initial and final positions) to calculate the minimum energy diffusion paths.[83,160]

## 5.3 Results

### 5.3.1 Structure Optimization

The concentration of B atom in B-Gr/B-Gr system was kept as $\approx 8\%$ . Each layer in a $2\sqrt{3} \times 2\sqrt{3}$ supercell of B-Gr bilayer was doped with two B atoms. As shown in Fig. A10 in the Appendices, when the B percentage is 4%, the voltage of the Na intercalated B-Gr bilayer becomes negative at a lower ionic concentration compared to the voltage of 8% B-doped system. Consequently, a lower capacity can be expected when the doping concentration is less than 8%, as illustrated in TABLE A5 (see Appendices). Accordingly, we selected 8% as the doping concentration for the graphene sheets. To be consistent, in $Ti_2CO_2$/B-Gr heterostructures, the graphene layer was also doped with 8% B concentration.

In order to minimize the lattice mismatch between MXene sheet and the B-doped graphene layer, a $4 \times 4$ supercell of $Ti_2CO_2$ was combined with a $5 \times 5$ super cell of B-Gr. The optimized lattice parameters for the MXene layer and the B-Gr layer are 12.50 and 12.07 Å, respectively. Thus, the lattice mismatch between these two sheets is calculated as 3.47%. In order to make them fit in the same periodic cell, we applied a 1.73% compressive strain on the B-Gr layer and a 1.73% tensile strain on the MXene layer. After relaxing the heterostructure, the optimized lattice parameter becames 12.29 Å. As a result, MXene nanosheet contains 1.67% tensile strain, whereas B-Gr nanosheet has 1.85 % compressive strain. The interlayer separation of bare heterostructure (i.e., $Ti_2CO_2$/B-doped graphene) is calculated as 2.98 Å which is almost equal to the $Ti_2CO_2$/pristine-Gr interlayer separation (3.00 Å).[151] To find the

ground state structure of B-Gr bilayer, we shifted the top layer with respect to the bottom layer and compared the total energies of the systems. This was done for the ion-free B-Gr/B-Gr system and also all the single and multiple ion intercalated bilayers (see Appendices). The interlayer binding energies per atom ($E_{\mathrm{b}}$) was obtained according to Eq. 5.1 and 5.2 for ion-free B doped graphene bilayer and MXene based heterostructure, respectively, as follows;

$$E_b = \frac{1}{\mathrm{N}}(E[\mathrm{B-Gr/B-Gr}] - 2 \times E[\mathrm{B-Gr}]) \tag{5.1}$$

and

$$E_b = \frac{1}{\mathrm{N}}(E[\mathrm{Ti_2CO_2/B-Gr}] - E[\mathrm{Ti_2CO_2}] - E[\mathrm{B-Gr}]) \tag{5.2}$$

Here, $E[\mathrm{Ti_2CO_2/B-Gr}]$ and $E[\mathrm{B-Gr/B-Gr}]$ are the total energy of the respective systems without ions. The total energy of a single MXene layer and B-Gr layer are given by $E[\mathrm{Ti_2CO_2}]$ and $E[\mathrm{B-Gr}]$, respectively. $N$ is the total number of atoms in each system without ions. It is found that the calculated binding energies are negative, which indicates that the considered bilayer and heterostructure are energetically stable against separation to isolated layers. TABLE 5.1 summarizes the interlayer separations and $E_{\mathrm{b}}$ for bare structures. As a reference, those quantities were also calculated for undoped graphene bilayer. It is found that AB stacking is the most stable stacking type as same as bare graphene bilayer[151,161] (see Fig. A11 in Appendices).

### 5.3.2 Single ion intercalation

We next studied single Na/Mg intercalation. In $\mathrm{Ti_2CO_2}$/B-Gr heterostructure, positively charged Na and Mg reside closer to the bottom O layer of $\mathrm{Ti_2CO_2}$. The ions are inserted at the middle of the triangles formed by the O atoms (see Fig. 5.1(a)).

Table 5.1: The binding energy ($E_b$) and interlayer distance ($d_0$) for ion-free systems. Both AA and AB stacking types were consideres for graphene undoped and doped bilayers.

| System | $E_b$ (eV/atom) | $d_0$ (Å) |
|---|---|---|
| $Ti_2CO_2$/B-Gr | -0.0086 | 2.98 |
| B-Gr/B-Gr (AB) | -0.0251 | 3.35 |
| B-Gr/B-Gr (AA) | -0.0237 | 3.46 |
| $Ti_2CO_2$/Gr[151] | -0.0180 | 3.00 |
| Gr/Gr (AB) | -0.0241 | 3.36 |
| Gr/Gr (AA) | -0.0200 | 3.58 |

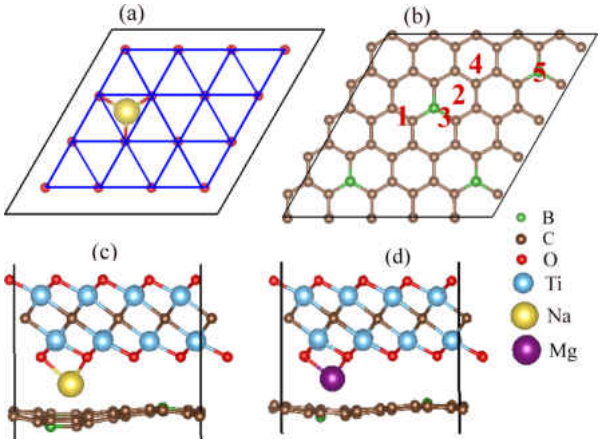


Figure 5.1: Examples of single ion intercalated $Ti_2CO_2$/B-Gr system where (a) position of the ion with respect to the bottom O layer of $Ti_2CO_2$, (b) possible adsorption sites for an ion with respect to B-Gr layer, (c) side view of a Na ion intercalated at site 3, and (d) side view of a Mg intercalated at site 3.

As a result of distinct atomic surroundings in B doped graphene sheet, five different initial sites are identified to intercalate a single ion. The sites labeled from 1 to 5 are (1) middle of C-C bonds, (2) hollow site of a honeycomb formed by C and B atoms together, (3) middle of C-B bonds, (4) hollow site of a honeycomb which is away from B atoms and (5) right above the B atoms, respectively (see Fig 5.1 (b)). The B atoms close to the inserted ion are shifted from the graphene plane as a consequence of the repulsive interaction between B and Na/Mg. Thus, the B-Gr sheet in $Ti_2CO_2$/B-Gr system bends, as shown in Fig. 5.1(c) and (d).

The binding energy, $E_b$, of Na and Mg inserted into $Ti_2CO_2$/B-Gr and B-Gr/B-Gr

systems were calculated using following expression,

$$E_b^{\mathrm{A}} = \frac{1}{x}[E(\text{System with A}) - E(\text{System}) - xE(\text{A})] \tag{5.3}$$

where $E$(System with A) is the system with ion A (Na or Mg), $E$(System) is the system without an ion, $E$(A) is the total energy of a Na or Mg atom extracted from their bulk phases, and $x$ is the total number of intercalated ions. Na and Mg bulk materials were considered with body centered cubic (BCC) and hexagonal structures, respectively. According to our binding energy definition, more negative binding energy ($E_b$) implies a stronger bonding between the system and the ions.

Table 5.2: Binding energy for a single Na/Mg ion at each site in $Ti_2CO_2$/B-Gr systems.

| Site | 1 | 2 | 3 | 4 | 5 |
|---|---|---|---|---|---|
| $E_b^{\mathrm{Na}}$ (eV/atom) | -1.715 | -1.877 | -1.863 | -1.682 | -1.764 |
| $E_b^{\mathrm{Mg}}$ (eV/atom) | -2.503 | -2.526 | -2.552 | -2.134 | -2.437 |

As evidenced by TABLE 5.2, the binding energies of the Na and Mg are negative for all the sites considered for $Ti_2CO_2$/B-Gr system. This implies that all five sites are energetically possible for ion intercalation. The sites 2 and 3 exhibit lower binding energies than that of the other three sites for Na and Mg.

Since Na (Mg) is expected to donate its 3s electron(s), B-substituted graphene (an electron deficient system) can better accommodate these extra electron(s) as compared to pristine graphene. In order to elucidate how the electrons are localized in B-Gr sheet, we calculated the charge distribution for one of the layers of a B-Gr and Gr-Gr bilayer without ions intercalated. We observed similar behavior in B-Gr sheets of all the systems considered in this work. As shown in Fig. 5.2 (a), the charge density plot shows that the electrons of the B atoms transfer to the C atoms adjacent to the B atoms due to a considerable electronegativity difference between B and C atoms. Thus, the uneven distribution of charge between C and B atoms make polar-covalent

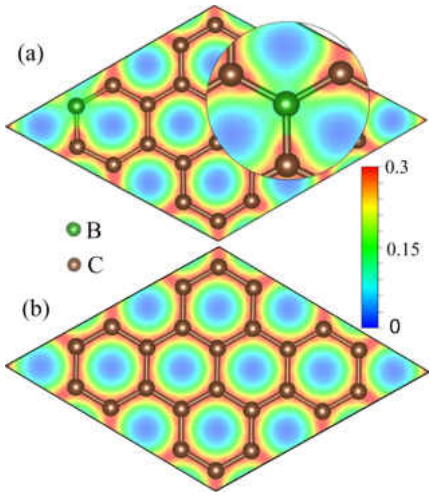


Figure 5.2: The charge distribution for one of layers of (a) B-Gr/B-Gr and (b) Gr/Gr bilayers. The zoomed area of part (a) shows the charge distribution around the B atom.

bonds, where C is negatively charged compared to the adjacent B atoms. Therefore, the positively charged Na/Mg prefers to reside at the hollow site formed by the C and B atoms. Accordingly, the binding energy at site 5 is higher than that at sites 2 and 3, because of the repulsion between positively charged B and Na/Mg . The attractive ionic interaction between the ion and the negatively charged C atoms enhances the binding energy. As a result of the higher positive charge per Mg ion than that per Na ion, Mg ion has lower (more negative) binding energy (see Table 5.2).

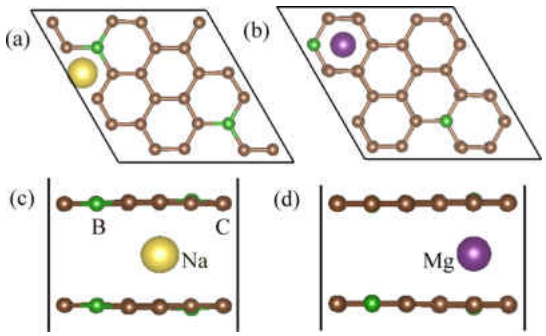


Figure 5.3: (a) Top and (c) side view of a single Na intercalated B-Gr/B-Gr system, and (b) Top and (d) a side view of a single Mg intercalated B-Gr/B-Gr system.

The ion intercalation is energetically more stable for AA stacking of the B-Gr/B-Gr system. The ion in the B-Gr/B-Gr system resides at the hollow site, as seen in

Fig. 5.3. B-Gr bilayer keeps a higher interlayer distance ($\approx$ 4.20 Å for Na and 3.67 Å for Mg) than that of heterostructure. This is mainly due to the strong interaction between the constitute layers and intercalated ions in the latter. In addition, we observed that Na/Mg ions, which stay closer to the C-B bonds, provide lower binding energies. This implies that the polar-covalent C-B bond/positively charged intercalated ion interaction plays a crucial role in enhancing the stability of intercalation in the B-Gr/B-Gr system. The calculated single ion binding energies, i.e., $E_b^{\mathrm{Na}}$ and $E_b^{\mathrm{Mg}}$, in a $4\sqrt{3} \times 4\sqrt{3}$ supercell are -1.194 eV and -1.702 eV, respectively. The weaker binding energies in B-Gr bilayers than that in $Ti_2CO_2$/B-Gr system is a consequence of the weaker interaction between ions and the B-doped graphene layers. Due to the O-layer of $Ti_2CO_2$, positively charged ions are highly attracted by the MXene sheet. Thus, the binding of intercalated ions is stronger in the $Ti_2CO_2$/B-Gr system.

We also calculated the Na and Mg binding energies for bare Gr/Gr bilayer. Our calculations showed that binding energy values are positive ($E_b^{\mathrm{Na}} = 0.343$ eV and $E_b^{\mathrm{Mg}} = 1.718$ eV) for bare bilayer graphene system indicating that Na and Mg intercalation are not energetically favorable.

### 5.3.3 Multiple Ion Intercalation

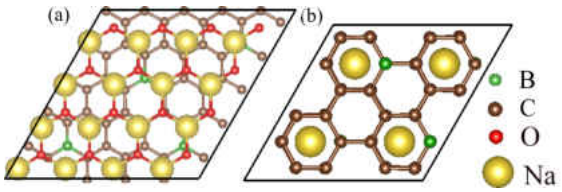


Figure 5.4: Maximum number of Na ions intercalated in (a) $Ti_2CO_2$ $(4 \times 4)$/B-Gr $(5 \times 5)$ and (b) B-Gr/B-Gr $(\sqrt{3} \times \sqrt{3})$ super cells. For clarity, only B-Gr layer and the bottom O layer are visible for $Ti_2CO_2$/B-Gr case.

In addition to single-ion intercalation, we investigated the multiple ions inserted systems to explore the variations in the structure, binding energies, charge transfer, and electronic structure. In Fig. 5.4, the systems with the maximum number of

intercalated Na ions are presented. Here, maximum number of ions means the highest number of intercalants which can be stored, while the voltage remains positive. For clarity, we showed only the bottom O layer of $Ti_2CO_2$ and B-Gr layer in Fig. 5.4(a). Due to the stronger attraction between the O layer and Na/Mg, we are able to intercalate a large number of ions, even though they are located close to each other.

As discussed before, the layers of Li intercalated graphene bilayer move with respect to each other and transform from AB stacking to AA stacking.[161,162] This kind of layer displacement is also possible for B-Gr bilayers. In order to find the lowest energy structure of B-Gr bilayer, B-Gr monolayers are allowed to move with respect to each other, while ions are intercalated. As a consequence, the relative orientation of B-Gr layers of B-Gr bilayer may be different for different intercalated ion concentrations. In Appendices, we showed examples for distinct supercell configurations as a function of ionic concentration. Those supercells were used to model the 0.004, 0.02, 0.03, 0.05 and 0.06$Å^{-2}$ intercalated ion concentrations for B-Gr bilayers, as shown in Fig. A12 to A21 (see Appendices). When two B atoms at different layers are positioned close to each other, a Na or Mg ion prefers to reside near those areas in a single ion intercalation case. B atoms donate their valence electrons to the adjacent C atoms, forming polar regions that strongly interact with positively charged intercalant. It is found that the total energy is minimum when the B atoms of the top and bottom layers are located close to each other in the 0.02$Å^{-2}$ concentration (Fig. A13 (a) for Na and Fig. A18 (a) for Mg) and 0.03$Å^{-2}$ concentration (Fig. A14 (a) for Na and Fig. A19 (a) for Mg). In multiple ions intercalated systems, the total energy is minimum when the B-B distance in the different layers increases. For a 0.06$Å^{-2}$ ion concentration, both layers move with respect to each other in such a way that at least one B atom is placed close to one ion to minimize the total energy of the system as shown in Fig. A16 (a) and Fig. A21 (a) (see Appendices ).

Figure 5.5 shows the variation of binding energy ($E_b^A$; A=Na/Mg) as a function

of ion concentration ($\alpha$). $\alpha$ for each system was computed using $\alpha = \frac{x}{\mathrm{S}}$, where $x$ is the number of intercalated ions and S is the surface area of the considered system. S was calculated using $\mathrm{S} = \frac{\sqrt{3}}{2}a^2$, where $a$ is the lattice constant of the system. It is clear that $E_b^A$ increases (meaning that the stability of intercalation weakens) in all systems, while $\alpha$ increases except at low Na concentrations in B-Gr/B-Gr bilayer. The enhanced repulsive ion-ion interaction due to the reduced inter-ionic distances at higher ion concentrations results in a weaker binding of ions within the considered systems.[151] Nevertheless, $E_b^{Na}$ increase in B-Gr/B-Gr system can be attributed to an abrupt increase in interlayer separation (0.23 Å change) at low Na concentrations as explained for Graphene/$MoS_2$ electrodes with Li.[163] $E_b^{Na}$ rises like in the other systems after 0.03 $Å^{-2}$ since the interlayer gap remains approximately unchanged. Since Na intercalated systems maintain relatively strong binding energy over a wide Na concentration, a greater number of Na ions can be intercalated in both systems without clustering of Na ions. In contrast, $E_b^{Mg}$ exhibits strong concentration dependence due to much larger ion-ion repulsion between $Mg^{2+}$ ions. In B-Gr bilayer, $E_b^{Mg}$ becomes almost zero at $\alpha = 0.06Å^{-2}$. However, it should be noted that partial intercalation of Mg in a given system is able to provide higher capacity due to its bi-valency.

Na has a larger ionic radius as compared to Mg, giving rise to a more significant downward displacement of B atom from the graphene plane in the Na intercalated heterostructure. We also studied the interlayer spacing change based on the equation $\Delta = d - d_0$, where $d$ is the distance between the layers of a system with ions, and $d_0$ is that of an ion free system. As illustrated by TABLE 5.3, Na intercalation results in a 1.00 Å average interlayer distance variation while Mg intercalated systems have an average interlayer separation change of around 0.38 Å. Thus, Mg intercalated systems show a minimal interlayer distance variation. That can be exploited to avoid restacking of layers during the ion charging/discharging processes, thereby providing

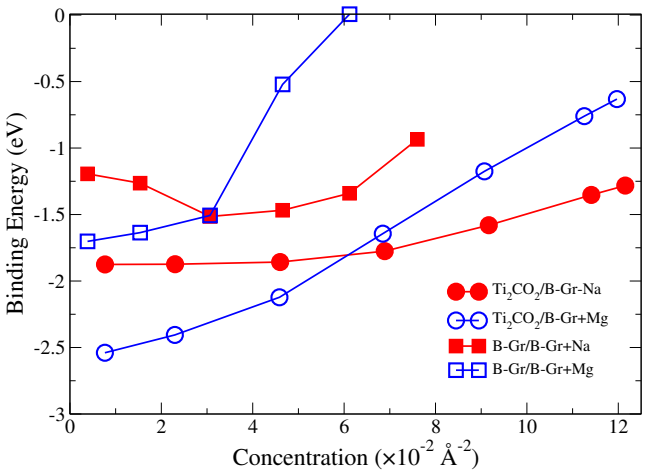


Figure 5.5: Binding energy per ion of Na and Mg intercalated systems as a function of intercalated ion concentration.

good mechanical stability.

Maximum in-plane lattice parameter expansion occurs at $0.12\text{Å}^{-2}$ and $0.06\text{Å}^{-2}$ concentration for $Ti_2CO_2$/B-Gr and B-Gr/B-Gr systems, respectively. Na intercalated systems show tiny lattice constant changes (less than 0.3%). Mg intercalated $Ti_2CO_2$/B-Gr heterostructure exhibits 1% expansion while that of B-Gr bilayer is 0.9% at $\alpha = 0.06\text{Å}^{-2}$. In the heterostructure, less than a 2.9% tensile strain should be applied on MXene layer to obtain the maximum expansion, while less than 1.4% compressive strain is required for B-Gr layer. Thus, the ion adsorption does not alter in-plane lattice parameters significantly. Small in-plane parameters expansions with the interlayer spacing change during charging provide that considered systems exhibit a volume change of around 15-40%. Volume expansion for Mg intercalated B-Gr bilayer and heterostructure is around 15% and 16%, respectively. However, in the Na intercalated systems, the calculated maximum volume expansion is found to be 35% for the bilayer and 40% for the heterostructure due to the larger size of Na. Such volume change is more than 300% for Si, Ge, and Sn-based Li-ion electrodes.[167–169]

Another important finding of this research is that both Na and Mg are able to donate almost all their valence electrons to the systems. The Bader charge analysis

Table 5.3: The average interlayer distance change $\Delta d_{\text{avg}}$, the maximum voltage ($V_{\text{max}}$), the average voltage ($V_{\text{avg}}$),the gravimetric capacity ($C_g$), and the energy barrier ($E_{\text{diff}}$) for the largest stable ion concentrations for the Na and Mg. $V_{\text{avg1}}$ was calculated from Eq. 5.5, where $\alpha_1 = 0\text{Å}^{-2}$ and $\alpha_2 = 0.12\text{Å}^{-2}$ for heterostructures, while $\alpha_2 = 0.06\text{Å}^{-2}$ for bilayers. $V_{\text{avg2}}$ was calculated using $\sum V_i/N$, where i is the step number and N is the number of steps in Fig.5.9.

| System | $\Delta d_{\text{avg}}$(Å) | $V_{\text{max}}$(V) | $V_{\text{avg1}}$(V) | $V_{\text{avg2}}$(V) | $C_g$(mAh/g) | $E_{\text{diff}}$ (eV) |
|---|---|---|---|---|---|---|
| $Ti_2CO_2$/B-Gr+Na | 1.04 | 1.88 | 1.28 | 1.27 | 240.4 | 0.46 |
| $Ti_2CO_2$/B-Gr+Mg | 0.37 | 1.27 | 0.82 | 0.92 | 295.1 | 1.43 |
| B-Gr/B-Gr+Na | 1.00 | 1.19 | 1.34 | 1.32 | 283.8 | 0.18 |
| B-Gr/B-Gr+Mg | 0.38 | 0.85 | 0.75 | 0.79 | 320.6 | 1.23 |
| $Ti_2CO_2$/undoped-Gr+Na[164] | ≈0.7 | ≈1.25 | 1.00 | - | 240.0 | ≈0.30 |
| $V_2CO_2$/undoped-Gr+Na[164] | ≈0.7 | ≈2.00 | 1.44 | - | 236.7 | ≈0.30 |
| $V_2C$/$V_2C$+Na[165] | - | 3.5 | - | - | 50.0 | - |
| Hard-C+Na[142] | - | - | - | - | 300.0 | - |
| B-Gr (highly doped)+Na[142] | - | - | 0.44 | - | 762.0 | 0.22 |
| B-Gr/B-Gr (highly doped)+Na[142] | - | - | 0.75 | - | ≈580 | - |
| 3D-B-Gr (highly doped)+Na[142] | - | - | 1.25 | - | ≈400 | - |
| 3D-$Ti_3C_2T_x$+Na[166] | - | 0.5-2.5 | - | - | 295.0 | - |
| 3D-$Ti_3C_2T_x$+Mg[144] | 1.90 | 2.85 | - | - | 210.0 | - |
| $MnO_2$/crystaline water+Mg[46] | - | - | 2.80 | - | 231.1 | - |

shows that the average Bader charge on Na is approximately $+1.00e$ ($+0.991e$ at a low ionic concentration of both systems), indicating that it completely donates its $3s^1$ electron to the systems. The Mg atom contributes exactly 2 electrons. Moreover, this trend persists as the ionic concentration is increased, except in the Na intercalated heterostructure, where it drops to $+0.987e$ at $0.12\text{Å}^{-2}$ concentration. On the contrary, Li intercalated MXene/Graphene heterostructures grant charge less than $+0.89e$, and it drops as the ionic concentration rises.[151] That is mainly because of the electronegativity difference between Na and Li. The former has a larger tendency to donate electron.

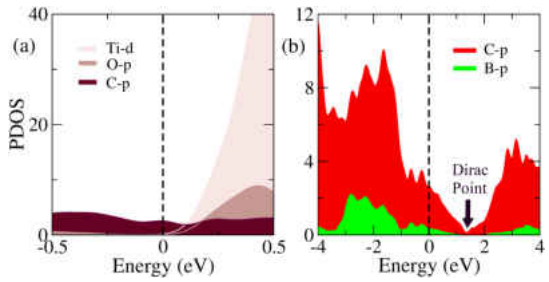


Figure 5.6: Partial density of states (PDOS) for ion free (a) $Ti_2CO_2$/B-Gr and (b) B-Gr/B-Gr systems. Here, the contributions from the orbitals, which are not mentioned, are negligible. Fermi energy is at zero energy.

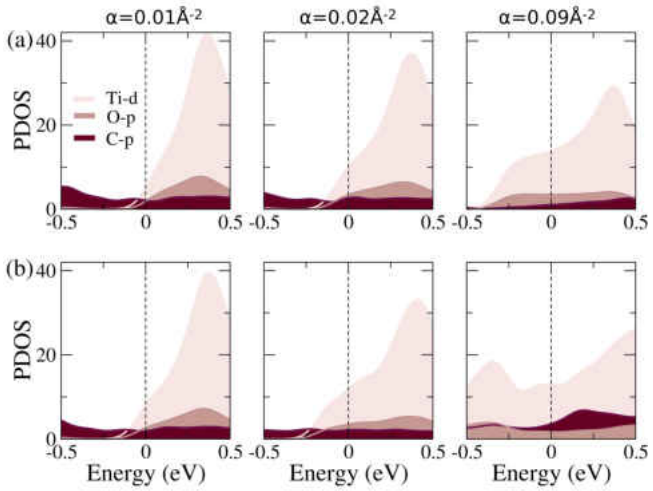


Figure 5.7: Partial density of states (PDOS) for (a) Na and (b) Mg intercalated in the $Ti_2CO_2$/B-Gr heterostructure with different intercalated ionic concentrations ($\alpha$). Here, the contributions from the orbitals, which are not mentioned, are negligible. Fermi energy is at zero energy.

Figure 5.6(a) includes the density of states (DOS) of ion free $Ti_2CO_2$/B-Gr heterostructure. It is clear that Ti-*d* orbitals dominate the DOS in the lower conduction band region. Figures 5.7 and 5.8 show how the DOS of considered systems changes as a function of ion concentration. It can be noted that the first peak of Ti-*d* orbital in the conduction band attenuates at high ionic concentration while enhancing the region of the valence band spanned by this orbital. This is a consequence of the charge transfer from the intercalated ions to the unoccupied *d* states of Ti atoms and *p* states of O atoms in MXene layer. As the ionic concentration increases, the Fermi level moves towards higher energies as a result of acquired electrons. Moreover, same as in the bare graphene monolayer, the bare graphene bilayer is also a semimetal with a zero bandgap, where two $\pi$ bonds contact at K point in the reciprocal space.[170] As a result, the valence and conduction density of states of C-*p* orbitals touch each other at the Fermi level. As pristine graphene is substitutionally doped with B, the Fermi level moves towards lower energies due to the p-type doping.[170] Thus, it can be observed in Fig. 5.6 (b) that the Dirac point appears in the valence band in the ion free case. As the intercalated ion concentration increases, the *p* states gain more electrons

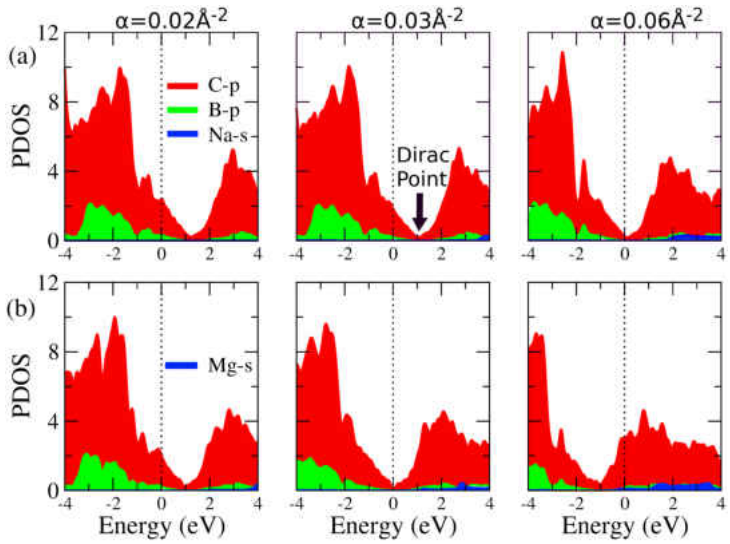


Figure 5.8: Partial density of states (PDOS) for (a) Na and (b) Mg intercalated B-Gr/B-Gr bilayer at different ionic concentrations ($\alpha$). Fermi energy is at zero energy.

from the ions. Accordingly, the Fermi level moves to higher energies. The DOS in Fig. 5.8 were calculated using a $2\sqrt{3}\times 2\sqrt{3}$ supercell of B-Gr bilayer which was doped with four B atoms. Since each B atom has one electron less than that of C, these B atoms donate four holes to the system. When the four Na ions ($0.06\text{Å}^{-2}$ concentration) are intercalated within the B-Gr bilayer, four electrons are provided to the system, saturating the electron deficient boron-carbon bonds. As a result of all holes being occupied by the electrons, the Dirac point appears at zero energy at $0.06\text{Å}^{-2}$ Na concentration. This happens at $0.03\text{Å}^{-2}$ ion concentration for Mg, since Mg is able to contribute electrons twice as much as that from Na at a given concentration.

### 5.3.4 Electrochemical Properties

The open-circuit voltage of an electrode is calculated using Gibbs free energy which is given by $G(\alpha) = \Delta E + P\Delta V - T\Delta S$. Due to the fact that $P\Delta V \approx 10^{-5}$ eV and $T\Delta S \approx 25$ meV at room temperature,[51,171] these terms make negligible contributions. Hence, we are able to approximate the average voltage by computing $\Delta E$ (internal energy change) using first-principle calculations within the range of number

concentration $\beta_1 \leq \beta \leq \beta_2$ based on Eq. 5.5 for the following chemical reaction,

$$(\beta_2 - \beta_1)\mathrm{A}^{z+} + z(\beta_2 - \beta_1)e^- + \mathrm{A}_{\beta_1}\gamma \leftrightarrow \mathrm{A}_{\beta_2}\gamma \tag{5.4}$$

where $\gamma$ represents $Ti_2CO_2$/B-Gr or B-Gr/B-Gr systems, while A denotes either the Na or Mg. The valency ($z$) of Na and Mg were considered as +1 and +2, respectively. $\beta$ is calculated as $\beta = \frac{x}{x_{\max}} \times 100$, where $x$ is the number of intercalates and $x_{\max}$ is the maximum number of ions that can be intercalated for a given supercell. Then, the average voltage for this reaction can be written as

$$V \approx \frac{E[\mathrm{A}_{\beta_1}\gamma] - E[\mathrm{A}_{\beta_2}\gamma] + (\beta_2 - \beta_1)E[\mathrm{A}]}{z(\beta_2 - \beta_1)e} \tag{5.5}$$

Here, $E$[A] is the total energy of metallic Na or Mg atom (extracted from bulk calculations), while $E[\mathrm{A}_{\alpha_1}\gamma]$ and $E[\mathrm{A}_{\alpha_2}\gamma]$ are the total energies of the systems with $\alpha_1$ and $\alpha_2$ concentrations of ions, respectively.

At low concentrations, the Mg intercalated systems exhibit lower voltages than that of the Na intercalated ones as shown in Fig. 5.9. The maximum voltages ($V_{max}$) are calculated as 1.27 V and 0.85 V for $Ti_2CO_2$/B-Gr, and B-Gr/B-Gr systems with Mg, respectively. Na intercalated $Ti_2CO_2$/B-Gr and B-Gr/B-Gr electrodes provide a $V_{max}$ of 1.88 V and 1.19 V, respectively. We observed abrupt voltage increses in the Na intercalated B-Gr/B-Gr bilayer at low concentrations. As in the case of binding energy shown in Fig. 5.5, this happens due to the significant interlayer separation change upon Na intercalation, which affects the intercalation energetics. After a Na concentration of $0.03\text{Å}^{-2}$, the voltage decreases as that in the other systems since the interlayer change is insignificant. Moreover, the average voltage for Mg intercalation becomes negative at around $0.07\text{Å}^{-2}$ in $Ti_2CO_2$/B-Gr electrode and $0.03\text{Å}^{-2}$ in B-Gr/B-Gr electrode. This indicates that we can expect the formation of metallic Mg for concentrations larger than those critical values, which is detrimental for battery

applications. Thus, 0.06Å$^{-2}$ concentration of Na can be intercalated without forming bulk Na.

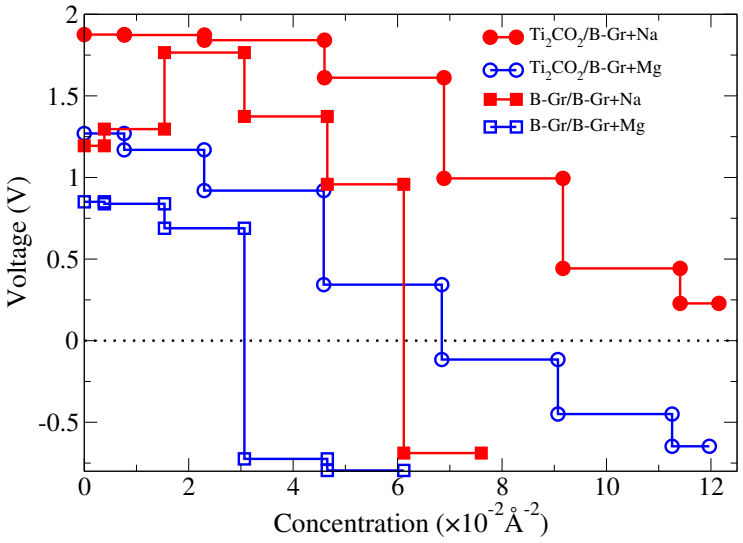


Figure 5.9: Open circuit voltage as a function of ion concentration

The theoretical gravimetric capacity, $C_g$ (mAh/g), can be obtained using

$$C_g = \frac{x_{\max} \times z \times F \times 10^3}{M_{A\gamma}} \tag{5.6}$$

where $x_{\max}$ is the maximum number of ions, which can be intercalated in a given system. $F$ is the Faraday constant (26.81 Ah/mol), and $M_{A\gamma}$ is the total atomic mass of the system with the maximum number of intercalated ions.[51] The $C_g$ values we calculated are 240.4 mAh/g for $Ti_2CO_2$/B-Gr with Na, 295.1 mAh/g for $Ti_2CO_2$/B-Gr with Mg, 283.8 mAh/g for B-Gr/B-Gr with Na and 320.6 mAh/g for B-Gr/B-Gr with Mg. It is clear that the B-Gr bilayers provide higher capacity than that of MXene based heterostructures due to the lower atomic mass of B-Gr sheets. As discussed before, the maximum concentration that can be inserted is limited due to the fact that the average voltage becomes negative for the Mg intercalation at a lower concentration than that for Na electrodes. But, it is worth noticing that Mg intercalated systems provide higher capacities than the respective Na electrodes because of the

bivalency of Mg. TABLE 5.3 includes $C_g$ values of several Na and Mg electrodes. The proposed heterostructure and bilayer for the Mg intercalation in this work provide higher capacity than that of 3D $Ti_3C_2T_x$ electrodes with Mg.[144] On the other hand, Na intercalated B-Gr based systems show lower capacity than that of 3D $Ti_3C_2T_x$ with Na.[166] Highly doped B-Gr monolayers provide higher Na capacity, which is more than twice the capacity of mildly doped bilayers of this study.[142] Experimentally realized $V_2C$ /$V_2C$ electrodes with Na exhibit incredibly high maximum voltage, even though the capacity is as low as 50 mAh/g.[165] It should be emphasized that the Na based heterostructure and bilayer introduced in this research provide higher (lower) $V_{max}$ ($C_g$) than that of it's Mg counterparts.

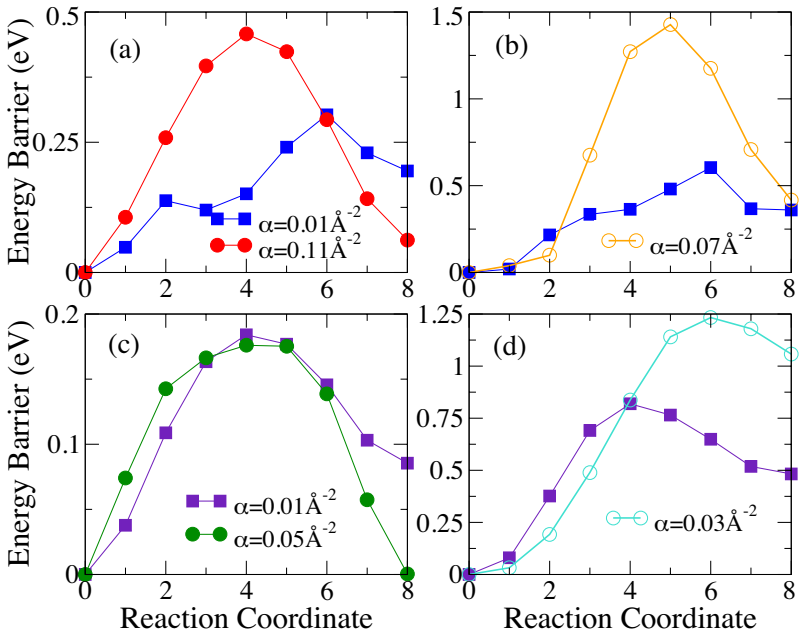


Figure 5.10: The diffusion barrier profile for $Ti_2CO_2$/B-Gr system with (a) Na and (b) Mg, and also B-Gr/B-Gr system with (c) Na and (d) Mg at different ionic concentrations ($\alpha$).

### 5.3.5 Diffusion Barrier

In order to study how easily Na and Mg are able to diffuse from one site to another between the layers in the respective systems, CI-NEB calculations were carried out as

illustrated by Fig. 5.10. A low diffusion barrier is important for high ionic mobility, which causes improving the charging and discharging rates. The Bader charge transfer calculations evidence that a Mg atom exhibits higher charge transfer than that from a Na since Na is a monovalent element and Mg is a bivalent element. The repulsive Coulomb interaction between Mg, and also attractive interaction between 2D sheets and intercalated Mg are stronger than those interactions for Na. As a result, the diffusion barrier in Na intercalated systems is considerably smaller compared to the Mg intercalated systems. In addition, Na intercalated systems have larger interlayer separations, making Na diffusion easier. As shown in Fig 5.4 (b), the ions are located close to each other in the MXene based system at high ion concentrations, which may significantly modify the barrier energies and diffusion paths. However, at low concentrations, ions, which move from one adsorption site to another, experience a low repulsion from other ions. When a higher number of ions presents, diffusion of ions is harder due to the large repulsive interaction. Therefore, the energy barrier is low at $\alpha = 0.01\text{Å}^{-2}$, while that is high at $\alpha = 0.11\text{Å}^{-2}$ in Fig. 5.10(a) for MXene based structures. For instance, while the diffusion barrier of Na at $\alpha = 0.01\text{Å}^{-2}$ is calculated as 0.30 eV, it becomes 0.46 eV for $\alpha = 0.11\text{Å}^{-2}$. On the contrary, the ions are inserted relatively apart from each other in B-Gr bilayers. At $\alpha = 0.04\text{Å}^{-2}$, ion-ion separation is around 4.23 Å, which is significantly greater than that in $Ti_2CO_2$/B-Gr heterostructures (2.99 Å at $\alpha = 0.11\text{Å}^{-2}$). Consequently, the resistance against the migration of ions due to neighboring ions is approximately equal for Na at high and low concentrations as can be seen in Fig. 5.10(c). Nevertheless, the resistance is significant at high concentrations for Mg due to greater ionic repulsion. Furthermore, Figure 5.11 shows examples of ion diffusion paths in MXene-based system and B-Gr bilayer. The initial paths for CI-NEB calculations are always straight between initial (I) and final (F) sites. In Mxene/B-Gr system, moving ion deviates from the straight path and move through the centers of the triangles (formed by the surface oxygen

atoms) as seen in Fig 5.11(b). But, Figure 5.11(d) depicts that the Mg/Na are able to diffuse on a nearly straight path within the B-Gr/B-Gr bilayer due to the presence of a weak interaction with the B-Gr sheets.

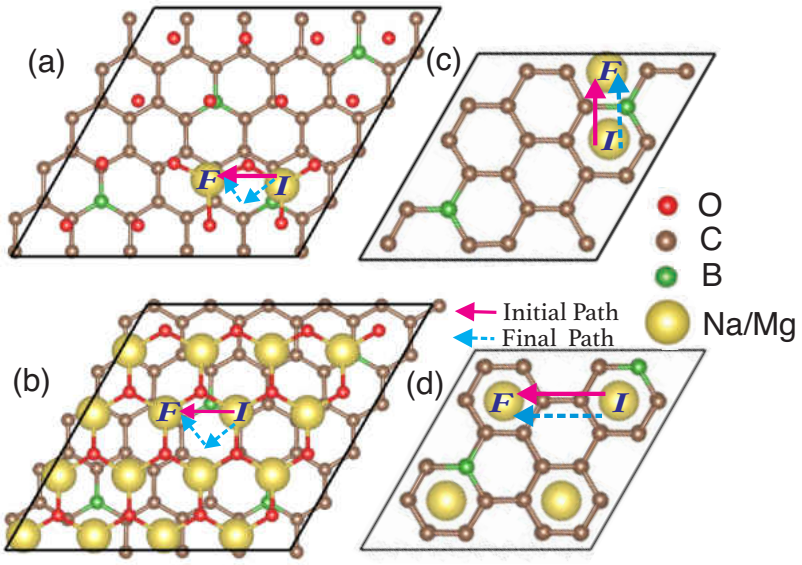


Figure 5.11: Calculated diffusion paths for $Ti_2CO_2$/B-Gr system with (a) 0.01Å$^{-2}$ and (b) 0.11Å$^{-2}$ ionic concentrations and B-Gr/B-Gr system with (c) 0.02Å$^{-2}$ (d) 0.04Å$^{-2}$ ionic concentrations. Only the bottom O layer and B-Gr layer are shown in $Ti_2CO_2$/B-Gr case. Initial and final sites are marked as "I" and "F", respectively.

The Li intercalated graphite electrodes have a diffusion barrier around 0.5 eV.[172] $MoS_2$/ undoped-Gr systems show diffusion barriers around 0.5-0.6 eV for the Li diffusion between the layers.[173] $Ti_2CO_2$/undoped-Gr heterostructures provide around 0.3 eV diffusion barrier for Li, while that from $V_2CO_2$/undoped-Gr is 0.6 eV.[151] Both $Ti_2CO_2$/undoped-Gr and $V_2CO_2$/undoped-Gr heterostructures have similar diffusion barriers for other alkali metal ions, i.e. 0.4 eV for Na, 0.3 eV for K and 0.6 eV for Ca.[164] Mg exhibits sluggish diffusion due to high polarization as compared to Li and Na.[174,175]

## 5.4 Conclusions

In this work, we conducted a density functional theory study on $Ti_2CO_2$/B-Gr heterostructure and B-Gr bilayer in order to examine the suitability of Na and Mg intercalation. Here, we exploited boron doping in order to chemically modify the graphene sheet in such a way that B-doping results in an electron-deficient system that strongly attracts positively charged Na/Mg ions as compared to pristine graphene. As a result, B-Gr bilayer is capable of storing Na/Mg with considerably high binding energies, even though Na/Mg intercalated bare graphene bilayers are not promising. The Na intercalated heterostructure shows more distortions due to the larger ionic radius of Na compared to Mg. The Na intercalated systems present considerable interlayer separation change due to larger size of Na. Instead, intercalation of small radius Mg ions provide relatively small interlayer separation change ($\leq$ 0.5 Å) for both heterostructure and bilayer, implying that the Mg intercalated systems may retain good mechanical stability during the charging/discharging process. The average voltage values calculated for Na intercalated systems are greater than that of highly doped B-Gr monolayer and multilayers. Furthermore, it could be shown that the gravimetric capacity of Mg intercalated $Ti_2CO_2$/B-Gr system is higher than that of Mg intercalated 3D-$Ti_3C_2T_x$. Our calculations revealed that the diffusion barriers are concentration-dependent. The low diffusion barriers obtained for the Na intercalated systems reflects that high charging/discharging rates can be expected. As a result of bivalency of Mg, it provides higher storage capacities than that of Na in the respective systems, while having low charging/discharging rates.

# CHAPTER VI

# SULFUR-FUNCTIONALIZED MXenes FOR Li-ION BATTERY APPLICATIONS

## 6.1 Introduction

Recently, sulfur functionalized MXenes have emerged as promising candidates as electrode materials because of their lower energy barriers, which offer higher charging/discharging rates and larger power densities.[176] The lightest MXene $Ti_2C$ with S termination has been studied for Li, Na, K, Mg, and Ca intercalation, where energy barriers are less than 0.5 eV. Mg intercalated $Ti_2CS_2$ provides excellent gravimetric capacity (1871.13 $mAhg^{-1}$),[177] which is much greater than that from bare $Ti_2C$ ($\approx$ 700 $mAhg^{-1}$) and $Ti_2CO_2$ (570 $mAhg^{-1}$) monolayers.[178] It has been reported that Na adsorbed $Ti_3C_2S_2$ nanosheets pose lower energy barrier (0.11 eV) than $Ti_3C_2O_2$ (0.22 eV).[179] S-functionalized $V_2C$ also provides lower energy barriers for Li and Na as compared to O-functionalized $V_2C$.[176] $Fe_2CS_2$ MXene has been discovered as a suitable electrode material for Al-ion batteries. $Fe_2CS_2$ can provide a capacity of 642 $mAhg^{-1}$, which is more than twice the capacity from $Fe_2CO_2$ (288 $mAhg^{-1}$).[180]

Considering the potential of these materials as electrode materials in battery applications, we carried out density functional theory (DFT) based calculations for $M_2CS_2$ MXenes, where M = Sc, Ti, Zr, Hf, V, Nb, Ta, Cr, Mo, and W. Our phonon calculations reveal that all the above MXenes, except Sc-based one, are dynamically stable. Cluster expansion calculations have been performed to obtain the lowest en-

ergy Li configurations at different concentrations. For a given Li concentration, Ti, Zr, and Hf based $M_2CS_2$ monolayers show lower binding energies (or stronger interaction) as compared to other S-functionalized MXenes. $M_2CS_2$ MXenes, where M= Ti, Hf, Zr, V, and Nb, are capable of attracting at least a full layer of Li on both surfaces whereas other MXenes provide a positive voltage only at much lower Li concentrations. Importantly, Ti, V, and Nb based MXenes are capable of storing three layers of Li, which greatly enhances the storage capacity. Ti- and V-based $M_2CS_2$ MXenes provide relatively higher capacities, which are greater than 400 mAh/g, than that of other considered S-functionalized MXenes of this work and their O-terminated counterparts. Diffusion barriers for all the dynamically stable $M_2CS_2$ nanosheets are smaller than 0.22 eV, offering charging/discharging rates in battery applications.

## 6.2 Computational Methods

The density functional theory (DFT) calculations were performed using the Vienna *ab initio* simulation package (VASP).[74–77] A plane-wave energy cutoff was set to 500 eV. The electron-ion interactions were described by the projected augmented wave (PAW) method.[81,82] The generalized gradient approximation (GGA) based exchange-correlation potential was considered with the Perdew-Burke-Ernzerhof (PBE) pseudopotentials.[100,101] A vacuum space larger than 15 Å was used to avoid spurious interaction between monolayers. The Γ-centered $17 \times 17 \times 1$ Monkhorst-Pack $k$-meshes were considered. The climbing image nudged elastic band (CI-NEB) method, as implemented in the VASP transition state tools, was applied to estimate the minimum energy diffusion paths.[83,160]

## 6.3 Results

### 6.3.1 Stability of MXenes

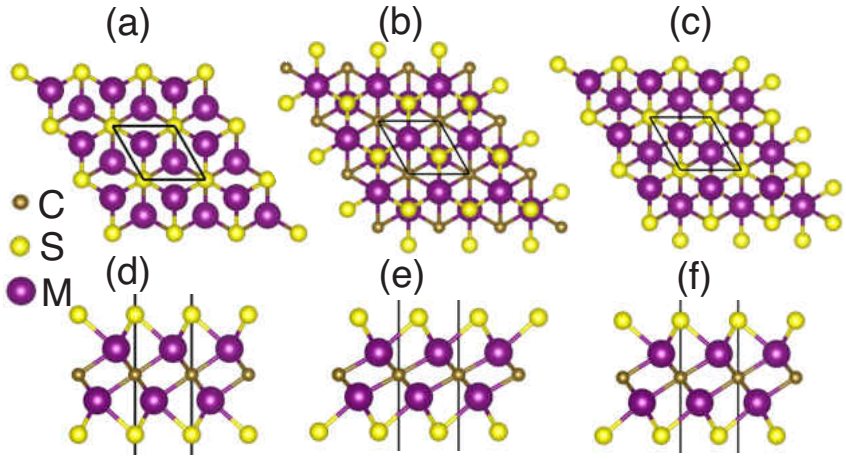


Figure 6.1: Top views of $M_2CS_2$ monolayers with (a) HCP, (b) FCC and (c)FCC-HCP surface structures, and the side views of (d) HCP, (e) FCC and (f) FCC-HCP surface structures

First, we considered different possible surface structures for $M_2CS_2$ (M= Sc, Ti, Zr, Hf, V, Nb, Ta, Cr, Mo, W) monolayers. The ground-state structure of bare-$M_2C$ monolayers is hexagonal, where the C layer is sandwiched between the two M layers. By changing the position of the S atoms on the surface, we predicted three different surface structures for sulfur atom, namely HCP, FCC, and HCP-FCC, as shown in Fig. 6.1. The HCP structure has the $P\bar{3}m1$ space group symmetry with both top and bottom S atoms residing directly above and below the same C atom. The FCC surface structure also possesses the $P\bar{3}m1$ symmetry. In the FCC structure, the top S atom is positioned directly above the bottom M atom, whereas the bottom S atom is at the right below the top M atom. The HCP-FCC structure has a mixed surface termination with the coexistence of HCP and FCC crystal configurations (see Fig. 6.1(c) and (f)).

The ground state structures of the materials are given in TABLE 6.1. $M_2CS_2$ with a 4B M element (Ti, Zr, and Hf) has the FCC structure as the minimum energy

configuration, while that with a 6B M element has the HCP surface termination. Even though MXenes with Nb and Ta provide the lowest energy surface termination for FCC-HCP structures, the S atoms prefer to sit at the FCC sites in V related MXene. Our phonon calculations (Fig. 6.2) indicate that all those monolayers with the 4B, 5B, and 6B M atoms are dynamically stable. Even though $Sc_2CO_2$ is stable, our phonon calculations found that $Sc_2CS_2$ is dynamically unstable.

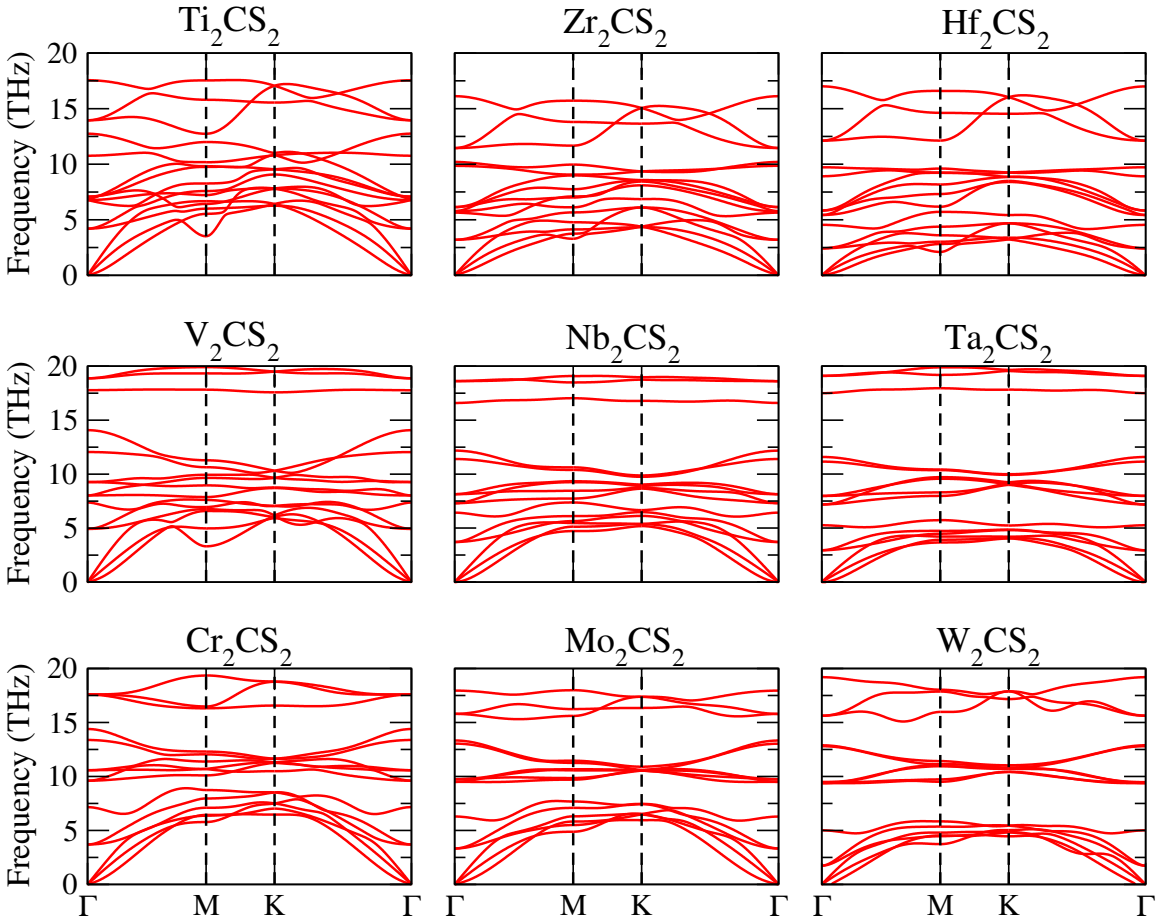


Figure 6.2: Phonon dispersion curves for stable S-functionalized MXenes

The computed lattice constants ($a$) and the M-S, M-C, and C-S bond lengths are summarized in TABLE 6.1. Our calculations are in good agreement with the values reported by previous research for $Ti_2CS_2$, $V_2CS_2$ and $Mo_2CS_2$.[176,177,181,182] The calculated lattice constants show that those values are larger than that of their O terminated counterparts ($M_2CO_2$). For instance, Ti, Zr, Hf, V, and Mo based

$M_2CO_2$ have $a$ values of 3.031, 3.309, 3.268,[183] 2.86,[184] and 2.99[185] Å, respectively . These values are more than 0.1 Å smaller than that of Ti, Zr, Hf, and V based S-terminated MXenes. We also found that $M_2CS_2$ MXenes have significantly longer M-S bond lengths than the M-O bond lengths of $M_2CO_2$ because the high electronegative O (3.5) which makes stronger and shorter bonds with M atoms compared to S, whose electronegativity is only 2.5. In addition, the S atom has a much larger radius than the O atom, which leads to a longer M-S bond as compared to the M-O bond. Such a large electronegativity difference between O and S also implies a larger charge on O, thereby larger O-Li attractive Coulomb interaction. $M_2CS_2$ with $3d$ transition metal atoms have the shortest bond lengths and lattice constants, as can be seen in TABLE 6.1. M-C and M-S bond lengths with $3d$ M atoms are shorter than that of $4d$ and $5d$ M atoms. These bond lengths in MXenes with $4d$ and $5d$ M atoms of the same column have approximately the same magnitude. This trend is correlated with the ionic radius ($R$) of the respective elements. For instance, $R_{\mathrm{Ti}} = 60$ pm ¡ $R_{\mathrm{Zr}} = R_{\mathrm{Hf}} \approx$ 86 pm by assuming these three atoms are at +4 oxidation state.[186]

The Bader charge ($\Delta q$) on each atom are presented in TABLE 6.1. The Bader charge on the S atoms is at most 1e, which is significantly smaller than the Bader charge on O in O-based MXenes. The M and C atoms have opposite charge transfer with the approximately same magnitude. Thus, we can conclude that M-C bonds also have an ionic character. The amount of charge transfer increases when moving down in the periodic table as the electronegativity difference between M and C/S atoms rises. MXenes with $3d$ transition metals show lower $\Delta q_{\mathrm{C}}$, $\Delta q_{\mathrm{M}}$ and $\Delta q_{\mathrm{S}}$ values than MXenes with $4d$ and $5d$ M atoms, indicating a weaker ionic bonding character in the former.

Table 6.1: The ground state structures, lattice constants ($a$), M-S and M-C bond lengths, average Bader charge transfer ($\Delta q$) for each element in $M_2CS_2$. The data for $Sc_2CS_2$ material is not provided, since it is dynamically unstable. For Nb and Ta, two different C-S bonds exist due to their mixed HCP-FCC surface structures.

| M | Ground State | $a$ (Å) | M-S (Å) | M-C (Å) | C-S (Å) | $\Delta q_C$ (e) | $\Delta q_M$ (e) | $\Delta q_S$ (e) |
|---|---|---|---|---|---|---|---|---|
| Ti | FCC | 3.197 | 2.406 | 2.211 | 3.321 | -1.843 | 1.739 | -0.814 |
| Zr | FCC | 3.477 | 2.539 | 2.414 | 3.525 | -1.925 | 1.915 | -0.949 |
| Hf | FCC | 3.435 | 2.516 | 2.383 | 3.488 | -2.160 | 2.125 | -1.042 |
| V | FCC | 3.063 | 2.370 | 2.078 | 3.203 | -1.703 | 1.504 | -0.649 |
| Nb | HCP-FCC | 3.281 | 2.508 | 2.267 | 2.888 (3.393) | -1.823 | 1.672 | -0.757 |
| Ta | HCP-FCC | 3.267 | 2.494 | 2.267 | 2.887 (3.357) | -2.061 | 1.914 | -0.949 |
| Cr | HCP | 2.934 | 2.278 | 2.053 | 2.686 | -1.353 | 1.188 | -0.509 |
| Mo | HCP | 3.077 | 2.400 | 2.201 | 2.914 | -1.410 | 1.280 | -0.573 |
| W | HCP | 3.068 | 2.404 | 2.220 | 2.963 | -1.574 | 1.438 | -0.648 |

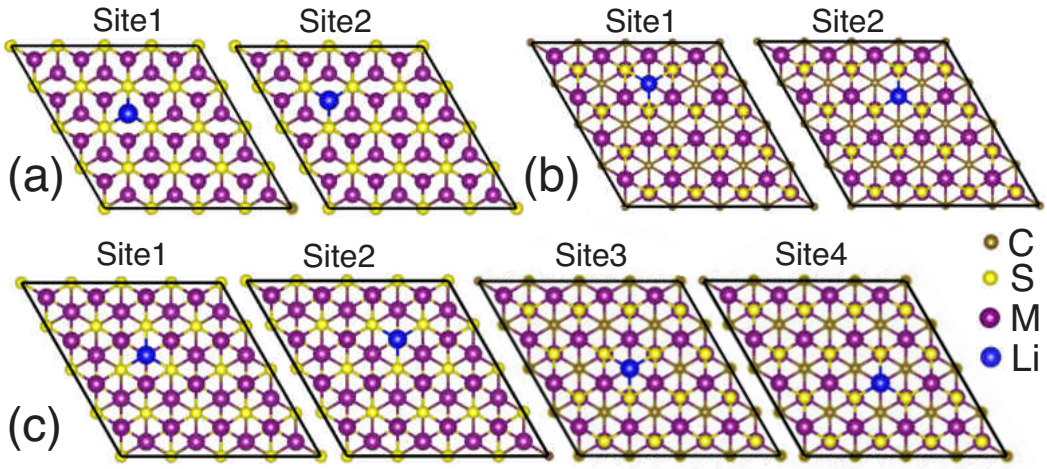


Figure 6.3: The possible Li adsorption sites for (a) HCC, (b) FCC and (c) HCP-FCC surface structures of $M_2CS_2$ MXenes.

### 6.3.2 Single Ion Adsorption

Next, we investigated single Li adsorption on S-terminated MXenes using a $4 \times 4$ $M_2CS_2$ supercell. We identified the different adsorption sites for the different lattice structures, as shown in Fig. 6.3. Figure 6.3(a) shows the two possible sites on the HCP structure. While Li is directly above a bottom M atom in Site1, it resides above a M atom in Site2. Figure 6.3(b) denotes the possible adsorption sites on the FCC surface structure. Site1 indicates a site on the surface right above a C atom, while Site2 is directly above a M atom. Due to the reduced symmetry, we found four distinct adsorption sites for the mixed HCP-FCC surface structure (Fig. 6.3(c)).

Table 6.2: The binding energy of a single Li ($E_b$) at different sites and Bader charge transfer ($\Delta q$) for each element when a single Li is adsorbed at the minimum energy site.

| M | Ground State | $E_b$ (eV/atom) | | | | $\Delta q_C$ (e) | $\Delta q_M$ (e) | $\Delta q_S$ (e) | $\Delta q_{Li}$ (e) | Li-S (Å) |
|---|---|---|---|---|---|---|---|---|---|---|
| | | Site1 | Site2 | Site3 | Site4 | | | | | |
| Ti | FCC | -2.226 | -2.262 | - | - | -1.852 | 1.736 | -0.838 | 0.990 | 2.368 |
| Zr | FCC | -2.462 | -2.380 | - | - | -1.933 | 1.924 | -0.985 | 0.996 | 2.352 |
| Hf | FCC | -2.300 | -2.241 | - | - | -2.154 | 2.127 | -1.078 | 0.995 | 2.349 |
| V | FCC | -1.348 | -1.467 | - | - | -1.719 | 1.510 | -0.678 | 0.991 | 2.351 |
| Nb | HCP-FCC | -1.549 | -1.645 | -1.248 | -1.324 | -1.822 | 1.682 | -0.798 | 0.993 | 2.380 |
| Ta | HCP-FCC | -1.201 | -1.310 | -0.920 | -1.004 | -2.055 | 1.885 | -0.885 | 0.991 | 2.376 |
| Cr | HCP | -1.428 | -1.556 | - | - | -1.357 | 1.203 | -0.553 | 0.991 | 2.367 |
| Mo | HCP | -1.066 | -1.209 | - | - | -1.401 | 1.280 | -0.607 | 0.991 | 2.358 |
| W | HCP | -0.955 | -1.113 | - | - | -1.587 | 1.451 | -0.686 | 0.991 | 2.352 |

Here, Site1 and Site2 are identified on the surface with HCP termination, whereas Site3 and Site4 are on FCC terminated surface. Site1 and Site2 are equivalent to Site1 and Site2 of the HCP surface structure, and the Site3 and Site4 are identical to the Site1 and Site2 of FCC surface structure.

The binding energy ($E_b$) per Li-ion was calculated as follows

$$E_b = \frac{1}{n}[E(M_2CS_2 + nLi) - E(M_2CS_2) - nE(Li)] \tag{6.1}$$

where $E(M_2CS_2 + xLi)$ is the total energy of MXene with Li, $E(M_2CS_2)$ is the total energy of bare MXene, $E(Li)$ is the energy of the Li atom obtained from body-centered-cubic (BCC) bulk crystal structure, and $n$ is the number of adsorbed Li atoms in our computational unit cell. The calculated $E_b$ values are given in TABLE 6.2. It is clear that the Li ions adsorbed on MXenes with group 4B M atom have the lowest $E_b$ energy which increases when M changes from group 4B to 6B. The above observation indicates that the strongest Li-S bonding exists in the MXenes made of group 4B transition metal atoms. $Zr_2CS_2$ shows the lowest $E_b$ that is -2.462 eV, while the highest $E_b$ is calculated for $W_2CS_2$.

Regarding the adsorption site, the Li atom prefers to bind to the Site2 on $M_2CS_2$, where M= Ti, V, Nb, Ta, Cr, Mo and W. However, the Site1 is energetically more favorable for $Zr_2CS_2$ and $Hf_2CS_2$. One reason for this different behavior of $Zr_2CS_2$

and $Hf_2CS_2$ monolayers is attributed to their much larger lattice constants.

The Bader charge transfer calculations in TABLE 6.2 show that $\Delta q_{\mathrm{Li}}$ ($\sim$ 1e) is almost the same for all $M_2CS_2$ MXenes. The charge on the S atoms plays a crucial role in determining the binding energy of Li. For instance, for $W_2CS_2$, the Bader charge on S atoms is only 0.648e, which is significantly smaller than that on S atoms of $M_2CS_2$ with M=Ti, Zr and Hf. Therefore, the Li-S attractive interaction is stronger in the latter system. The larger the charge on S, the stronger the interaction with Li.

### 6.3.3 Multiple Ion Adsorption

Before calculating the voltage, we searched out the most stable Li configurations for different intermediate Li concentrations on S-functionalized MXenes using cluster-expansion (CE). In most of the previously published computational battery papers, the possible adsorption configurations for ions have been found by checking a few numbers of possible adsorption structures for each concentration. This can cause substantial errors in the calculation of voltage at intermediate Li concentrations and the prediction of storage capacity. For instance, in recent work on Li adsorption on $Mo_2CS_2$ monolayer, the calculated theoretical specific capacity was found to be 410 mAh/g.[182] However, our capacity calculations based on CE predicts a much lower capacity of 49.4 mAh/g. Therefore, to predict the storage capacity and voltage correctly, the CE method was chosen in our work. In the CE method, for a given configuration, the formation energy ($E_f$) of $Li_xM_2CS_2$ with respect to $M_2CS_2$ and $Li_2M_2CS_2$ is defined as

$$E_f = E_{tot}[\mathrm{Li}_{2-2x}\mathrm{M}_2\mathrm{CS}_2] - E_{tot}[\mathrm{M}_2\mathrm{CS}_2] - (1-x)E_{tot}[\mathrm{Li}_2\mathrm{M}_2\mathrm{CS}_2] \qquad (6.2)$$

Here, $x$ is the fraction of Li atoms out of the total number of Li atoms in a fully loaded MXene. In other words, $x$=1 denotes the adsorption of two layers of Li (one

Li layer on each surface). $E_{tot}[Li_xM_2CS_2]$, $E_{tot}[Li_2M_2CS_2]$, and $E_{tot}[M_2CS_2]$ are the calculated formula unit energies of $Li_xM_2CS_2$ $Li_2M_2CS_2$, and $M_2CS_2$ monolayers, respectively. We computed the total energy of at least 150 configurations with different Li concentrations for each M (i.e., transition metal atom). Then, we constructed the CE Hamiltonian of $Li_xM_2CS_2$ by fitting to the first-principles energies. The formation energies allow us to construct the ground state energy vs. composition curve (called convex hull), which consists of lines connecting all the lowest energy structures that are most likely to form in experiments. Convex hull identifies thermodynamically stable structures at T = 0 K, which can be considered as free energy without the inclusion of the entropy term. The cross-validation score, providing the predictive power of the cluster expansion, of the CE fitting for different MXenes are less than 10 meV, which depicts that our CE Hamiltonian is accurate enough to predict the formation energies of $Li_xM_2CS_2$ as a function of Li concentration. Figure 6.4 denotes the calculated formation energies as a function of Li concentration obtained from the cluster expansion calculations using the ATAT code.[187–189] We found several stable Li configurations at intermediate concentrations. The shape of the convex hull is similar for the transition metal elements in the same column of the periodic table. MXenes with group 4B and 5B elements have a minimum in the convex hull at a lower concentration than the group 6B elements, allowing more structures to exist on the convex hull. Cr-based MXene has no structure on the convex hull when the Li concentration is larger than $x$ =0.34 due to its small lattice constant, resulting in enhanced repulsive interaction between Li ions with increasing Li concentration, and thereby pushing the structures away from the convex hull. MXenes with group 4B elements have lower minimum formation energies than that with group 5B and 6B elements. Figure 6.5 shows the structure of minimum energy intermediate configurations extracted from the convex hull plots. In the present study, we neglected the temperature effects. Some of the ion orderings that are within a small energy

window above the convex hull may become accessible at finite temperatures. By considering the typical operation temperatures of batteries, we can predict the accessible structures from the convex hull plots. For instance, MXenes with group 4B and 5B elements have configurations very close to the convex hull, which can be accessible with increasing temperature.

We also calculated the Li adsorption on $Li_2M_2CS_2$, where $M_2CS_2$ already has two layers of Li adsorbed (one Li layer on each surface). Figure 6.6 shows the formation energy for $Li_{2+x}M_2CS_2$, where M=Ti, V and Nb. Further addition of Li ions to $Li_2M_2CS_2$ makes the formation energy positive, meaning that further Li adsorption is not energetically possible at T= 0K. At $x = 0.5$ (or one more Li layer), the formation energy is slightly positive. At finite temperatures, the structures with slightly positive energies may be accessible as entropy term lowers the formation energy. Therefore, it is possible to store three layers of Li on these three MXenes.

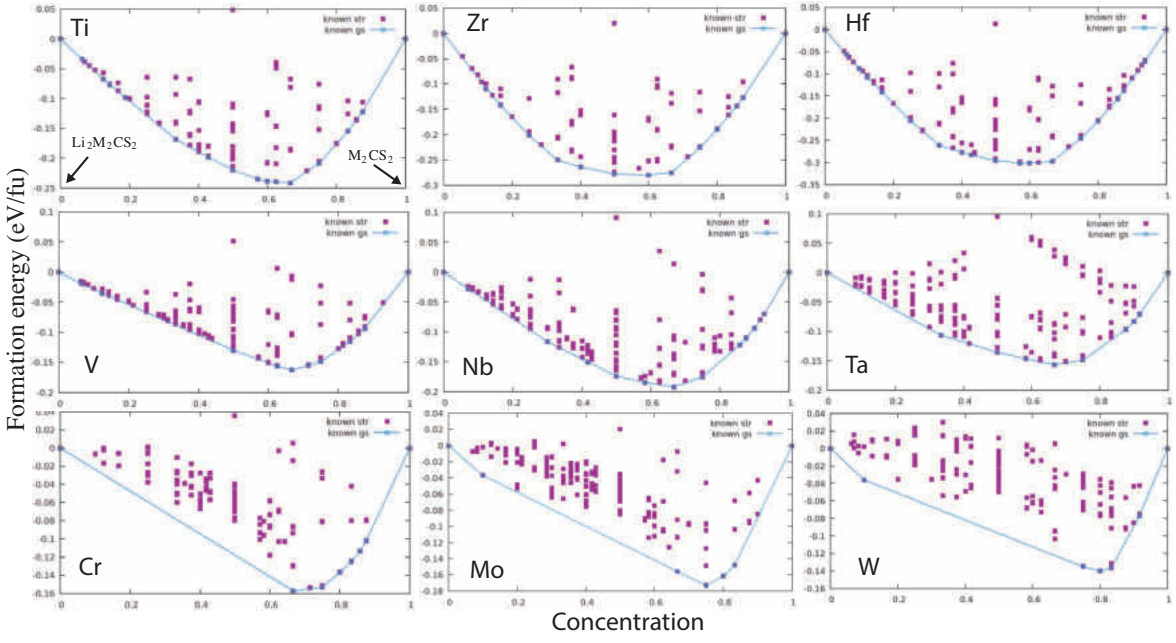


Figure 6.4: Calculated formation energies of $Li_xM_2CS_2$. The blue line in each figure indicates the convex hull. The configurations marked with blue empty squares are those that are the thermodynamically stable (at T = 0 K) ordered configurations of lithium ions and vacancies on S-functionalized MXenes. .

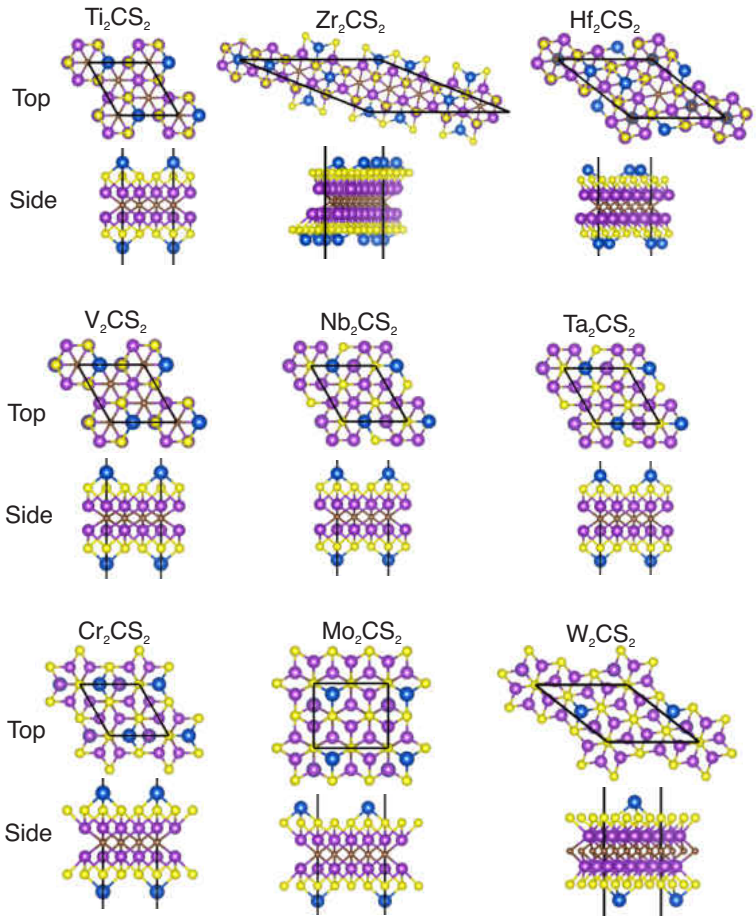


Figure 6.5: Top and side views of lowest energy multiple ions adsorbed $M_2CS_2$ MXenes structures obtained from the minimum of convex hull.

We studied the change in lattice constant ($\Delta a$) when both surfaces are covered with Li atoms, based on the expression $\Delta a = \frac{(a-a_0)\times 100}{a_0}$ as shown in TABLE 6.3. Here, $a_0$ is the lattice constant of bare MXene, while $a$ is the lattice constant of $M_2CS_2Li_2$. All materials show surface expansion when Li atoms are attached to the surfaces. 3*d*-transition metal atom-based $M_2CS_2$ exhibit high in-plane lattice parameter expansion in line with strong interactions with Li observed for these monolayers. $V_2CS_2Li_2$ possesses the highest increase which is around 5.8%. 5*d*-transition metal-based $M_2CS_2$ MXenes show the lowest change, which is only 1.4%.

Figure 6.7 denotes the $E_b$ as a function of Li content. Here, the Li content is 2 when all lowest energy adsorption sites on both surfaces are occupied. The common

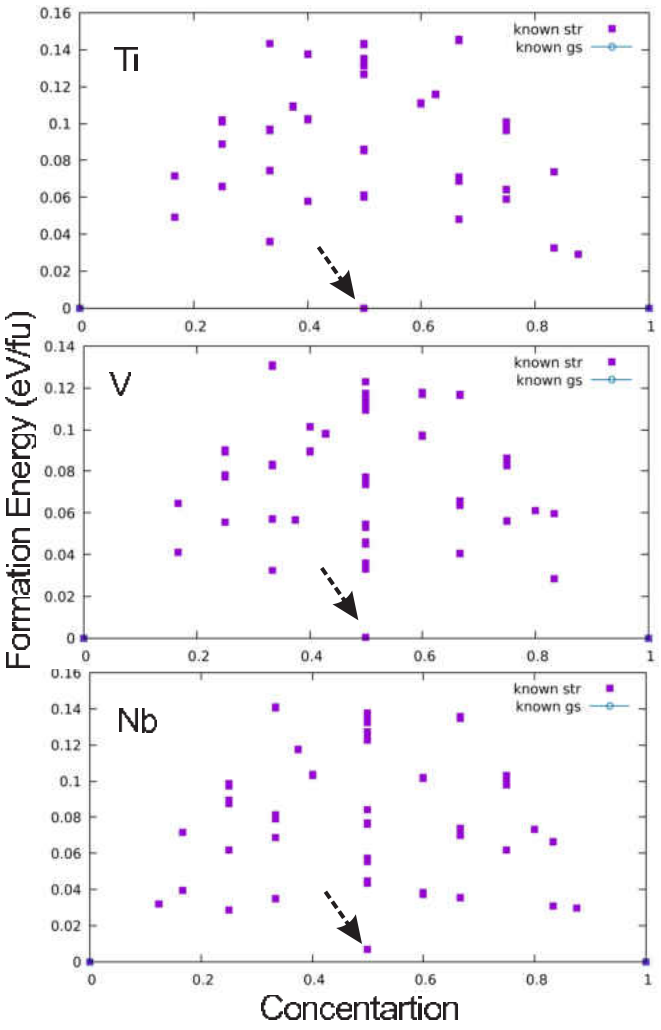


Figure 6.6: Calculated formation energies of $Li_{2+x}M_2CS_2$ as a function of Li concentration. Arrows show the minimum energy structures at $x$=0.5.

feature of the results for all MXenes is that the binding energy rises (approaching the positive side) while the Li content increases. It is clear that $E_b$ of $M_2CS_2$ MXenes with M elements in the same column of the periodic table exhibit similar behavior with changing Li content. For a given content, the lowest (more negative) $E_b$ can be found for the 4B column, while the highest values can be obtained for the 6B column. Thus, Li adsorption on $Ti_2CS_2$, $Zr_2CS_2$, and $Hf_2CS_2$ are more stable, and it will be useful for avoiding the formation of bulk Li (or Li clusters) during the charging/discharging processes. $W_2CS_2$ has positive $E_b$ after a 1.5 Li content, implying that the adsorption of two layers of Li (one Li layer on each surface) is not energetically favorable.

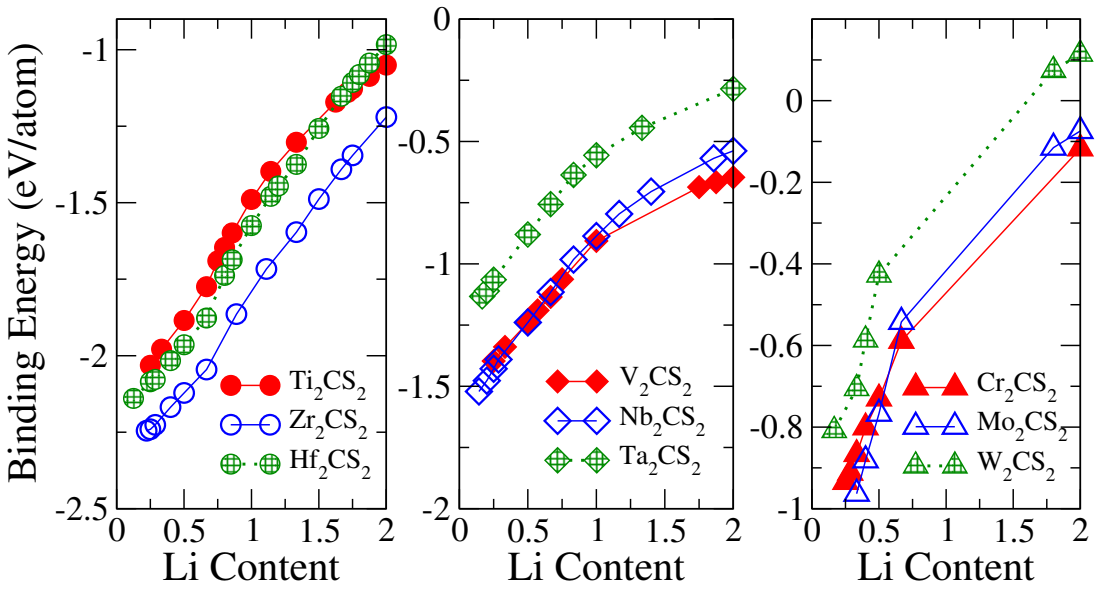


Figure 6.7: Binding energy ($E_b$) as a function of Li content.

### 6.3.4 Electrochemical Properties

We next studied the electrochemical properties of the S-fuctionalized MXenes. The chemical reaction for adsorbing Li on $M_2CS_2Li_{x1}$ and forming $M_2CS_2Li_{x2}$ can simply be described using Eq. 6.3, where $x_1$ and $x_2$ are the Li content before and after the reaction.

$$(x_2\text{-}x_1)Li^+ + (x_2\text{-}x_1)e^- + M_2CS_2Li_{x1} \longleftrightarrow M_2CS_2Li_{x2} \tag{6.3}$$

The open-circuit voltage (OCV) for the above chemical reaction can be predicted using the Gibbs free energy ($G(x)$), which can be written as $G(x) = \Delta E + P\Delta V - T\Delta S$. Here, $\Delta E$ is internal energy change (obtained from our DFT calculations at T= 0K), $P$ indicates pressure, $\Delta V$ is volume change, $T$ is temperature, and $\Delta S$ is entropy change. However, $P\Delta V \approx 10^{-5}$ eV and $T\Delta S \approx 25$ meV. By neglecting these two terms, we are able to approximate the average voltage ($V$) by only determining $\Delta E$ as follows.

Table 6.3: The in-plane lattice constant change ($\Delta a$), maximum voltage ($V_{max}$), average voltage ($V_{avg}$), gravimetric capacity ($C_g$) and diffusion barrier ($E_{diff}$). Here, $V_{avg1}$ was calculated using Eq. 6.4 for positive voltage ranges, while $V_{avg2}$ was computed employing $\sum_i^N V_i/N$ where $i$ is the step number and $N$ is the number of steps in Fig. 6.8.

| M | $\Delta a$(%) | $V_{max}$ (V) | $V_{avg1}$ (V) | $V_{avg2}$ (V) | $C_g$ (mAh/g) | $E_{diff}$ (eV) |
|---|---|---|---|---|---|---|
| Ti | 3.6 | 2.031 | 1.050 | 0.997 | 288.6 | 0.176 |
| Zr | 2.1 | 2.245 | 1.220 | 1.362 | 196.8 | 0.218 |
| Hf | 1.7 | 2.140 | 0.983 | 0.988 | 120.0 | 0.206 |
| V | 5.8 | 1.397 | 0.646 | 0.730 | 279.4 | 0.199 |
| Nb | 1.9 | 1.521 | 0.538 | 0.724 | 194.4 | 0.211 |
| Ta | 1.5 | 1.133 | 0.444 | 0.564 | 79.9 | 0.210 |
| Cr | 3.7 | 0.935 | 0.589 | 0.561 | 96.8 | 0.177 |
| Mo | 2.0 | 0.963 | 0.767 | 0.582 | 49.4 | 0.210 |
| W | 1.4 | 0.808 | 0.705 | 0.705 | 20.0 | 0.217 |

$$V \approx \frac{E[M_2CS_2Li_{x1}] - E[M_2CS_2Li_{x2}] + (x_2 - x_1)E[Li]}{(x_2 - x_1)} \tag{6.4}$$

Using Eq. 5.5, we calculated the open-circuit voltage as a function of Li concentration, as shown in Fig. 5.9. When calculating the voltages, we considered the structures on the convex hull (Fig. 6.4). Usually, the V and Mo containing MXenes with O or mixed O/OH terminations have higher OCV and can be cycled to higher potentials vs. $Li/Li^+$ compared to Ti containing MXenes. However, here, we found that the highest maximum voltages were obtained for sulfur functionalized MXenes with M atom from group 4B of the periodic table (i.e., Ti, Zr, and Hf). The explanation for the discrepancy in our calculations and the previous experimental/theoretical results is that sulfur functionalized MXenes with Ti, Zr, and Hf exhibit the strongest binding energies for Li as a result of larger negative charge on S atoms, giving rise to strong attractive interaction with positively charged Li-ions. For instance, the Bader charge on the S atom is more than 0.84 for Ti, Zr, and Hf, whereas it is less than 0.7 for both V and Mo. The charge on Li-ion is almost the same for all consider systems. Since the value of voltage is substantially dependent on the strength of binding between

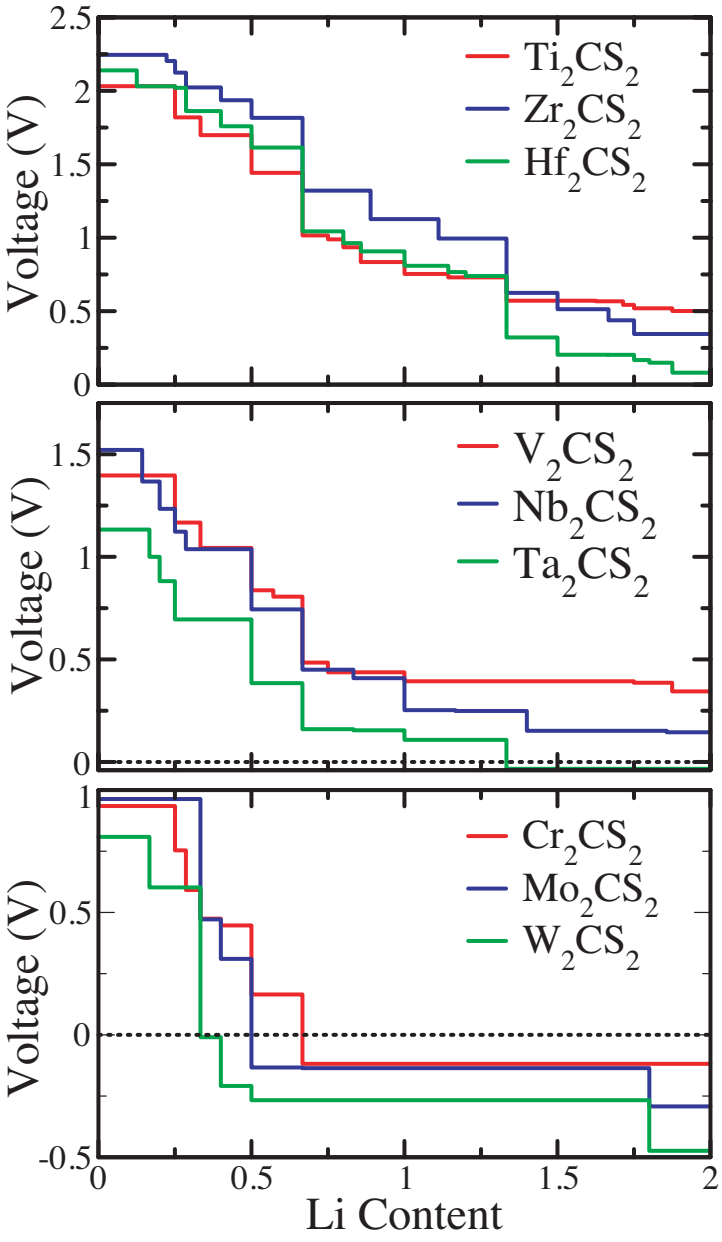


Figure 6.8: Binding energy (Voltage as a function of Li Content.

the host material and Li-ion, the highest maximum voltages were obtained for Ti, Zr, and Hf containing sulfur functionalized MXenes. The maximum voltages for Ti, Zr, and Hf are larger than 2 V. $M_2CS_2$ with M element from group 5B provides the next highest maximum voltages, which are greater than 1 V. The lowest voltage for a given Li content is obtained from $M_2CS_2$ monolayers with M atoms from group 6B, where voltages are always less than 1 V. It is clear from Fig. 5.9 that voltages computed for $M_2CS_2$ with Ti, Zr, Hf, V, and Nb do cross zero even when the Li content is approaching 2. However, the voltage of $Ta_2CS_2$ becomes negative at around 1.33 Li content, which indicates that two layers of Li cannot be stored using $Ta_2CS_2$ monolayer. The computed voltage for $Cr_2CS_2$, $Mo_2CS_2$ and $W_2CS_2$ become negative for low Li contents, designating that very low capacities can be expected from these MXenes. TABLE 6.3 summarizes the maximum voltage ($V_{max}$) and average voltage ($V_{avg}$) for each $M_2CS_2$ monolayer. The theoretically calculated $V_{max}$ for bare $Ti_2C$ is around 0.6 V and that for $Ti_2CO_2$ is 1.94 V.[190] $Ti_2CS_2$ provides approximately the same $V_{max}$ (2.03 eV) as it's O-functionalized counterpart. Bare $Mo_2C$ monolayers possesses $V_{max}$ of 0.95 V[191] which is almost equal to $V_{max}$ of $Mo_2CS_2$ .

The theoretical maximum gravimetric capacity ($C_g$) of $M_2CS_2$ MXenes can be obtain from

$$Cg = \frac{x_{\max} \times z \times F \times 10^3}{M_{\mathrm{M_2CS_2}} + x_{\max}\mathrm{Li}} \tag{6.5}$$

where $x_{max}$ is the maximum Li content before the voltage of the system become negative, $z$ is the valency of ion ($z = 1$ for Li), $F$ is the Faraday constant (26.81 Ah/mol), and $M_{\mathrm{M_2CS_2+x_{max}Li}}$ is the total atomic mass of the system with $x_{max}$ of Li. Note that we also included the mass of adsorbed Li atoms, which is usually neglected when calculating the capacity. This causes the overestimation of the storage capacity.

From TABLE 6.3, we notice that the highest $C_g$ (288.6 mAh/g) can be obtained for $Ti_2CS_2$ due to its low total atomic weight and the ability to adsorb full Li lay-

ers on both surfaces. Next lightest $M_2CS_2$ MXene is $V_2CS_2$ and it also possesses a high capacity (279.4 mAh/g). Even though $Cr_2CS_2$ is the third lightest MXene in TABLE 6.3, it exhibits very low capacity due to small $x_{\max}$. Despite the fact that two full layers of Li can be stored on Zr, Hf, and Nb based $M_2CS_2$, they provide low capacity compared to $Ti_2CS_2$ and $V_2CS_2$ due to their high total atomic masses. The theoretical $C_g$ of $Ti_2CO_2$ was reported as 350 mAh/g.[192] The theoretical values calculated for O-terminated $V_2C$ and $Nb_2C$ are 335 and 250 mAh/g, respectively. O-based MXenes possess higher theoretical values than S-based MXenes as a consequence of having a low atomic mass for O termination. The theoretical capacity calculated for bare $Ti_2C$ and $Ti_3C_2$ are 440 and 320 mAh/g, respectively. Even though these are much higher than that of it's S-functionalized $Ti_2C$, they have very low open-circuit voltages, which are 0.44 V for $Ti_2C$ and 0.62 V for $Ti_3C_2$.[192–194] The theoretically and experimentally obtained capacity for graphite is around 372 mAh/g, but its open-circuit voltage is very low (0.2 V).[194,195] $Ti_2NS_2$ and $V_2NS_2$ nitride MXenes have capacities around 300 mAh/g with average open-circuit voltages 0.64 V and 0.82 V, respectively.[196] Whereas $Ti_2CS_2$ provides a capacity close to 288 mAh/g with an average open-circuit voltage of 1.050 V.

In our previous analysis, we computed $C_g$ by considering two Li per formula unit or two Li layers (one layer on each surface of monolayer). However, our cluster expansion calculations revealed that $Ti_2CS_2$, $V_2CS_2$ and $Nb_2CS_2$ may store up to three Li per formula unit (or three layers of Li), giving rise a significant storage enhancement. Then, the storage capacities become 417.4 mAh/g for Ti, 404.5 mAh/g for V, and 284.4 mAh/g for Nb. Since we did not include entropy term, the voltage becomes negative ($\sim -0.1$ V) when increasing the number of adsorbed Li layers from two to three. Inclusion of this term may stabilize the multilayer adsorption on each surface of MXene monolayer. Therefore, our calculations propose that S-functionalized $Ti_2CS_2$, $V_2CS_2$ and $Nb_2CS_2$ are likely to have storage capacities larger than O-terminated

$Ti_2CO_2$, $V_2CO_2$ and $Nb_2CO_2$.

### 6.3.5 Diffusion Barrier

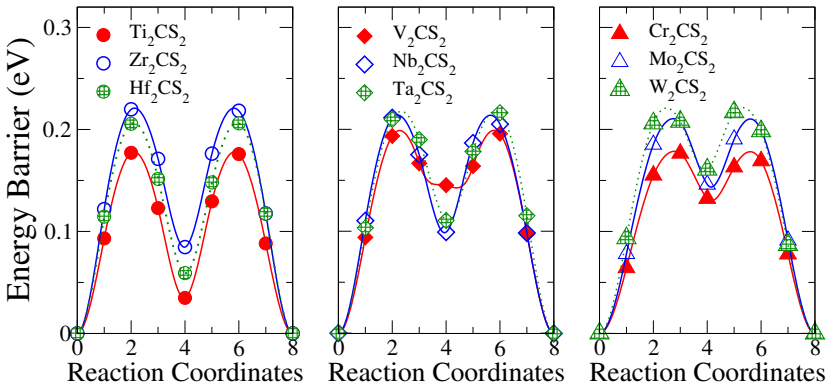


Figure 6.9: Diffusion barrier ($E_{\text{diff}}$) profiles for a single Li adsorbed on $M_2CS_2$.

A low diffusion barrier is an essential property of an electrode to achieve high kinetics of metal ions. The high mobility of Li ions leads to good charging and discharging rates and high power densities in batteries. In order to study the ion kinetics, we performed CI-NEB calculations for single ion adsorbed systems. The computed energy barriers as a function of reaction coordinates are shown in Fig. 6.9, and maximum energy barriers are mentioned in TABLE 6.3. The energy barrier is lower for 3*d*-transition metal-related $M_2CS_2$ MXenes than others. This can be due to the lower charge transfer of S atoms of Ti, V, and Cr atoms compared to the members of respective columns in the periodic table. Thus, Li-S attraction is low in respective MXenes. The lowest energy barrier was obtained for $Ti_2CS_2$, which is 0.176 eV. The next smallest energy barrier is for $V_2CS_2$, which is 0.199 eV. It is reported that single Li adsorbed on a $4 \times 4$ supercell of $V_2C$ provides very small diffusion barrier (0.02 eV) while that of $V_2CO_2$ posses 0.24 eV.[176] The higher barrier in O-based MXene is due to the larger interaction between Li and O than that between Li and S. These trends were also observed for Zr based MXenes where $Zr_2C$ has a negligible energy barrier, and $Zr_2CO_2$ has a barrier approximately 0.5 eV,[197] while $Zr_2CS_2$ has a barrier of only

0.218 eV. The calculated diffusion barriers of $M_2CS_2$ are much lower than that of commercial graphite (0.45-1.2 eV).[182,198]

Figure 6.10 denotes the diffusion barrier for a Li ion which is surrounded by other Li ions. As expected, the presence of adjacent Li ions strongly modifies the values and diffusion profiles due to the repulsive interaction among the positively charged Li ions. In these calculations, we only considered $Ti_2CS_2$, $V_2CS_2$ and $Nb_2CS_2$ due to their potential. We calculated the diffusion paths and energy barriers for a Li ion on a 4×4×1 supercell, where only a single adsorption site is empty to facilitate the migration of adjacent Li ions into this empty site. Our calculations found that energy barrier increases to 0.41, 0.48 and 0.43 eV for $Ti_2CS_2$, $V_2CS_2$ and $Nb_2CS_2$, respectively. Regardless of Li concentration, these MXenes are expected to offer faster kinetics for the battery operations as compared to commercial electrodes and computational predicted systems listed above.

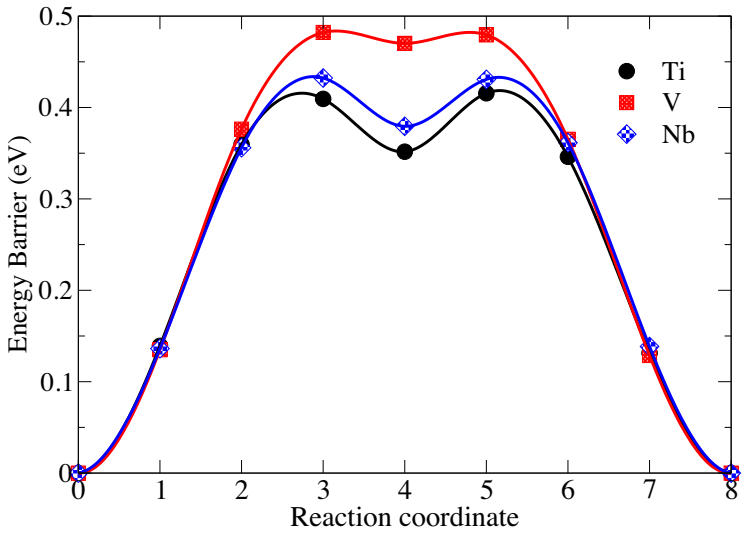


Figure 6.10: Diffusion barrier profiles for a single Li on $M_2CS_2$ for high Li concentration.

## 6.4 Conclusions

In summary, we conducted a density functional theory-based study of the structural, stability, electrochemical, and ion kinetics of sulfur functionalized $M_2CS_2$ MXenes, where M= Sc, Ti, Zr, Hf, V, Nb, Ta, Cr, Mo, and W. First, we identified the lowest energy S absorption site on bare $M_2C$ MXenes. Depending on the type of M element, the S atom prefers to site at different sites. From our phonon calculations at T = 0K, we confirmed that all $M_2CS_2$ MXenes, except $Sc_2CS_2$, are dynamically stable. $M_2CS_2$ with M = Ti, Zr, Hf, V, and Nb MXenes can attract full Li coverage on both surfaces. Our cluster expansion calculations revealed the correct Li adsorption structures at different concentrations. We found that $Ti_2CS_2$, $V_2CS_2$ and $Nb_2CS_2$ promise to have gravimetric capacities higher than their O-terminated counterparts. $Ti_2CS_2$ and $V_2CS_2$ have low diffusion barriers, which are around 0.19 eV. As a result, $Ti_2CS_2$ and $V_2CS_2$ have better ion-storage and fast ion diffusion properties. Due to the strong monolayer-$Li^+$ interaction, $M_2CS_2$ monolayers with Ti, Zr and Hf have larger open-circuit voltages where the maximum of the voltages exceed 2 V, and the average voltages are around 1 V. By considering all the above facts, not only $Ti_2CS_2$ but also $V_2CS_2$ and $Nb_2CS_2$ appears as candidate materials for the energy storage applications due to high voltages, large capacities, and low diffusion barriers.

# CHAPTER VII

# PILLARED STRUCTURES FOR Li-ION BATTERIES

## 7.1 Introduction

Evidently, the key limitations for batteries based on 2D materials are low storage capacities and slow ion mobilities. The latter results in slow charging/discharging rates. In this study, we proposed MXene multilayer structures, where individual layers are chemically connected via molecular linkers, known as pillared structures[199–204] in order to overcome these performances limiting factors. By building pillared structures from the chemically linked 2D sheets, it is possible to eliminate the disadvantages of multilayers. Pillaring can be used as an effective strategy to minimize the change in the interlayer distance in multilayers during ion loading/unloading. This enables zero volume change in electrode during battery cycling and improves mechanical and electrochemical stability of the system leading to extended cycle life. In addition, by selecting a stable linker molecule, it is possible to control the interlayer distance and the interaction strength between individual layers, opening a way to accommodate larger (such as $Na^{+}$) and more polarized (such as $Mg^{2+}$) ions and decrease energy barriers for the ion movement between layers. Since F and OH-functionalized MXenes are not as stable as O-functionalized ones,[205] and the F and OH groups result in lower capacities and very high Li diffusion barriers,[206] we selected O-terminated $Ti_3C_2$ (i.e. $Ti_3C_2O_2$ ) monolayer to test our proposal. In addition, functionalized

$Ti_3C_2$ is the best studied MXene and its electrical conductivity is quite high.[207] While many of the electrode materials in lithium-ion battery applications exhibit volume expansion upon ion intercalation, $Ti_3C_2$ paper electrodes was shown to undergo a volumetric contraction upon $Li^+$, $Na^+$, and $Mg^{2+}$ ions intercalation.[208] As a linker, we considered two different quinone molecules, namely 1,4-Benzoquinone ($C_6H_4O_2$) and Tetrafluoro-1,4-benzoquinone ($C_6F_4O_2$).[209] In order to investigate binding structures and energies, diffusion paths and barriers and maximum storage capacities, we performed first-principles simulations based on density functional theory.

## 7.2 Computational Methods

We performed first-principles calculations in the framework of density functional theory (DFT) as implemented in the Vienna ab-initio simulation package (VASP).[74,75] The generalized gradient approximation (GGA) within the Perdew- Burke-Ernzerhof (PBE)[100,101] formalism is employed for the exchange-correlation potential. The projector augmented wave (PAW) method[81,82] is used to take into account the electron-ion interaction. A plane-wave basis set with an energy cutoff of 400 eV is used in the calculations. For geometry optimization, the Brillouin-zone integration is performed within the Monkhorst-Pack scheme using regular $\Gamma$ centered $7\times7\times1$ and $3\times3\times1$ $k$-mesh for the $3\times3$ and $5\times5$ super cell structures, respectively.[210] The convergence criterion of the self-consistent field calculations is set to $10^{-5}$ eV for the total energy. To prevent spurious interaction between isolated monolayers, lattice vectors perpendicular to the 2D plane were fixed as 35 Å for all the simulations. By using the conjugate gradient method, atomic positions and lattice constants are optimized until the Hellmann-Feynman forces are less then 0.01 eV/Å and pressure on the supercell is decreased to values less than 1 kbar. We also took into account van der Waals (vdW) interactions using the DFT-D3 method, including Becke-Jonson damping.[106,107]

Diffusion barriers for Li atom is calculated using the climbing-image nudge elastic (CI-NEB) method as implemented in the VASP transition state tools.[83,160] CI-NEB is an efficient method in determining the minimum energy diffusion path between two given positions. We used a 5×5 super cell monolayer with 9 images, including initial and final positions, for CI-NEB calculations. The atomic positions and energy of the images were then relaxed. The amount of charge transfer between Li atom and pillared structure were determined by using the Bader charge analysis.[211–213]

Ab-initio molecular dynamics (MD) simulations[214,215] within isothermal-isobaric (NPT)[216] ensemble have been conducted by using VASP code. MD simulations are performed at the Γ-point, each simulation lasting 10 ps with a time step of 1 fs. Since heat will be released during the discharge of a battery, we considered MD simulations for both 300 K and 400 K. 2 ps pre-equilibration simulations were done to reach target temperature with 0.15 K temperature increase in each 1 fs timestep. For the slab calculations, we only applied the constant pressure algorithm to the two lattice vectors parallel to the 2D plane, leaving the third vector unchanged during the simulation.

## 7.3 Results

### 7.3.1 Intercalation of Quinone Molecules

We first optimized the lattice parameters and atomic coordinates of $Ti_3C_2O_2$ bilayer. The calculated in plane lattice parameter and interlayer separation are 3.02 and 2.58 Å, respectively. The relaxed structure of $Ti_3C_2O_2$ bilayer is used to construct hybrid structures composing of $Ti_3C_2O_2$ layers and molecular linkers. The optimized geometrical structures of $C_6H_4O_2$ and $C_6F_4O_2$ molecules are given in Fig. 7.1(a). These molecules are intercalated between $Ti_3C_2O_2$ monolayers to form pillared structures, which are depicted in Figs. 7.1(b) and (c). The calculated interlayer separation, $d$,

Table 7.1: Binding energies for adsorption at sites (see Fig. 7.3) I, II, III, IV, V and VI in eV.

| System | I | II | III | IV | V | VI |
|---|---|---|---|---|---|---|
| H-$Ti_3C_2O_2$ | 2.32 | 2.04 | 2.16 | 1.67 | V→I | VI→I |
| F-$Ti_3C_2O_2$ | 2.29 | 2.01 | 1.90 | IV→I | 1.70 | 2.29 |

is found to be 5.92 Å for $C_6H_4O_2$ and 6.35 Å for $C_6F_4O_2$. Upon intercalation, the C-O bond length of molecule enlarges from 1.24 (1.23) to 1.40 (1.38) Å for $C_6H_4O_2$ ($C_6F_4O_2$). While C-H bond lengths almost remain intact, C-C bond length changes 3-5.5% depending on the position of C atom. In the ground state structures, H atoms point to the midpoint of two neighboring surface O atoms to enhance attractive Coulomb interaction. These molecules may rotate around $z$-axis due to thermal effects. To check stability of the lowest energy intercalation structure of molecules against rotation, we calculated rotation barrier as shown in Fig. 7.2 for $C_6H_4O_2$. The calculated barrier is only 85 meV. Above room temperatures, molecules may swing between the lowest energy structures with the same energy.

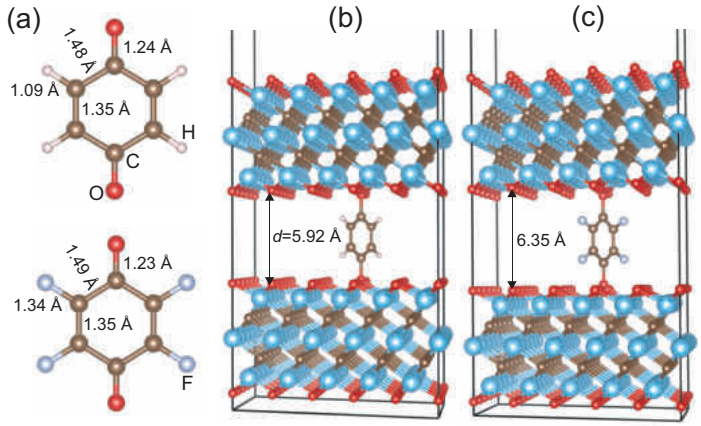


Figure 7.1: (a) The relaxed structure of $C_6H_4O_2$ and $C_6F_4O_2$ molecules. Various interatomic bond lengths are depicted for both molecules. The lowest energy intercalation structure of (b) $C_6H_4O_2$ and (c) $C_6F_4O_2$ between 5×5 $Ti_3C_2O_2$ monolayers. Here, $d$ is the interlayer separation.

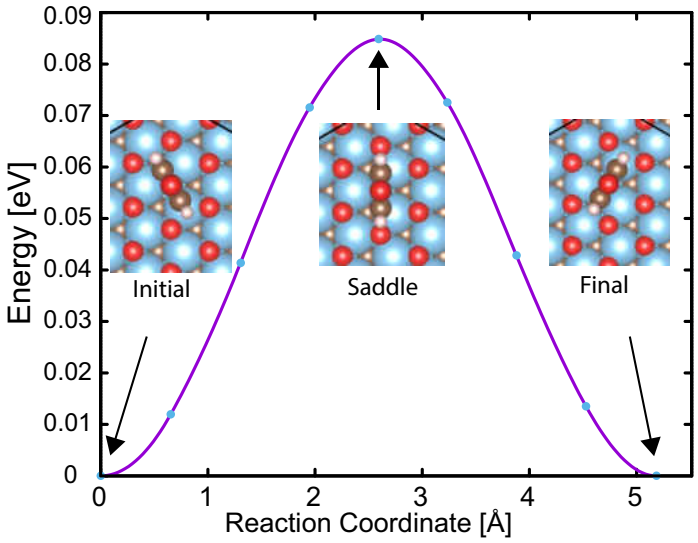


Figure 7.2: Rotation energy profile of intercalated $C_6H_4O_2$ molecule between the lowest energy adsorption structures for the 5×5 super cell structure. Insets show the initial, saddle and final point structures.

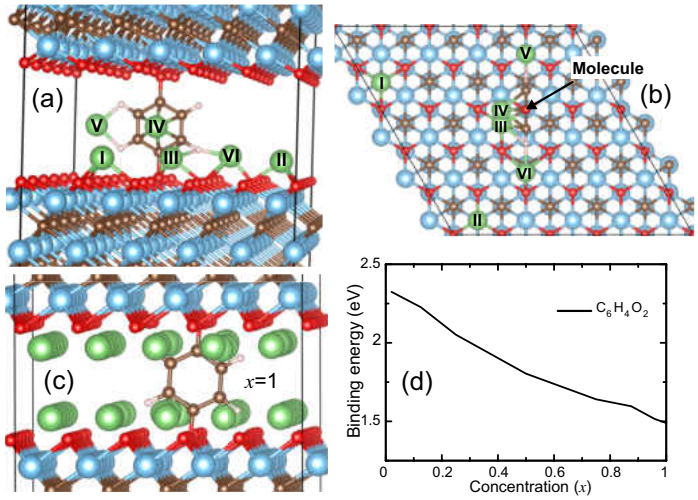


Figure 7.3: (a) Side and (b) top view of possible adsorption sites ( I, II, III, IV and V) for a single Li atom for a 5×5 super cell structure. (c) The relaxed structures of fully lithiated of H-$Ti_3C_2O_2$ . Variation of binding energy as a function of Li concentration ($x$) is depicted in (d).

### 7.3.2 Single Ion Intercalation

We next investigated a single Li atom intercalation in $Ti_3C_2O_2$ bilayer and pillared structures. To find out lowest energy adsorption site for the Li atom, we considered six different configurations, see Fig. 7.3. The binding energy, $E_b$[Li], of the Li atom

is defined through the following equation

$$E_b[\mathrm{Li}] = (E[\mathrm{pillar}] + n_{\mathrm{Li}}E[\mathrm{Li}] - E[\mathrm{pillar} + n_{\mathrm{Li}}\mathrm{Li}])/n_{\mathrm{Li}} \tag{7.1}$$

where $E[\mathrm{pillar} + n_{\mathrm{Li}}\mathrm{Li}]$ and $E[\mathrm{pillar}]$ are the total energies of the system with and without Li atom, respectively. $E[\mathrm{Li}]$ is the total energy of a Li atom in its most stable bcc bulk structure. Here, $n_{\mathrm{Li}}$ is the number of intercalated Li atoms. We also included the vdW interaction in the calculation of Li bulk energy. According to our binding energy definition, a more positive binding energy indicates a more favorable binding of Li. Table 7.1 summarizes the binding energy of a single Li ion at different sites depicted in Fig. 7.3 between $Ti_3C_2O_2$ layers. $E[\mathrm{Li}]$ in lowest energy configuration is about 2.32 eV for $C_6H_4O_2$ (Fig. 7.3(a)). Li atom prefers to sit at a hollow site formed by there O atoms with a C atom beneath the center. However, when Li is placed at the top of a Ti atom, $E_b[\mathrm{Li}]$ decreases by 0.28 eV due to repulsive interaction between the Li and Ti atoms. In $C_6H_4O_2$, Li ends up at site I, when it starts at sites V and VI at which the repulsive H-Li interaction pushes Li away from positively charged H atoms. Sites I and VI are the lowest energy sites and have almost the same binding energy for $C_6F_4O_2$. Deviation from site I is compensated by the attractive interaction between Li-F atoms. For $C_6F_4O_2$, Li tends to stay away from ring of molecule. Upon relaxation, Li migrates to a nearest hollow site on the surface of $Ti_3C_2O_2$. However, Li can stick to ring of $C_6H_4O_2$ with a $E[\mathrm{Li}]$ of 1.67 eV. In contrast to $C_6H_4O_2$ molecule, sites V and VI can be occupied by the Li atom in $C_6F_4O_2$ due to the attractive F-Li interaction. For completeness, we also calculated $E[\mathrm{Li}]$ for pristine bilayer $Ti_3C_2O_2$. $E[\mathrm{Li}]$ is considerably higher in pristine $Ti_3C_2O_2$ bilayer with a value of 2.98 eV. Intercalation of molecules between $Ti_3C_2O_2$ layers enlarges interlayer spacing and weakens the binding of Li. However, in pillared structures, we still have strong binding of Li atom on the surface, which

prevents undesired releasing of Li atoms as a result of thermal effects. Main role of molecules is to enlarge interlayer spacing. $Ti_3C_2O_2$ layers are the main hosts to store Li ions.

In addition to adsorption of single Li ion, we also studied the effect of the metal ion concentration on $E$[Li]. We only filled siteI on the surface of $Ti_3C_2O_2$ and calculated $E$[Li] as a function of number of intercalated Li atoms. In our 5×5×1 pillared structures shown in Fig. 7.1, we have 48 sites available for Li intercalation. Figure 7.3(b) shows the variation of $E$[Li] as a function of concentration of Li ions (i.e. $x$) adsorbed within pillared structures. Here, $x$ is defined as $n_{Li}/48$, where $n_{Li}$ is the number Li atoms. According to this definition, "1" (i.e. $n_{Li}$=48) means that two monolayers of Li are intercalated between $Ti_3C_2O_2$ layers. The first clear observation is that $E$[Li] decreases gradually with increase of concentration due to the enhanced repulsive interaction between the metal ions. $E$[Li] is always positive, suggesting that the pillared structures with Li atoms are energetically stable and thus we can safely disregard the phase separation problem up to $x$=1 for $C_6H_4O_2$ and $x$=0.92 for $C_6F_4O_2$. For $C_6F_4O_2$ structure, when $x$ is larger than 0.92, $C_6F_4O_2$ molecule dissociates, implying that the stability of $C_6F_4O_2$ is sensitive to $x$. F atoms move within pillared structure and, locally, bind to Li atoms. This result is correlated with the fact that LiF is a very stable compound and Li is very reactive towards F. Therefore, molecules with F termination should be avoided. In addition, LiF is one of compounds that is found in solid-electrolyte interface.[217]

### 7.3.3 Stability of Pillared Structures

To realize real battery applications, we need to address the cyclic stability of our hybrid structures against Li loading/unloading and thermal effects. Since our pillared structures contain molecular linkers, stability is particularly important to prevent chemical loss for long term usage, which ensures a good cycling stability. First of all,

our calculations showed that $C_6F_4O_2$ reacts with Li ions and decomposition reaction takes place at high Li concentrations. Thus, F contained quinone molecules are unstable against Li loading. For the binding energy and average voltage calculations, at each concentration, we equally and homogeneously distributed Li atoms on both surfaces within pillared structures shown in Fig. 7.1. When all Li atoms are placed on only one of the $Ti_3C_2O_2$ monolayers (i.e. for $x$=0.5), the 5×5 super cell structure of $Ti_3C_2O_2$-$C_6H_4O_2$-$Ti_3C_2O_2$ collapses in a such a way that individual $Ti_3C_2O_2$ layers approach each other and interlayer separation significantly decreases. $C_6H_4O_2$ molecule is stayed connected to $Ti_3C_2O_2$ monolayers. Here, there exists two competing interactions. The first one is the repulsive Coulomb interaction between the positively charged Li ions and the other one is the attractive interaction of Li ions with O atoms of $Ti_3C_2O_2$ surfaces. This collapsed structure is energetically favorable as compared to the other configuration where Li atoms are equally and homogeneously distributed on the surface of both $Ti_3C_2O_2$ layers.

To avoid this structural instability, we tested 3×3 and 4×4 super cell structures of $Ti_3C_2O_2$-$C_6H_4O_2$-$Ti_3C_2O_2$. Our calculations demonstrated that intermolecular separation is critical to realize a stable pillared structure. The 3×3 and 4×4 super cell structures are found to be stable against above mentioned one-side adsorption structure of Li.

To further confirm the stability of our pillared structures, we checked the variation of the lattice parameters and interatomic distances as a function of Li ion concentration for the 3×3 super cell size. We found that in-plane lattice parameters shrink less than 0.5% as the number of Li ions is increased. We found no bond breaking and the total expansion of whole system along the vertical direction is less than 1%, which is much smaller than that of traditional graphite anodes (10%).[218] The volume change mainly occurs along the $z$-direction, which is attributed to different bonding types. Due to interaction with Li ions, Ti-O bond length increases from 1.97 Å to 2.18 Å

when $x$ increases from 0 to 1.

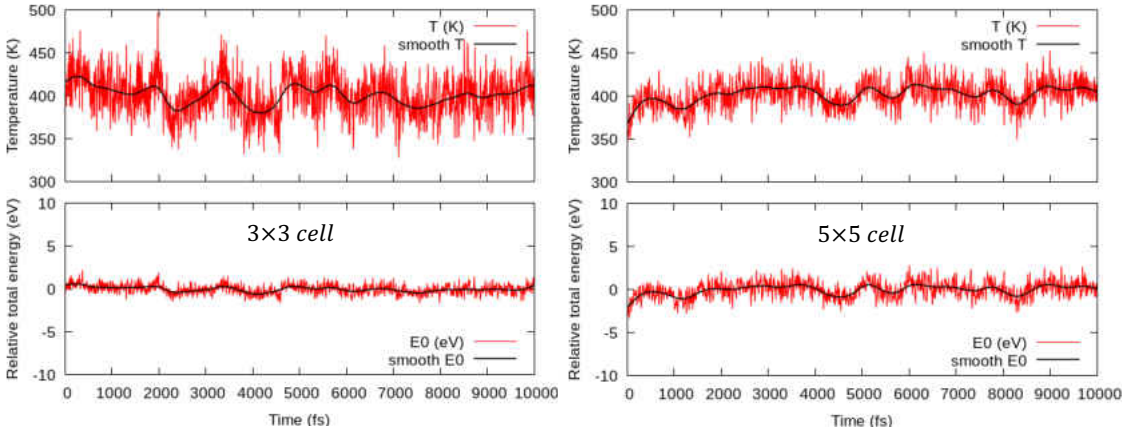


Figure 7.4: Temperature and total energy evaluation profiles in MD simulations for full coverage Li ion intercalation for 3×3 and 5×5 supercell structures at 400 K.

Thermal stability of pillared structures would have a large influence on the performance of battery. Ab-initio molecular dynamics (MD) simulations were performed to check stability of bilayer and bulk H-$Ti_3C_2O_2$ with full coverage of Li. We performed MD simulations for both 3×3 and 5×5 supercell structures to reveal the effect of system size. We selected temperatures 300 K and 400 K to see whether thermally induced perturbations will induce any structural transformation/distortion and Li release. Except one-side Li adsorption at $x$=0.5, the 5×5 supercell is quite stable against thermal motions. The total energy and temperature variations suggest that these systems are thermally stable at relatively high temperatures (Fig. 7.4). We found that the H-$Ti_3C_2O_2$ system is stable at this temperature for 10 ps without any structural deformation.

### 7.3.4 Electrochemical Properties

In order to gain insight into the electrochemical properties of the Li intercalation process into the 3×3 supercell structure of H-$Ti_3C_2O_2$, we obtained the open-circuit-voltage by calculating the averaged half cell voltage over a range of metal ion con-

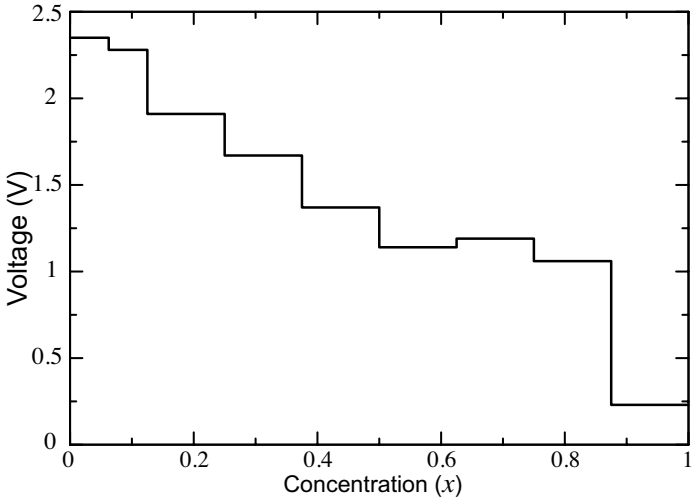


Figure 7.5: Calculated open circuit voltage, $V$, profile for Li-intercalation as a function of Li concentration ($x$).

centrations $x$, where $x_1 \leq x \leq x_2$, using,

$$(x_2 - x_1)\mathrm{M}^+ + (x_2 - x_1)e^- + \mathrm{H{-}Ti_3C_2O_2M}_{x_1} \leftrightarrow \mathrm{H{-}Ti_3C_2O_2M}_{x_2} \tag{7.2}$$

By the help of the above reaction, the average voltage, $V$, of H-$\mathrm{Ti_3C_2O_2M}_x$ in the concentration range of $x_1 \leq x \leq x_2$ can be estimated using,[219]

$$V \approx \frac{E[\mathrm{H-Ti_3C_2O_2M}_{x_1}] - E[\mathrm{H-Ti_3C_2O_2M}_{x_2}] + (x_2 - x_1)E[\mathrm{M}]}{(x_2 - x_1)e} \tag{7.3}$$

where $E$[H-$\mathrm{Ti_3C_2O_2M}_{x_1}$], $E$[H-$\mathrm{Ti_3C_2O_2M}_{x_2}$] and $E_{\mathrm{M}}$ are the total energy of H-$\mathrm{Ti_3C_2O_2M}_{x_1}$, H-$\mathrm{Ti_3C_2O_2M}_{x_2}$, and metallic M, respectively. According to above definition, voltage should be positive. In actual calculations of the average voltage, Gibbs free energy ($G(x)$=$\Delta E$+P$\Delta$V- T$\Delta$S) should be considered. However, in this expression, P$\Delta$V is only on the order of $10^{-5}$ eV and the entropy term (T$\Delta$S) is around 25 meV at room temperature, and hence the first term (i.e. internal energy change) is sufficient to estimate the average voltage.[219] $E_{\mathrm{Li}}$ is the total energy of bulk bcc Li. This simple formula allows us to estimate the voltage difference between two Li concentrations

(i.e. $x_1$ and $x_2$). Figure 7.5 shows the voltage as a function of Li concentration. First of all, our calculations show that the calculated voltage for Li intercalation decreases with increasing Li ion concentration. It is positive over whole considered concentration range, meaning that almost two monolayers of Li can be intercalated between $Ti_3C_2O_2$ layers in the presence of molecules, see Fig. 7.5. In contrast, pristine $Ti_3C_2O_2$ bilayer can only store only one monolayer of Li. In other words, when starting to intercalate the second layer of Li, the formation of bulk Li becomes energetically more favorable, which blocks the operation of battery. Theoretical capacity, $C$ (mAh/g), at maximum Li concentration ($x_{max}$) is computed using

$$C = \frac{x_{max} \times z \times F \times 10^3}{M_{\text{pillar}}} \tag{7.4}$$

where $z$ is the valence number of Li, $F$ is the Faraday constant (26.81 Ah/mol) and $M_{\text{pillar}}$ is the atomic mass of pillared structure. The calculated $C$ is found to be 253.2 mAh/g which is much larger than $C$ of pristine $Ti_3C_2O_2$ (134.3 mAh/g), indicating that pillared structures offer significant capacity enhancement.

### 7.3.5 Diffusion Barrier

We considered three criteria to uncover the potential of pillared structures for battery applications. These are binding energy of Li, average voltage and migration diffusion barriers as a function of Li concentration. Besides having a doubled storage capacity (with respect to pristine $Ti_3C_2O_2$ bilayer) determined by average voltage, a low diffusion barrier and high mobility of ions are one of the essential requirements for the efficient $Ti_3C_2O_2$ based electrodes. In particular, mobility is a key factor to evaluate the rate performance at which a battery can be charged and discharged. In this respect, we also investigated Li diffusion barriers along different migration paths at different Li concentrations.

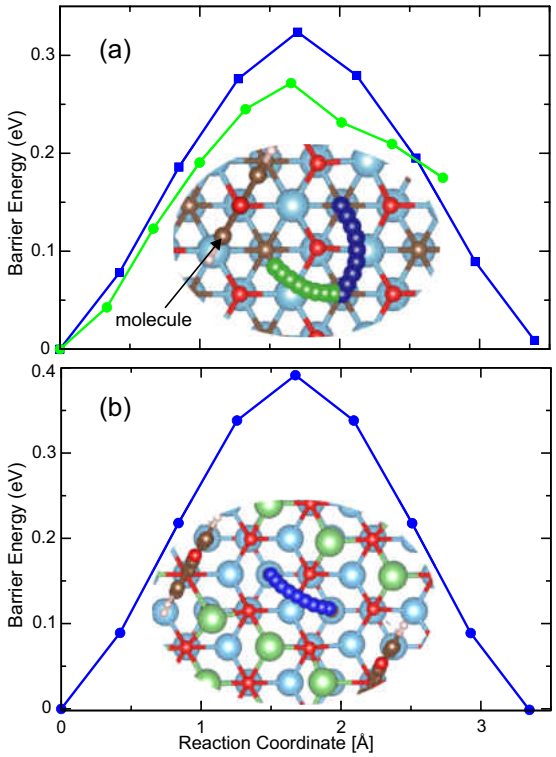


Figure 7.6: Diffusion barrier profiles and optimized migration pathways between two nearest lowest energy sites of Li atom at (a) $x$= 0.0625 and (b) $x$=0.875. Migrating Li atoms are denoted by blue and green color to distinguish them from other Li atoms.

For pristine $Ti_3C_2O_2$ bilayer, we only considered one diffusion path, which connects two adjacent lowest energy binding sites on a 5×5 surface cell with a single Li atom ion. $E_{diff}$ for pristine $Ti_3C_2O_2$ monolayer and bilayer (not shown) are calculated as 0.31 and 0.97 eV, respectively. Such a high migration barrier for bilayer $Ti_3C_2O_2$ is due to the presence of the geometric constraint in bilayer such that the Li atom should travel between two surfaces of monolayers. Therefore, one may expect a slow charging/discharging rates for batteries based on pristine $Ti_3C_2O_2$ multilayers. As predicted in previous works,[220,221] the diffusion barriers are quite low on MXene without functional groups.

Figure 7.6 shows the diffusion barriers ($E_{diff}$) and optimized pathways for selected systems with different Li concentrations in pillared structure with a 3×3 surface cell. The most important observation is that Li displays about three times smaller on-

plane diffusion barriers as compared to pristine $Ti_3C_2O_2$ bilayer. Due to presence of intercalated molecule, $E_{diff}$ approaches monolayer limit. For instance, at an interlayer distance of 5.99 Å, $E_{diff}$ is calculated as 0.32 eV for $x$=0.0625 . As expected, Li migration barrier is concentration dependent due to the interaction between the $Li^+$ ions. One might expect to see an increasing effect of the barrier energies with increasing concentration. For instance, at $x$= 0.875 (see Fig. 7.6(b)), $E_{diff}$ becomes only 0.40 eV. These values are still lower than the migration barrier of graphite with a diffusion barrier around 0.5 eV,[222] high-capacity bulk silicon anode materials with a diffusion barrier around 0.57 eV[223] and commercially used anode materials based on $TiO_2$ with a barrier of 0.35-0.65 eV.[224–226] The marked reduction in diffusion barriers comes from two factors; (1) an increase of interlayer separation because of molecular linkers and (2) notable decrease of Li binding energy. Our calculations also indicated that interlayer migration of Li ions is quite unlikely due to high barrier energy as a result of strong binding of Li on the surface. The calculated barrier energy is around 1 eV. This means that Li ions spend their time on the surface on which they are absorbed. We also investigated the effect of molecule concentration on diffusion barriers. $E_{diff}$ values were calculated for both 3×3 and 5×5 surface cell structures. For the 3×3 (5×5) supercell structure, the separation between the molecules is at least 5.85 (11.67) Å. Interestingly, $E_{diff}$ values mildly depend on the molecule concentration. Depending on concentration and diffusion path, $E_{diff}$ falls into a range of [0.27-0.40] ([0.29-0.34]) eV for the 3×3 (5×5) supercell structure. As a comparison, $E_{diff}$ for graphite varies between 0.42 and 0.56 eV depending on diffusion path for large Li concentrations.[222] We showed that, for an almost full coverage, the energy barriers are still about 0.1 eV lower than the graphite ($LiC_6$). Although 0.1 eV difference seems a small difference, it gives almost 50 times higher mobility when approximated with Arrhenius law.

## 7.4 Conclusion

We demonstrated that interlayer expansion in $Ti_3C_2O_2$ multilayers via molecular linkers is a promising strategy to overcome the limitations, including low storage capacity and slow kinetics, for batteries based on not only MXenes but also other 2D materials. In proposed pillared structures, the improved large capacity accompanies with fast ion transport. Due to enlarged interlayer separation, our pillared structures could serve as model systems to store Na and multivalent ions (such as $Mg^{2+}$, $Zn^{2+}$ and $Al^{3+}$) as well. Presence of an enlarged interlayer separation is utilized to intercalate about two layers of Li ions between $Ti_3C_2O_2$ layers with a positive open circuit voltage for Li intercalation. In contras to $Ti_3C_2O_2$ bilayer without molecular linker, Li migrates between in-plane lowest energy sites with small energy barriers of 0.27-0.40 eV depending on Li concentration. Interlayer ion diffusion is prohibited due to large barrier energy. Stability of pillared structure is sensitive to lateral size of the $Ti_3C_2O_2$ bilayer, Li ion concentration and adsorption structure of Li ions. Whereas a $5\times5$ supercell exhibits instabilities in certain adsorption structures, the $3\times3$ and $4\times4$ supercell structures are stable for the same adsorption structures of Li.

# CHAPTER VIII

# SUMMARY AND DISCUSSIONS

Chapter I discussed the importance of two-dimensional (2D) materials for spintronics and energy applications. Among the 2D materials, it could be shown that MXenes can be effectively utilized to produce battery electrodes and spintronics applications due to their high mechanical and dynamical stability, electronic conductivity, and tunability of electronic and magnetic properties using various techniques.

Chapter II reviewed the details of the theoretical background of density functional theory (DFT). Due to a large number of electrons of materials and their interactions, it is difficult to solve the Schrödinger equation based on many-body Hamiltonian. Therefore, the Hartree-Fock theory considers non-interacting single electron Hamiltonian with exchange potential. As a result of omitting correlation potential, Hartree-Fock is not much accurate. This chapter discussed how DFT minimizes the differences between many-body and single-electron Hamiltonians by taking into account the correlation effects. Since this dissertation carried out spin-polarized calculations to study the ferromagnetic materials, spin density functional theory was addressed. VASP software was used for DFT calculations of all the projects related to this dissertation. VASP uses a plane wave basis set to construct the wavefunctions of the non-interacting electrons. Thus, this chapter explained how to implement DFT with a plane-wave basis set.

Chapter III considered $Hf_2MnC_2O_2$ and $Hf_2VC_2O_2$ MXenes due to their ferromagnetic and semiconductor properties. The importance of those materials is that the conduction bands are highly sensitive to both biaxial and uniaxial strains. As a result,

strain engineering can be exploited to turn semiconductor monolayers into metallic or semi-metallic ones depending on the size and type of applied strain. For instance, a semiconductor to metal transition occurs at -3% compression and 8% tension in $Hf_2MnC_2O_2$, and also at -2% compression and 9% tension in $Hf_2VC_2O_2$. Electron and hole effective masses are able to be tuned significantly. The ferromagnetic phase becomes stronger (weaker) as compared to the anti-ferromagnetic phase of both types of monolayers by applying biaxial tensile (compressive) strain. We could show that the above results are almost the same under uniaxial strain for Mn-based monolayer.

Chapter IV used an approach to investigate the magnetic and electronic properties of $Hf_2MnC_2O_2$ and $Hf_2VC_2O_2$ by exploiting realistic surface terminations via creating surface defects including oxygen vacancies and H adatoms. We found that introducing surface oxygen vacancies or hydrogen adatoms is able to modify the electronic structures, magnetic anisotropies, and exchange couplings. Depending on the defect concentration, a ferromagnetic half-metallic state can be realized for both $Hf_2VC_2O_2$ and $Hf_2MnC_2O_2$. Bare $Hf_2VC_2O_2$ exhibits easy-axis anisotropy, whereas bare $Hf_2MnC_2O_2$ exhibits easy-plane anisotropy; however, defects can change the latter to easy-axis anisotropy, which is preferable for spintronics applications. The considered defects were found to modify the magnetic anisotropy by as much as 500%. Defects also produce an inhomogeneous pattern of exchange couplings, which can further enhance the Curie temperature. In particular, $Hf_2MnC_2O_2H_{0.22}$ was predicted to have a Curie temperature of about 171 K due to a combination of easy-axis anisotropy and a connected network of enhanced exchange couplings.

Chapter V selected $Ti_2CO_2$ and B-doped graphene ($\approx 8\%$) to model heterostructures and bilayers due to their low molecular weight and good electrical conductivity. Highly abundant Na and Mg are convenient to lower the production cost of energy-storage. In this study, we examined the suitability of Na and Mg intercalation in $Ti_2CO_2$/B-doped-graphene heterostructures and B-doped-graphene (B-Gr)

bilayers. Even though Na and Mg intercalated bare graphene bilayers are not energetically stable, our studies reveal that (B-Gr) bilayers facilitate the storing of those ions. As a consequence of smaller atomic size, Mg intercalated systems show low structural deformations and interlayer distance change ($\leq$ 0.5 Å) and low in-plane lattice constant change ($\leq$ 0.1%), indicating good mechanical stability during the charging/discharging process. The considered bilayers provide higher capacities than MXene based heterostructure. Na and Mg intercalated $Ti_2CO_2$/B-Gr systems allow 240.4 mAh/g and 295.1 mAh/g storage capacities, respectively. In comparison, the calculated gravimetric storage capacities for Na and Mg intercalated B-Gr bilayers are 283.8 mAh/g and 320.6 mAh/g, respectively. All the intercalated ion systems provide average voltages greater than 0.75 V. Our diffusion barrier calculations revealed that very low diffusion barriers, as small as 0.18 eV, are expected for the Na intercalated systems, offering fast charging/discharging rates for the battery applications.

Chapter VI studied the stability and structural, electrochemical, and ion dynamic properties of Li adsorbed on sulfur-functionalized group 3B, 4B, 5B, and 6B transition metal (M)-based MXenes (i.e., $M_2CS_2$ with M= Sc, Ti, Zr, Hf, V, Nb, Ta, Cr, Mo, and W). We performed phonon calculations, which indicate that all the above $M_2CS_2$ MXenes, except for Sc, are dynamically stable at T = 0 K. The ground-state structure of each $M_2CS_2$ monolayer depends on the type of M atom. For instance, while sulfur prefers to sit at the FCC site on $Ti_2CS_2$, it occupies the HCP site of Cr-based MXene. We determined the Li adsorption configurations at different concentrations using the cluster expansion method. The highest maximum open-circuit voltages were computed for group 4B element (i.e., Ti, Zr, and Hf)-based $M_2CS_2$, which are larger than 2.1 V, while their average voltages are approximately 1 V. The maximum voltage for group 6B element (i.e., Cr, Mo, W)-based $M_2CS_2$ are less than 1 V, and the average voltage is less than 0.71 V. We found that S functionalization is helpful for capacity improvements over the O-terminated MXenes. In this respect,

the computed storage gravimetric capacity may reach up to 417.4 $mAhg^{-1}$ for $Ti_2CS_2$ and 404.5 $mAhg^{-1}$ for $V_2CS_2$. Ta, Cr, Mo, and W-based $M_2CS_2$ MXenes show very low capacities, which are less than 100 $mAhg^{-1}$.

Chapter VII demonstrated that high lithium storage capacity and fast kinetics are achieved for $Ti_3C_2O_2$ by preintercalating organic molecules. As a proof-of-concept, two different quinone molecules, namely 1,4-Benzoquinone ($C_6H_4O_2$) and Tetrafluoro-1,4-benzoquinone ($C_6F_4O_2$) were selected as the molecular linkers to demonstrate the feasibility of this interlayer engineering strategy for energy storage. As compared to $Ti_3C_2O_2$ bilayer without linker molecules, our pillared structures facilitate a much faster ion transport, promising a higher charge/discharge rate for Li. For example, while the diffusion barrier of a single Li ion within pristine $Ti_3C_2O_2$ bilayer is at least 1.0 eV, it becomes 0.3 eV in pillared structures, which is comparable and even lower than that of commercial materials. At high Li concentrations, the calculated diffusion barriers are as low as 0.4 eV. Out-of-plane migration of Li ions is hindered due to large barrier energy with a value of around 1-1.35 eV. Concerning storage capacity, we can only intercalate one monolayer of Li within pristine $Ti_3C_2O_2$ bilayer. In contrast, pillared structures offer significantly higher storage capacity. Our calculations showed that at least two layers of Li can be intercalated between $Ti_3C_2O_2$ layers without forming bulk Li and losing the pillared structure upon Li loading/unloading. A small change in the in-plane lattice parameters ($<0.5\%$) and volume ($<1.0\%$), and ab-initio molecular dynamics simulations prove the stability of the pillared structures against Li intercalation and thermal effects. Intercalated molecules avoid the large contraction/expansion of the whole structure, which is one of the key problems in electrochemical energy storage. Pillared structures allow us to realize electrodes with high capacity and fast kinetics. Our results open new research paths for improving the performance of not only MXenes but also other layered materials for supercapacitor and battery applications.

# APPENDICES

## A.1 Additional Calculations Under Biaxial Strain

### A.1.1 The Calculations Using GGA (without U) and HSE06

Here, we calculated the electronic band structures under -4%, 0% and 4% strains for both $Hf_2MnC_2O_2$ and $Hf_2VC_2O_2$ 2D materials. It is clear that the DFT calculations provide zero band gap electronic band structures for the unstrained and $\epsilon = 4\%$ cases where DFT+U and hybrid functional calculations indicate those materials are semiconductors.

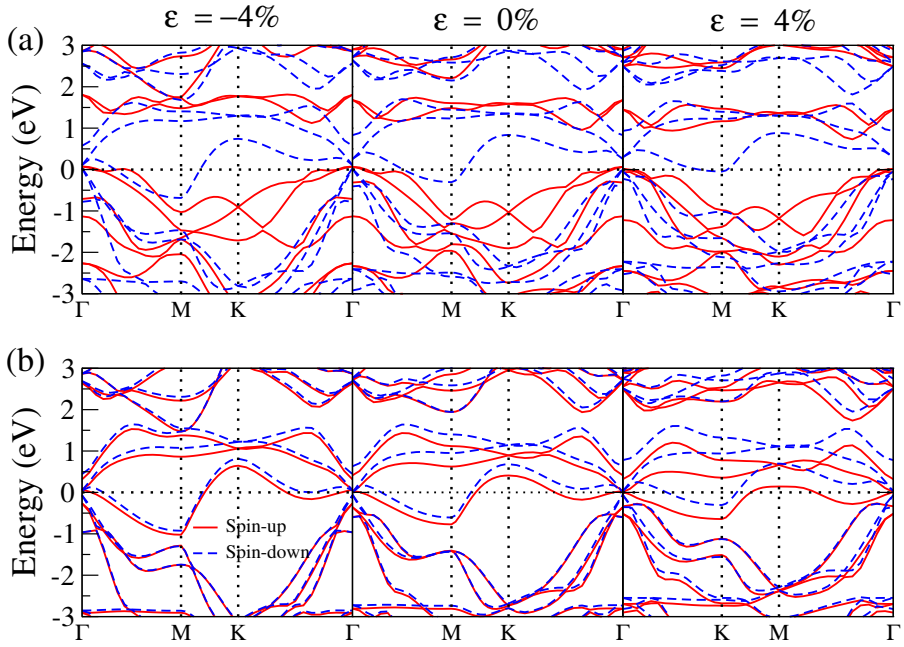


Figure A1: Electronic band structures for (a) $Hf_2MnC_2O_2$ and (b) $Hf_2VC_2O_2$ under $-4\%$, 0% and 4% biaxial strains using DFT calculations

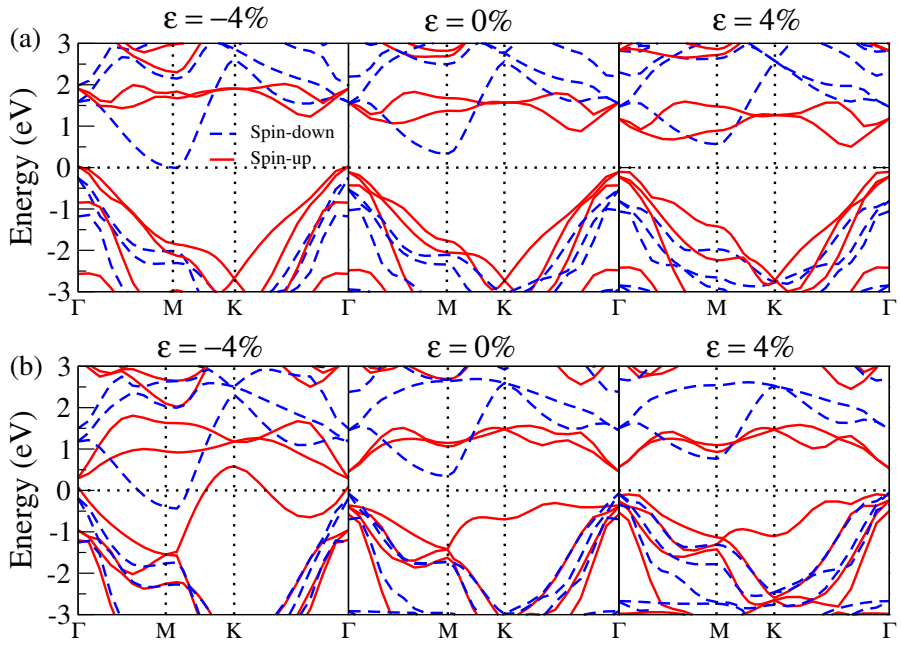


Figure A2: Electronic band structures for (a) $Hf_2MnC_2O_2$ and (b) $Hf_2VC_2O_2$ under $-4\%$, $0\%$ and $4\%$ biaxial strains using hybrid functional calculations

Table A1: The band gap and the total magnetic moment values of $Hf_2MnC_2O_2$ using DFT, DFT+U and HSE06 methods

| Strain | | DFT | DFT+U | HSE06 |
|---|---|---|---|---|
| $-4\%$ | $E_g$ (eV) | 0 | 0 | 0 |
| | $\mu$ ($\mu_B$) | 2.461 | 2.966 | 2.976 |
| $0\%$ | $E_g$ (eV) | 0 | 0.282 | 0.484 |
| | $\mu$ ($\mu_B$) | 2.759 | 3.000 | 3.000 |
| $4\%$ | $E_g$ (eV) | 0 | 0.268 | 0.665 |
| | $\mu$ ($\mu_B$) | 2.964 | 3.000 | 3.000 |

Table A2: The band gap and the total magnetic moment values of $Hf_2VC_2O_2$ using DFT, DFT+U and HSE06 methods

| Strain | | DFT | DFT+U | HSE06 |
|---|---|---|---|---|
| $-4\%$ | $E_g$ (eV) | 0 | 0 | 0 |
| | $\mu$ ($\mu_B$) | 0.207 | 0.791 | 0.790 |
| $0\%$ | $E_g$ (eV) | 0 | 0.149 | 0.422 |
| | $\mu$ ($\mu_B$) | 0.311 | 1.000 | 1.000 |
| $4\%$ | $E_g$ (eV) | 0 | 0.223 | 0.630 |
| | $\mu$ ($\mu_B$) | 0.5837 | 1.000 | 1.000 |

### A.1.2 Rectangular Super-Cell Structure

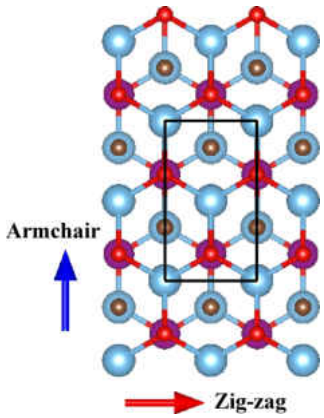


Figure A3: Rectangular Super-cell structure for out-of-plane Poisson's ratio calculations

### A.1.3 Multi-layer Structure for Calculating the Thickness

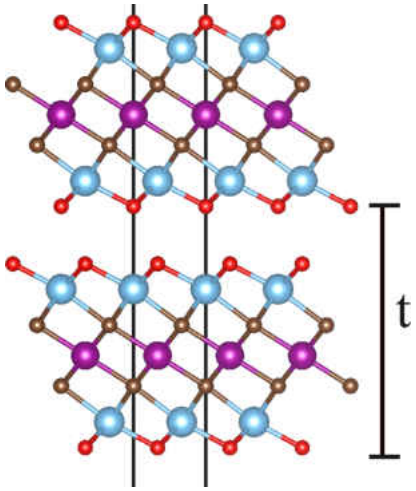


Figure A4: Multi-layer structure for calculating the thickness (t) of the monolayers

## A.2 Additional Calculations Under Uniaxial Strain

### A.2.1 Phonon Dispersion

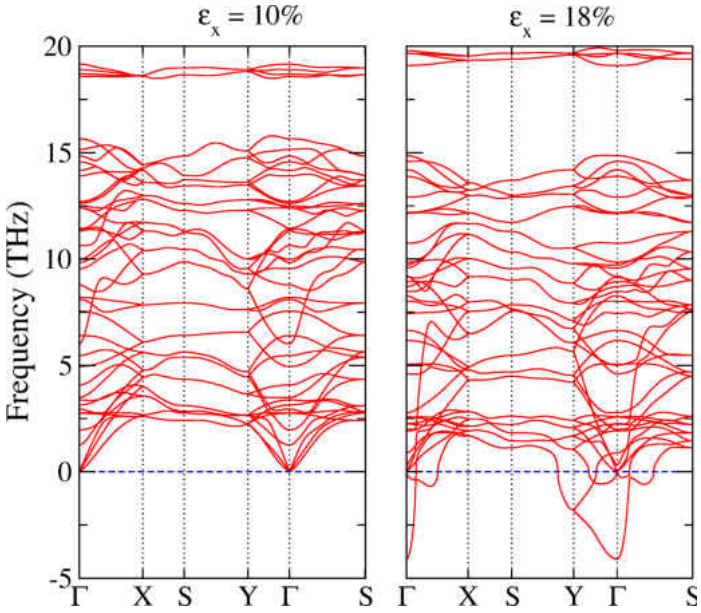


Figure A5: The phonon calculations for 10% and 18% tensile strain in zig-zag direction.

### A.2.2 The Calculations Using GGA (without U) and HSE06

GGA calculations show that $Hf_2MnC_2O_2$ MXene is a metal which does not change its band structure significantly under the uniaxial strain (see Fig. A6). On the contrary, HSE06 calculations confirms that the bands are shifting as seen in the GGA+U method. Both HSE06 and the GGA+U methods prove that strain free $Hf_2MnC_2O_2$ is a semiconductor.

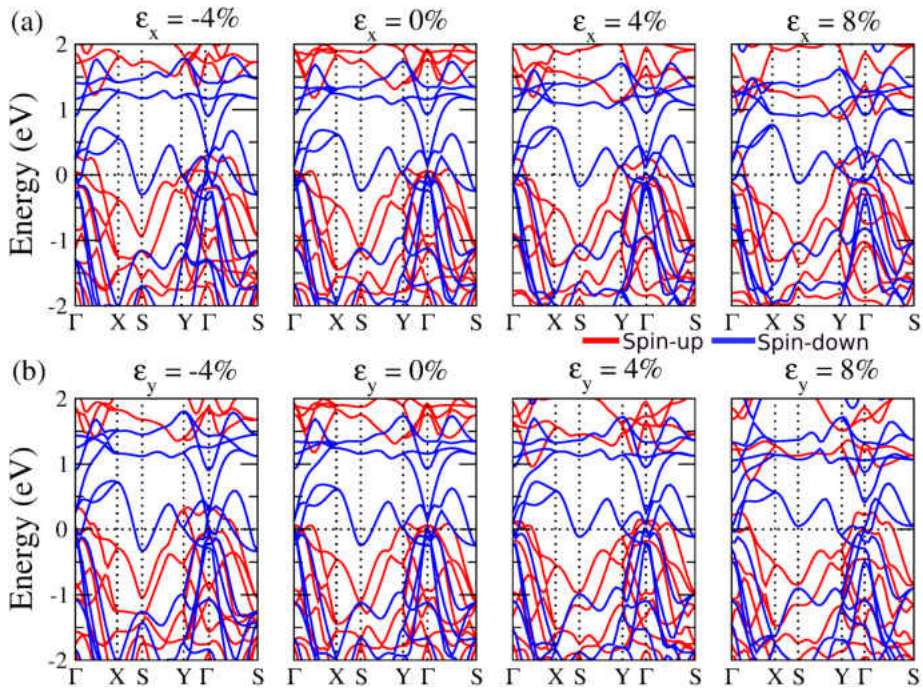


Figure A6: Electronic band structures for $Hf_2MnC_2O_2$ under -4%, 0% and 4% uniaxial strains in (a) x and (b) y directions using DFT calculations. Spin-up and spin-down bands are in red and blue, respectively. Fermi energy marks zero energy.

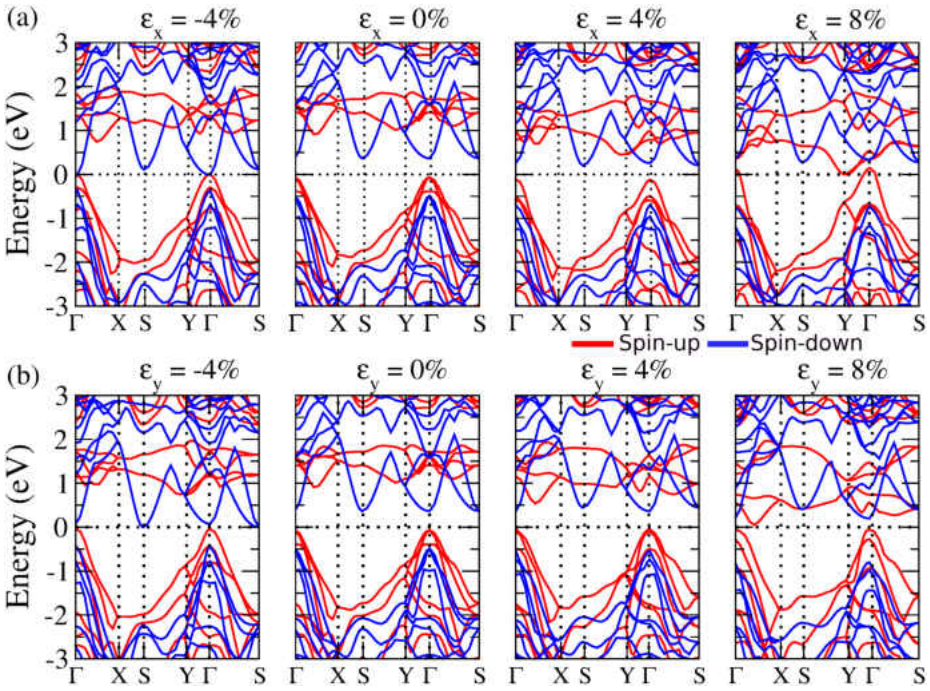


Figure A7: Electronic band structures for $Hf_2MnC_2O_2$ under -4%, 0% and 4% uniaxial strains in (a) x and (b) y directions using HSE06 calculations. Spin-up and spin-down bands are in red and blue, respectively. Fermi energy marks zero energy.

Table A3: The band gap ($E_g$) and the total magnetic moment ($\mu$) values of $Hf_2MnC_2O_2$ using DFT, DFT+U and HSE06 methods under uniaxial strain in zig-zag direction

| Strain | | DFT | DFT+U | HSE06 |
|---|---|---|---|---|
| -4% | $E_g$ (eV) | 0 | 0 | 0 |
| | $\mu$ ($\mu_B$) | 2.543 | 2.989 | 3.000 |
| 0% | $E_g$ (eV) | 0 | 0.282 | 0.484 |
| | $\mu$ ($\mu_B$) | 2.674 | 3.000 | 3.000 |
| 4% | $E_g$ (eV) | 0 | 0.239 | 0.324 |
| | $\mu$ ($\mu_B$) | 2.750 | 3.000 | 3.000 |
| 8% | $E_g$ (eV) | 0 | 0 | 0 |
| | $\mu$ ($\mu_B$) | 2.746 | 3.000 | 3.000 |

Table A4: The band gap ($E_g$) and the total magnetic moment ($\mu$) values of $Hf_2MnC_2O_2$ using DFT, DFT+U and HSE06 methods under uniaxial strain in arm-chair direction

| Strain | | DFT | DFT+U | HSE06 |
|---|---|---|---|---|
| -4% | $E_g$ (eV) | 0 | 0 | 0 |
| | $\mu$ ($\mu_B$) | 2.547 | 2.996 | 3.000 |
| 0% | $E_g$ (eV) | 0 | 0.282 | 0.484 |
| | $\mu$ ($\mu_B$) | 2.674 | 3.000 | 3.000 |
| 4% | $E_g$ (eV) | 0 | 0.233 | 0.415 |
| | $\mu$ ($\mu_B$) | 2.796 | 3.000 | 3.000 |
| 8% | $E_g$ (eV) | 0 | 0.0184 | 0.103 |
| | $\mu$ ($\mu_B$) | 2.783 | 3.000 | 3.000 |

### A.2.3 Energy Differences Between Nonmagnetic and Ferromagnetic Phases

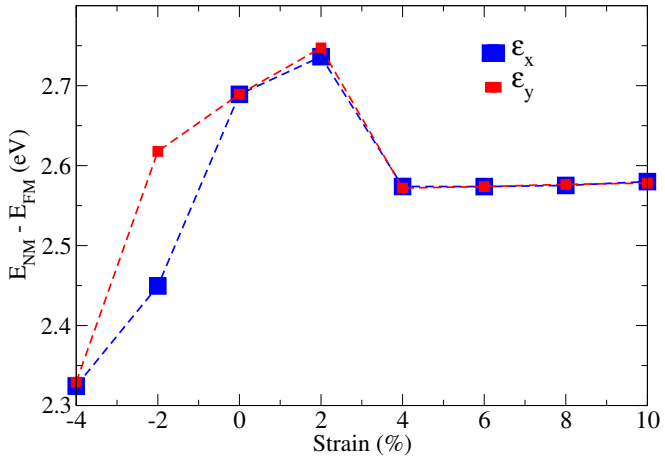


Figure A8: Energy difference $E_{\mathrm{NM}} - E_{\mathrm{FM}}$ per unit formula as a function of uniaxial strain

### A.2.4 Cohesive Energy

The cohesive energy ($E_{\mathrm{coh}}$) of the strain free monolayer is -1.949 eV per atom. As can be seen in the Fig A9, the cohesive energy increases, while strain is applied. Within the range of -4% to 10%, this value remains less than zero.

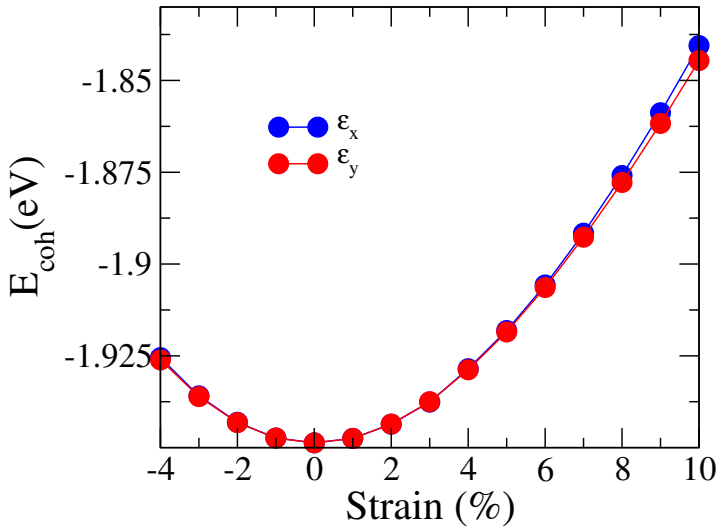


Figure A9: Cohesive energy ($E_{\mathrm{coh}}$) as a function of strain

## A.3 Additional Calculations for B-Doped-Graphene Based Electrodes

### A.3.1 The Voltage and Gravimetric Capacity for Different B Concentrations in B-Gr Bilayers

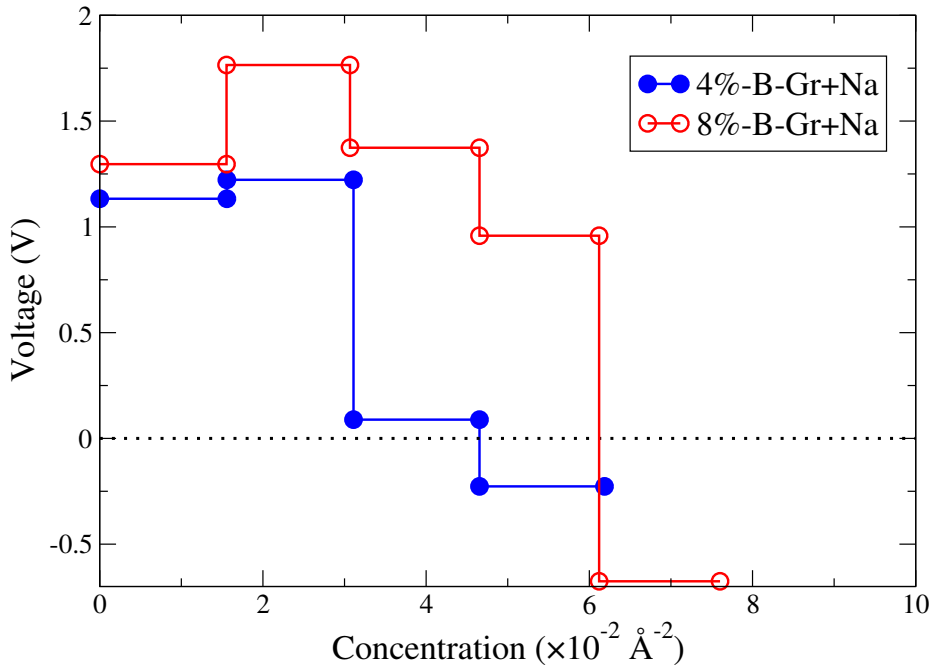


Figure A10: Cohesive energy ($E_{\text{coh}}$) as a function of strain

Table A5: The gravimetric capacity for 4% and 8% doping concetrations.

| B Concentration | Gravimetric Capacity (mAh/g) |
|---|---|
| 4% | 212.88 |
| 8% | 283.83 |

### A.3.2 The Supercells of B-Gr Bilayers Without Ions

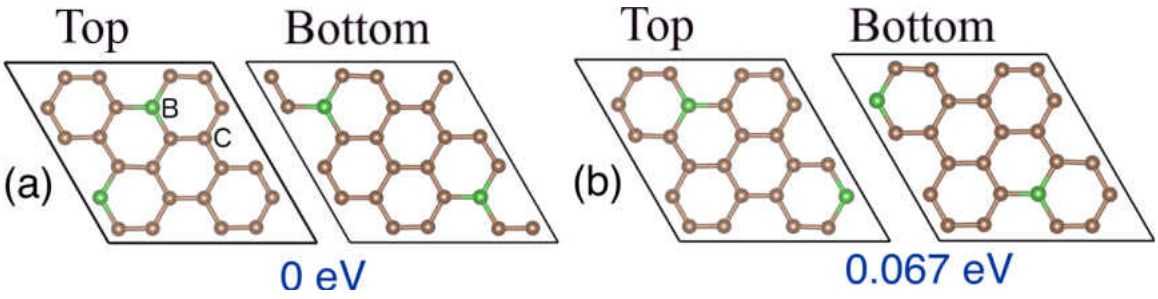


Figure A11: Top views of top and bottom layers of (a) AB and (b) AA stacking of B-Gr bilayers without ions. The total energy of each system relative to the ground state is stated in blue.

### A.3.3 The Sites of the B Atoms in Na Intercalated B-Gr Bilayers

The following Fig. A12, A13, A14, A15 and A16 show the total energies with respect to the ground state for several structures. Those supercells were considered to find the ground states of $0.004\text{Å}^{-2}$, $0.02\text{Å}^{-2}$, $0.03\text{Å}^{-2}$, $0.05\text{Å}^{-2}$ and $0.06\text{Å}^{-2}$ Na intercalated B-Gr bilayers, respectively.

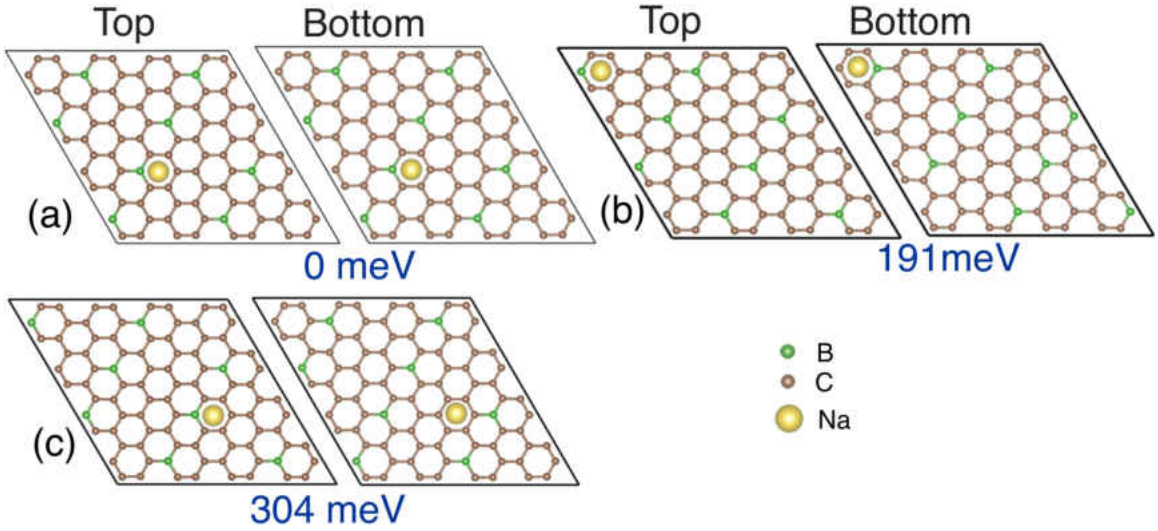


Figure A12: Top views of top and bottom layers of (a) AB and (b) AA stacking of B-Gr bilayers without ions. The total energy of each system relative to the ground state is stated in blue.

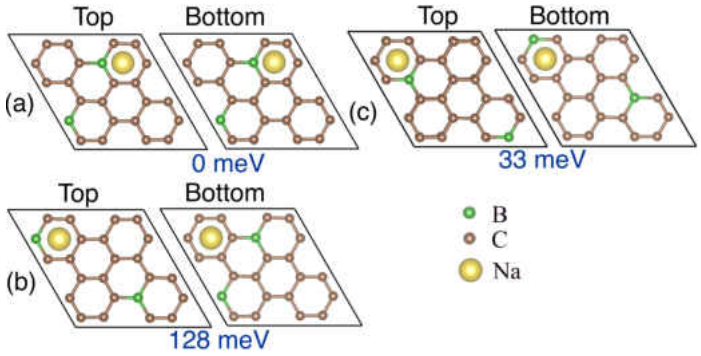


Figure A13: Top views of top and bottom layers of bilayer with $0.02\text{Å}^{-2}$ concentration of Na (1 ion per $2\sqrt{3}\times2\sqrt{3}$ supercell). The total energy of each system is stated in blue.

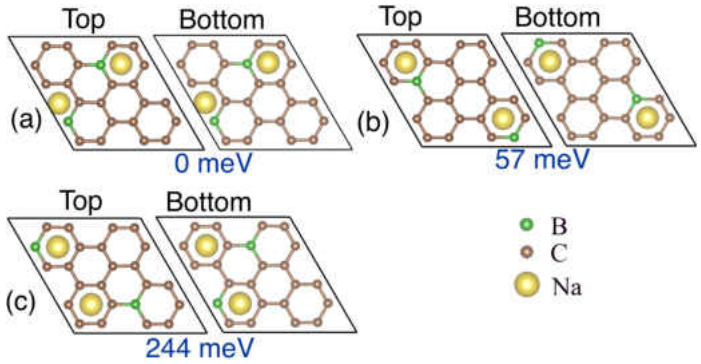


Figure A14: Top views of top and bottom layers of bilayer with $0.03\text{Å}^{-2}$ concentration of Na (2 ions per $2\sqrt{3}\times2\sqrt{3}$ supercell). The total energy of each system is stated in blue.

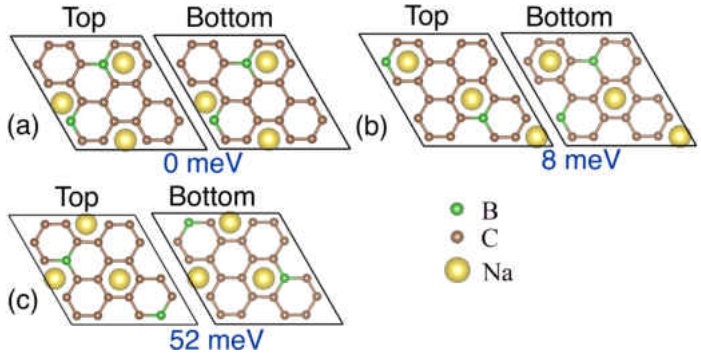


Figure A15: Top views of top and bottom layers of bilayer with $0.05\text{Å}^{-2}$ concentration of Na (3 ions per $2\sqrt{3}\times2\sqrt{3}$ supercell). The total energy of each system is stated in blue.

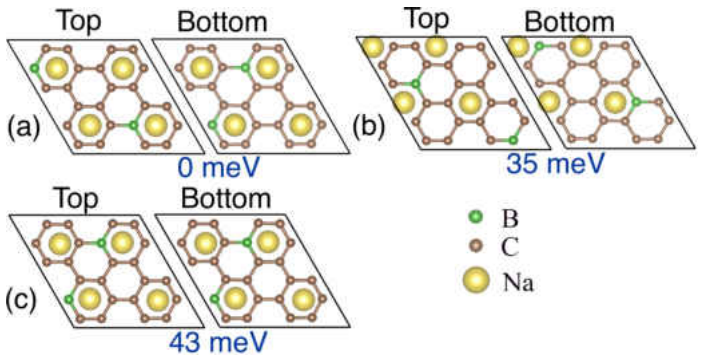


Figure A16: Top views of top and bottom layers of bilayer with 0.06Å$^{-2}$ concentration of Na (4 ions per $2\sqrt{3}\times2\sqrt{3}$ supercell). The total energy of each system is stated in blue.

### A.3.4 The Sites of the B Atoms in Mg Intercalated B-Gr Bilayers

The following Fig. A17, A18, A19, A20 and A21 show the total energies with respect to the ground state for several structures. Those supercells were considered to find the ground states of 0.004Å$^{-2}$, 0.02Å$^{-2}$, 0.03Å$^{-2}$, 0.05Å$^{-2}$ and 0.06Å$^{-2}$ Mg intercalated B-Gr bilayers, respectively.

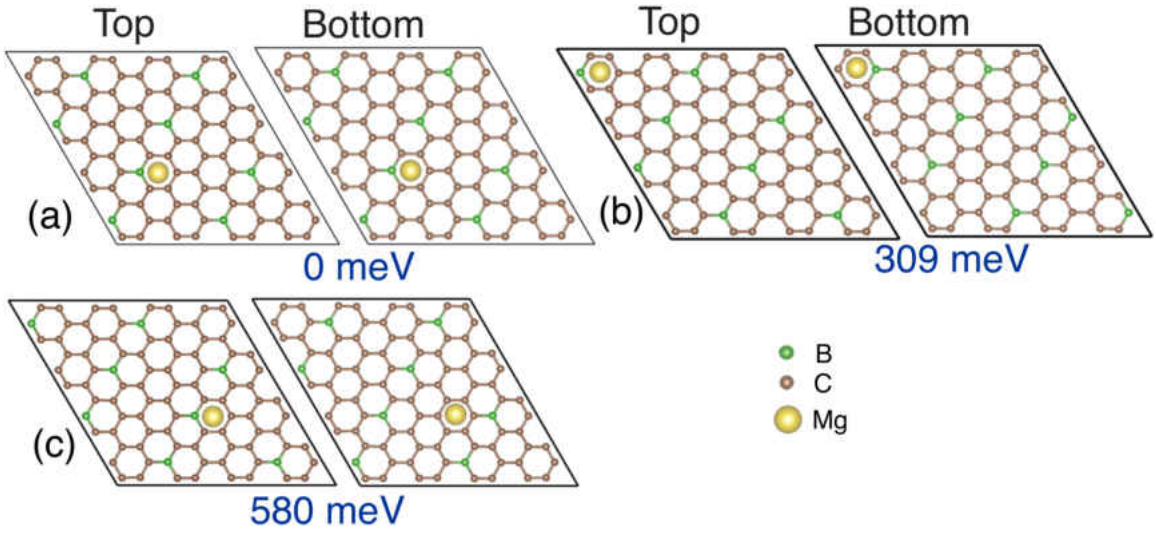


Figure A17: Top views of top and bottom layers of (a) AB and (b) AA stacking of B-Gr bilayers without ions. The total energy of each system relative to the ground state is stated in blue.

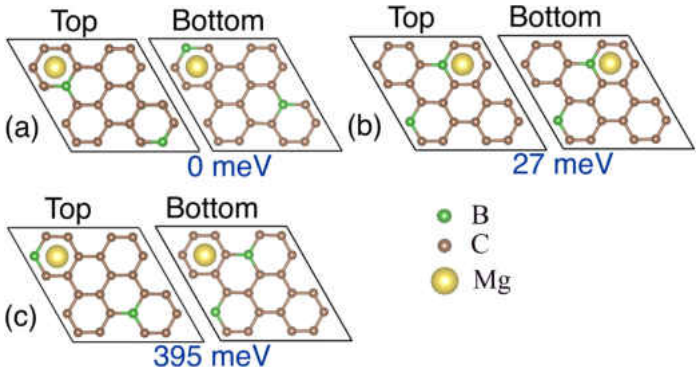


Figure A18: Top views of top and bottom layers of bilayer with $0.02\text{Å}^{-2}$ concentration of Mg (1 ion per $2\sqrt{3}\times2\sqrt{3}$ supercell). The total energy of each system is stated in blue.

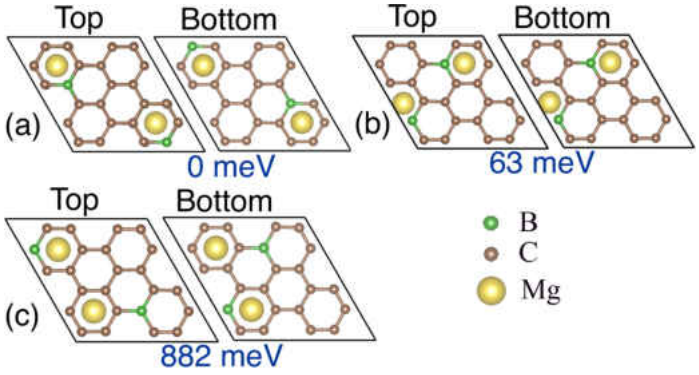


Figure A19: Top views of top and bottom layers of bilayer with $0.03\text{Å}^{-2}$ concentration of Mg (2 ions per $2\sqrt{3}\times2\sqrt{3}$ supercell). The total energy of each system is stated in blue.

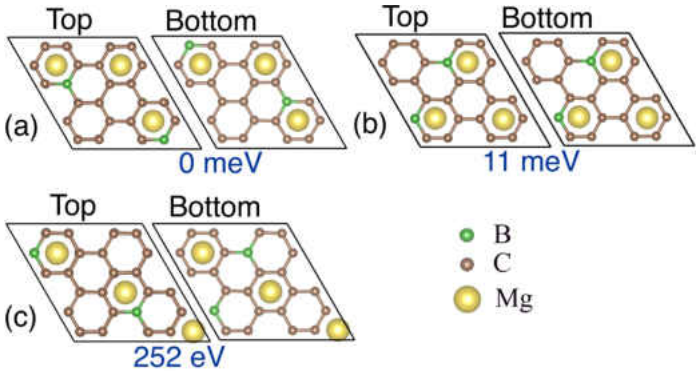


Figure A20: Top views of top and bottom layers of bilayer with $0.05\text{Å}^{-2}$ concentration of Mg (3 ions per $2\sqrt{3}\times2\sqrt{3}$ supercell). The total energy of each system is stated in blue.

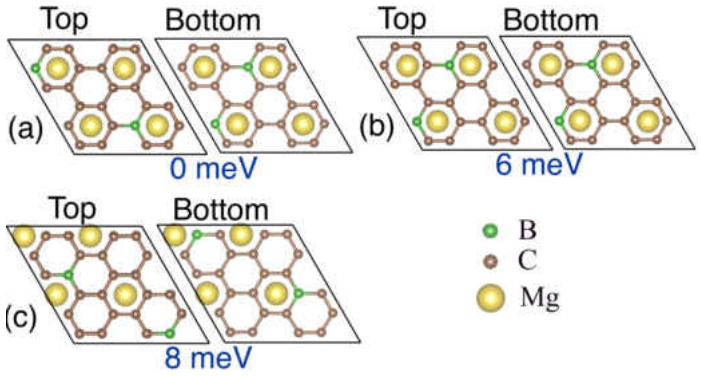


Figure A21: Top views of top and bottom layers of bilayer with $0.06\text{Å}^{-2}$ concentration of Mg (4 ions per $2\sqrt{3}\times2\sqrt{3}$ supercell). The total energy of each system is stated in blue.

# REFERENCES


[1] Lee, H. C.; Liu, W.-W.; Chai, S.-P.; Mohamed, A. R.; Aziz, A.; Khe, C.-S.; Hidayah, N. S.; Hashim, U. *RSC Adv.* **2017**, *7*, 15644–15693.

[2] Novoselov, K. S.; Geim, A. K.; Morozov, S. V.; Jiang, D.; Zhang, Y.; Dubonos, S. V.; Grigorieva, I. V.; Firsov, A. A. *Science* **2004**, *306*, 666–669.

[3] Novoselov, K. S.; Jiang, D.; Schedin, F.; Booth, T. J.; Khotkevich, V. V.; Morozov, S. V.; Geim, A. K. *PNAS* **2005**, *102*, 10451–10453.

[4] Geim, A. K.; Novoselov, K. S. *Nature Mater.* **2007**, *6*, 183–191.

[5] Radisavljevic, B.; Radenovic, A.; Brivio, J.; Giacometti, V.; Kis, A. *Nature Nanotech.* **2011**, *6*, 147–150.

[6] Zeng, Z.; Yin, Z.; Huang, X.; Li, H.; He, Q.; Lu, G.; Boey, F.; Zhang, H. *Angew. Chem. Int. Ed.* **2011**, *50*, 11093–11097.

[7] Ataca, C.; Sahin, H.; Ciraci, S. *J. Phys. Chem. C* **2012**, *116*, 8983.

[8] Liu, G.-B.; Xiao, D.; Yao, Y.; Xu, X.; Yao, W. *Chem. Soc. Rev.* **2015**, *44*, 2643–2663.

[9] Tongay, S. et al. *Nat Commun* **2014**, *5*.

[10] Horzum, S.; Çakır, D.; Suh, J.; Tongay, S.; Huang, Y.-S.; Ho, C.-H.; Wu, J.; Sahin, H.; Peeters, F. M. *Phys. Rev. B* **2014**, *89*, 155433.

[11] Şahin, H.; Cahangirov, S.; Topsakal, M.; Bekaroglu, E.; Akturk, E.; Senger, R. T.; Ciraci, S. *Phys. Rev. B* **2009**, *80*, 155453.

[12] Li, L.; Yu, Y.; Ye, G. J.; Ge, Q.; Ou, X.; Wu, H.; Feng, D.; Chen, X. H.; Zhang, Y. *Nat Nano* **2014**, *9*, 372–377.

[13] Liu, H.; Neal, A. T.; Zhu, Z.; Luo, Z.; Xu, X.; Tomanek, D.; Ye, P. D. *ACS Nano* **2014**, *8*, 4033–4041.

[14] Woomer, A. H.; Farnsworth, T. W.; Hu, J.; Wells, R. A.; Donley, C. L.; Warren, S. C. *ACS Nano* **2015**, *9*, 8869–8884.

[15] Guan, J.; Zhu, Z.; Tománek, D. *Phys. Rev. Lett.* **2014**, *113*, 046804.

[16] Çakır, D.; Sevik, C.; Peeters, F. M. *Phys. Rev. B* **2015**, *92*, 165406.

[17] Çakır, D.; Sahin, H.; Peeters, F. M. *Phys. Rev. B* **2014**, *90*, 205421.

[18] Aierken, Y.; Çakır, D.; Sevik, C.; Peeters, F. M. *Phys. Rev. B* **2015**, *92*, 081408.

[19] Naguib, M.; Mochalin, V. N.; Barsoum, M. W.; Gogotsi, Y. *Adv. Mater.* **2014**, *26*, 992–1005.

[20] Sun, Y.; Chen, D.; Liang, Z. *Mater. Today Energy* **2017**, *5*, 22 – 36.

[21] Naguib, M.; Kurtoglu, M.; Presser, V.; Lu, J.; Niu, J.; Heon, M.; Hultman, L.; Gogotsi, Y.; Barsoum, M. W. *Adv. Mater.* **2011**, *23*, 4248–4253.

[22] Zha, X.-H.; Zhou, J.; Luo, K.; Lang, J.; Huang, Q.; Zhou, X.; Francisco, J. S.; He, J.; Du, S. *J. Condens. Matter Phys.* **2017**, *29*, 165701.

[23] Naguib, M.; Mashtalir, O.; Carle, J.; Presser, V.; Lu, J.; Hultman, L.; Gogotsi, Y.; Barsoum, M. W. *ACS Nano* **2012**, *6*, 1322–1331, PMID: 22279971.

[24] Zhang, C. J.; Kim, S. J.; Ghidiu, M.; Zhao, M.-Q.; Barsoum, M. W.; Nicolosi, V.; Gogotsi, Y. *Adv. Funct. Mater.* **2016**, *26*, 4143–4151.

[25] Dong, L.; Kumar, H.; Anasori, B.; Gogotsi, Y.; Shenoy, V. B. *J. Phys. Chem. Lett.* **2017**, *8*, 422–428.

[26] Siriwardane, E. M. D.; Çakır, D. *J. Appl. Phys.* **2019**, *125*, 082527.

[27] Siriwardane, E. M. D.; Karki, P.; Loh, Y. L.; Çakır, D. *J. Phys. Chem. C* **2019**, *123*, 12451–12459.

[28] Frey, N. C.; Bandyopadhyay, A.; Kumar, H.; Anasori, B.; Gogotsi, Y.; Shenoy, V. B. *ACS Nano* **2019**, *13*, 2831–2839.

[29] Khazaei, M.; Ranjbar, A.; Arai, M.; Sasaki, T.; Yunoki, S. *J. Mater. Chem. C* **2017**, *5*, 2488–2503.

[30] Balc, E.; Akkus, U. O.; Berber, S. *J. Mater. Chem. C* **2017**, *5*, 5956–5961.

[31] Naguib, M.; Gogotsi, Y. *Acc. Chem. Res.* **2015**, *48*, 128–135, PMID: 25489991.

[32] Feng, L.; Zha, X.-H.; Luo, K.; Huang, Q.; He, J.; Liu, Y.; Deng, W.; Du, S. *J. Electron. Mater.* **2017**, *46*, 2460–2466.

[33] Anasori, B.; Lukatskaya, M. R.; Gogotsi, Y. *Nat. Rev. Mater.* **2017**, *2*, 16098.

[34] Wang, L.; Zhang, H.; Wang, B.; Shen, C.; Zhang, C.; Hu, Q.; Zhou, A.; Liu, B. *Electron. Mater. Lett.* **2016**, *12*, 702–710.

[35] Halim, J.; Lukatskaya, M. R.; Cook, K. M.; Lu, J.; Smith, C. R.; Näslund, L.-A.; May, S. J.; Hultman, L.; Gogotsi, Y.; Eklund, P.; Barsoum, M. W. *Chem. Mater.* **2014**, *26*, 2374–2381, PMID: 24741204.

[36] Bos, J.-W. G. *IUCrJ* **2017**, *4*, 712–713.

[37] Sarma, S. D.; Fabian, J.; Hu, X.; Zutic, I. *EEE Trans. Magn.* **2000**, *36*, 2821–2826.

[38] Prinz, G. A. *Science* **1998**, *282*, 1660–1663.

[39] *Materials Today* **2017**, *20*, 530 – 548.

[40] Jiang, Z.; Wang, P.; Jiang, X.; Zhao, J. *Nanoscale Horiz.* **2018**, *3*, 335–341.

[41] Kumar, H.; Frey, N. C.; Dong, L.; Anasori, B.; Gogotsi, Y.; Shenoy, V. B. *ACS Nano* **2017**, *11*, 7648–7655.

[42] Wu, Z.; Yu, J.; Yuan, S. *Phys. Chem. Chem. Phys.* **2019**, *21*, 7750–7755.

[43] Sajjia, M.; Baroutaji, A.; Olabi, A. *Reference Module in Materials Science and Materials Engineering*; Elsevier, 2017.

[44] Zhang, W.-B.; Qu, Q.; Zhu, P.; Lam, C.-H. *J. Mater. Chem. C* **2015**, *3*, 12457–12468.

[45] Zhuang, H. L.; Kent, P. R. C.; Hennig, R. G. *Phys. Rev. B* **2016**, *93*, 134407.

[46] Peng, L.; Zhu, Y.; Chen, D.; Ruoff, R. S.; Yu, G. *Adv. Energy Mater.* **2016**, *6*, 1600025.

[47] Peng, L.; Fang, Z.; Zhu, Y.; Yan, C.; Yu, G. *Adv. Energy Mater.* **2017**, *8*, 1702179.

[48] Zhang, F.; Xia, C.; Zhu, J.; Ahmed, B.; Liang, H.; Velusamy, D. B.; Schwingenschlögl, U.; Alshareef, H. N. *Adv. Energy Mater.* **2016**, *6*, 1601188.

[49] Zhang, P.; Wang, F.; Yu, M.; Zhuang, X.; Feng, X. *Chem. Soc. Rev.* **2018**, *47*, 7426–7451.

[50] Pomerantseva, E.; Gogotsi, Y. *Nat. Energy* **2017**, *2*, 17089.

[51] Siriwardane, E. M. D.; Demiroglu, I.; Sevik, C.; Çakırda, D. *ACS Appl. Energy Mater.* **2019**, *2*, 1251–1258.

[52] Shukla, V.; Jena, N. K.; Naqvi, S. R.; Luo, W.; Ahuja, R. *Nano Energy* **2019**, *58*, 877 – 885.

[53] Cai, P.; He, Q.; Wang, L.; Liu, X.; Yin, J.; Liu, Y.; Huang, Y.; Huang, Z. *Ceram. Int.* **2019**, *45*, 5761 – 5767.

[54] Wen, Y.; Rufford, T. E.; Chen, X.; Li, N.; Lyu, M.; Dai, L.; Wang, L. *Nano Energy* **2017**, *38*, 368 – 376.

[55] Lukatskaya, M. R.; Bak, S.-M.; Yu, X.; Yang, X.-Q.; Barsoum, M. W.; Gogotsi, Y. *Adv. Energy Mater. 5*, 1500589.

[56] Sun, S.; Liao, C.; Hafez, A. M.; Zhu, H.; Wu, S. *Chem. Eng. J.* **2018**, *338*, 27 – 45.

[57] Echenique, P.; Alonso, J. L. *Mol. Phys.* **2007**, *105*, 3057–3098.

[58] Tew, D. P.; Klopper, W.; Helgaker, T. *J. Comput. Chem.J. Comput. Chem.* **2007**, *28*, 1307–1320.

[59] Hohenberg, P.; Kohn, W. *Phys. Rev.* **1964**, *136*, B864–B871.

[60] Kohn, W.; Sham, L. J. *Phys. Rev.* **1965**, *140*, A1133–A1138.

[61] Jones, R. O.; Gunnarsson, O. *Rev. Mod. Phys.* **1989**, *61*, 689–746.

[62] Perdew, J. P.; Wang, Y. *Phys. Rev. B* **1992**, *46*, 12947–12954.

[63] von Barth, U. *Physica Scripta T109*, 9.

[64] He, L.; Liu, F.; Hautier, G.; Oliveira, M. J. T.; Marques, M. A. L.; Vila, F. D.; Rehr, J. J.; Rignanese, G.-M.; Zhou, A. *Phys. Rev. B* **2014**, *89*, 064305.

[65] Perdew, J. P.; Ruzsinszky, A.; Csonka, G. I.; Vydrov, O. A.; Scuseria, G. E.; Constantin, L. A.; Zhou, X.; Burke, K. *Phys. Rev. Lett.* **2008**, *100*, 136406.

[66] Armiento, R.; Mattsson, A. E. *Phys. Rev. B* **2005**, *72*, 085108.

[67] Wu, Z.; Cohen, R. E. *Phys. Rev. B* **2006**, *73*, 235116.

[68] Jacob, C. R.; Reiher, M. *Int. J. Quantum Chem. 112*, 3661–3684.

[69] Kittel, C. *Introduction to Solid State Physics*, 8th ed.; Wiley, 2004.

[70] Bloch, F. *Zeitschrift fur Physik* **1929**, *52*, 555–600.

[71] Martínez-Duart, J.; Martín-Palma, R.; Agulló-Rueda, F. In *Nanotechnology for Microelectronics and Optoelectronics*; Martínez-Duart, J., Martín-Palma, R., Agulló-Rueda, F., Eds.; European Materials Research Society Series; Elsevier: Amsterdam, 2006; pp 21 – 53.

[72] Kratzer, P.; Neugebauer, J. *Front. Chem.* **2019**, *7*, 106–106.

[73] Monkhorst, H. J.; Pack, J. D. *Phys. Rev. B* **1976**, *13*, 5188–5192.

[74] Kresse, G.; Hafner, J. *Phys. Rev. B* **1993**, *47*, 558–561.

[75] Kresse, G.; Hafner, J. *Phys. Rev. B* **1994**, *49*, 14251–14269.

[76] Kresse, G.; Furthmüller, J. *Comput. Mater. Sci.* **1996**, *6*, 15–50.

[77] Kresse, G.; Furthmüller, J. *Phys. Rev. B* **1996**, *54*, 11169–11186.

[78] Phillips, J. C.; Kleinman, L. *Phys. Rev.* **1959**, *116*, 287–294.

[79] Hamann, D. R.; Schlüter, M.; Chiang, C. *Phys. Rev. Lett.* **1979**, *43*, 1494–1497.

[80] Vanderbilt, D. *Phys. Rev. B* **1990**, *41*, 7892–7895.

[81] Blöchl, P. E. *Phys. Rev. B* **1994**, *50*, 17953–17979.

[82] Kresse, G.; Joubert, D. *Phys. Rev. B* **1999**, *59*, 1758–1775.

[83] Henkelman, G.; Uberuaga, B. P.; Jónsson, H. *J. Chem. Phys.* **2000**, *113*, 9901–9904.

[84] Jungwirth, P. *Density functional Theory. A Practical Introduction. Von David Sholl and Janice A. Steckel.*; 2010; Vol. 122; pp 493–493.

[85] Zhou, Y.; Wang, Z.; Yang, P.; Zu, X.; Yang, L.; Sun, X.; Gao, F. *ACS Nano* **2012**, *6*, 9727–9736, PMID: 23057936.

[86] Siriwardane, E. M.; Karki, P.; Sevik, C.; Çakır, D. *Appl. Surf. Sci.* **2018**, *458*, 762 – 768.

[87] *Extreme Mech. Lett.* **2017**, *13*, 42 – 77.

[88] Amorim, B.; Cortijo, A.; de Juan, F.; Grushin, A.; Guinea, F.; Gutiérrez-Rubio, A.; Ochoa, H.; Parente, V.; Roldán, R.; San-Jose, P.; Schiefele, J.; Sturla, M.; Vozmediano, M. *Physics Reports* **2016**, *617*, 1 – 54, Novel effects of strains in graphene and other two dimensional materials.

[89] Lu, P.; Wu, X.; Guo, W.; Zeng, X. C. *Phys. Chem. Chem. Phys.* **2012**, *14*, 13035–13040.

[90] Kan, M.; Wang, B.; Lee, Y. H.; Sun, Q. *Nano Research* **2015**, *8*, 1348–1356.

[91] Khan, S. A.; Amin, B.; Gan, L.-Y.; Ahmad, I. *Phys. Chem. Chem. Phys.* **2017**, *19*, 14738–14744.

[92] Deniz Çakir, H. S.; Peeters, F. M. *Phys. Rev. B* **2014**, *90*, 205421.

[93] Aierken, Y.; Çakir, D.; Peeters, F. M. *Phys. Chem. Chem. Phys.* **2016**, *18*, 14434–14441.

[94] Amin, B.; Kaloni, T. P.; Schwingenschlögl, U. *RSC Adv.* **2014**, *4*, 34561–34565.

[95] Gao, G.; Ding, G.; Li, J.; Yao, K.; Wu, M.; Qian, M. *Nanoscale* **2016**, *8*.

[96] Yuan, J.; Liu, Y.; Wu, P.; Zhou, W. *J. Condens. Matter Phys.* **2018**, *30*, 305804.

[97] Anasori, B.; Xie, Y.; Beidaghi, M.; Lu, J.; Hosler, B. C.; Hultman, L.; Kent, P. R. C.; Gogotsi, Y.; Barsoum, M. W. *ACS Nano* **2015**, *9*, 9507–9516, PMID: 26208121.

[98] Liu, Z.; Zheng, L.; Sun, L.; Qian, Y.; Wang, J.; Li, M. *J. Am. Ceram.* **2014**, *97*, 67–69.

[99] Zhou, J.; Zha, X.; Zhou, X.; Chen, F.; Gao, G.; Wang, S.; Shen, C.; Chen, T.; Zhi, C.; Eklund, P.; Du, S.; Xue, J.; Shi, W.; Chai, Z.; Huang, Q. *ACS Nano* **2017**, *11*, 3841–3850, PMID: 28375599.

[100] Perdew, J. P.; Burke, K.; Ernzerhof, M. *Phys. Rev. Lett.* **1996**, *77*, 3865–3868.

[101] Perdew, J. P.; Burke, K.; Ernzerhof, M. *Phys. Rev. Lett.* **1997**, *78*, 1396–1396.

[102] Dudarev, S. L.; Botton, G. A.; Savrasov, S. Y.; Humphreys, C. J.; Sutton, A. P. *Phys. Rev. B* **1998**, *57*, 1505–1509.

[103] Krukau, A. V.; Vydrov, O. A.; Izmaylov, A. F.; Scuseria, G. E. *J. Chem. Phys.* **2006**, *125*, 224106.

[104] Baroni, S.; de Gironcoli, S.; dal Corso, A.; Giannozzi, P. *RMP* **2001**, *73*, 515–562.

[105] Zhang, B.-G., Shi-Hao; Liu *eprint arXiv:1612.02748* **2016**,

[106] Grimme, S.; Antony, J.; Ehrlich, S.; Krieg, H. *J. Chem. Phys.* **2010**, *132*, 154104.

[107] Grimme, S.; Ehrlich, S.; Goerigk, L. *J. Comput. Chem.J. Comput. Chem. 32*, 1456–1465.

[108] Castellanos-Gomez, A.; Poot, M.; Steele, G. A.; van der Zant, H. S. J.; Agaïït, N.; Rubio-Bollinger, G. *Adv. Mater.* **2012**, *24*, 772–775.

[109] Lipatov, A.; Lu, H.; Alhabeb, M.; Anasori, B.; Gruverman, A.; Gogotsi, Y.; Sinitskii, A. *Sci. Adv.* **2018**, *4*.

[110] Gomez-Navarro, C.; Burghard, M.; Kern, K. *Namo Lett.* **2008**, *8*, 2045–2049, PMID: 18540659.

[111] Fei, R.; Li, W.; Li, J.; Yang, L. *Appl. Phys. Lett.* **2015**, *107*, 173104.

[112] Yu, M.; Trinkle, D. R. *J. Chem. Phys* **2011**, *134*, 064111.

[113] Gao, G.; Ding, G.; Li, J.; Yao, K.; Wu, M.; Qian, M. **2016**, *8*.

[114] Wu, F.; Luo, K.; Huang, C.; Wu, W.; Meng, P.; Liu, Y.; Kan, E. *Solid State Commun.* **2015**, *222*, 9 – 13.

[115] Houtappel, R. *Physica* **1950**, *16*, 425 – 455.

[116] van der Marel, D.; Sawatzky, G. A. *Phys. Rev. B* **1988**, *37*, 10674–10684.

[117] Bao, J. L.; Gagliardi, L.; Truhlar, D. G. *J. Phys. Chem. Letters* **2018**, *9*, 2353–2358, PMID: 29624392.

[118] Lundberg, M.; Siegbahn, P. E. M. *J. Chem. Phys.* **2005**, *122*, 224103.

[119] Schmidt, T.; Kraisler, E.; Kronik, L.; Kümmel, S. *Phys. Chem. Chem. Phys.* **2014**, *16*, 14357–14367.

[120] Arbuznikov, A. V. *J. Struct. Chem.* **2007**, *48*, S1–S31.

[121] Farsal, D.; Snina, M.; Badia, M.; Bennai, M. *J. Supercond. Nov. Magn.* **2017**, *30*, 2187–2195.

[122] Husimi, K.; Syozi, I. *Prog. Theor. Phys.* **1950**, *5*, 177–186.

[123] Wolff, U. *Phys. Rev. Lett.* **1989**, *62*, 361–364.

[124] Editorial, *Nat. Nanotechnol.* **2018**, *13*.

[125] Han, W. *APL Materials* **2016**, *4*, 032401.

[126] Cullity, B. D.; Graham, C. D. *Introduction to Magnetic Materials*, 2nd ed.; Wiley-IEEE Press, 2008.

[127] Gong, C.; Li, L.; Li, Z.; Ji, H.; Stern, A.; Xia, Y.; Cao, T.; Bao, W.; Wang, C.; Wang, Y.; Qiu, Z. Q.; Cava, R. J.; Louie, S. G.; Xia, J.; Zhang, X. *Nature* **2017**, *546*, 265–269.

[128] Lee, I.; Utermohlen, F. G.; Weber, D.; Hwang, K.; Zhang, C.; van Tol, J.; Goldberger, J. E.; Trivedi, N.; Hammel, P. C. *Phys. Rev. Lett.* **2020**, *124*, 017201.

[129] Misiorny, M.; Hell, M.; R. Wegewijs, M. *Nat. Phys.* **2013**, *9*, 801–805.

[130] Huang, B.; Clark, G.; Navarro-Moratalla, E.; Klein, D.; Cheng, R.; Seyler, K.; Zhong, D.; Schmidgall, E.; A. McGuire, M.; Cobden, D.; Yao, W.; di, X.; Jarillo-Herrero, P.; Xu, X. *Nature* **2017**, *546*.

[131] Zhang, X.; Zhao, Y.; Song, Q.; Jia, S.; Shi, J.; Han, W. *Japanese J. Appl. Phys.* **2016**, *55*, 033001.

[132] Bonilla, M.; Kolekar, S.; Ma, Y.; Coy Diaz, H.; Sankar, V.; Das, R.; Eggers, T.; Rodriguez Gutierrez, H.; Phan, M.-H.; Batzill, M. *Nat. Nanotechnol.* **2018**,

[133] Feng, S.; Mi, W. *Appl. Surf. Sci.* **2018**, *458*, 191 – 197.

[134] Parks, J. J.; Champagne, A. R.; Costi, T. A.; Shum, W. W.; Pasupathy, A. N.; Neuscamman, E.; Flores-Torres, S.; Cornaglia, P. S.; Aligia, A. A.; Bal-

seiro, C. A.; Chan, G. K.-L.; Abruña, H. D.; Ralph, D. C. *Science* **2010**, *328*, 1370–1373.

[135] Frey, N.; Kumar, H.; Anasori, B.; Gogotsi, Y.; B. Shenoy, V. *ACS Nano* **2018**, 6319–6325.

[136] Otte, A.; Ternes, M.; von Bergmann, K.; Loth, S.; Brune, H.; Lutz, C.; Hirjibehedin, C.; Heinrich, A. The role of magnetic anisotropy in the Kondo effect. APS Meeting Abstracts. 2009; p A27.011.

[137] Zheng, H.; Zheng, J.; Wang, C.; Han, H.; Yan, Y. *J. Magn. Magn. Mater.* **2017**, *444*, 184 – 189.

[138] Luo, J.; Zhang, W.; Yuan, H.; Jin, C.; Zhang, L.; Huang, H.; Liang, C.; Xia, Y.; Zhang, J.; Gan, Y.; Tao, X. *ACS Nano* **2017**, *11*, 2459–2469, PMID: 27998055.

[139] Sevik, C.; Çak ır, D. *Phys. Rev. Applied* **2019**, *12*, 014001.

[140] Shao, Y.; Gong, P.; Pan, H.; Shi, X. *Adv. Theory Simul.* **2019**, *2*, 1900045.

[141] Marbella, L. E.; Evans, M. L.; Groh, M. F.; Nelson, J.; Griffith, K. J.; Morris, A. J.; Grey, C. P. *J. Am. Chem. Soc.* **2018**, *140*, 7994–8004, PMID: 29916704.

[142] Ling, C.; Mizuno, F. *Phys. Chem. Chem. Phys.* **2014**, *16*, 10419–10424.

[143] Houghton, T.; Eltohamy, G.; Yu, H. An Experimental Magnesium Ion Battery Cell Made of Flexible Materials. 2017 IEEE 67th Electronic Components and Technology Conference (ECTC). 2017; pp 206–211.

[144] Zhao, M.-Q.; Ren, C. E.; Alhabeb, M.; Anasori, B.; Barsoum, M. W.; Gogotsi, Y. *ACS Appl. Energy Mater* **2019**, *2*, 1572–1578.

[145] Zhu, K.; Jin, Y.; Du, F.; Gao, S.; Gao, Z.; Meng, X.; Chen, G.; Wei, Y.; Gao, Y. *J. Energy Chem.* **2019**, *31*, 11 – 18.

[146] Rakhi, R. B.; Ahmed, B.; Hedhili, M. N.; Anjum, D. H.; Alshareef, H. N. *Chem. Mater.* **2015**, *27*, 5314–5323.

[147] Du, F.; Tang, H.; Pan, L.; Zhang, T.; Lu, H.; Xiong, J.; Yang, J.; Zhang, C. J. *Electrochim. Acta* **2017**, *235*, 690 – 699.

[148] Dall'Agnese, Y.; Rozier, P.; Taberna, P.-L.; Gogotsi, Y.; Simon, P. *J. Power Sources* **2016**, *306*, 510 – 515.

[149] Zhao, M.-Q.; Ren, C. E.; Ling, Z.; Lukatskaya, M. R.; Zhang, C.; Van Aken, K. L.; Barsoum, M. W.; Gogotsi, Y. *Adv. Mater.* **2014**, *27*, 339–345.

[150] Fan, Z.; Wang, Y.; Xie, Z.; Wang, D.; Yuan, Y.; Kang, H.; Su, B.; Cheng, Z.; Liu, Y. *Adv. Sci* **2018**, *5*, 1800750.

[151] Aierken, Y.; Sevik, C.; Gűlseren, O.; Peeters, F. M.; Çakır, D. *J. Mater. Chem. A* **2018**, *6*, 2337–2345.

[152] Gong, S.; Wang, Q. *J. Phys. Chem. C* **2017**, *121*, 24418–24424.

[153] Boukhvalov, D.; Zhidkov, I.; Kukharenko, A.; Slesarev, A.; Zatsepin, A.; Cholakh, S.; Kurmaev, E. *Appl Surf Sci* **2018**, *441*, 978 – 983.

[154] Wu, Z.-S.; Winter, A.; Chen, L.; Sun, Y.; Turchanin, A.; Feng, X.; Müllen, K. *Adv. Mater.* **2012**, *24*, 5130–5135.

[155] Thirumal, V.; Pandurangan, A.; Jayavel, R.; Ilangovan, R. *Synth. Met.* **2016**, *220*, 524 – 532.

[156] Moriwake, H.; Kuwabara, A.; Fisher, C.; Ikuhara, Y. *RSC Adv.* **2017**, *7*, 36550–36554.

[157] Wang, Z.; Selbach, S. M.; Grande, T. *RSC Adv.* **2014**, *4*, 4069–4079.

[158] Bommier, C.; Ji, X.; Greaney, P. A. *Chem. Mater.* **2019**, *31*, 658–677.

[159] Tang, W.; Sanville, E.; Henkelman, G. *J. Phys. Condens. Matter* **2009**, *21*, 084204.

[160] Henkelman, G.; Jónsson, H. *J. Chem. Phys.* **2000**, *113*, 9978–9985.

[161] Shirodkar, S. N.; Kaxiras, E. *Phys. Rev. B* **2016**, *93*, 245438.

[162] Zhou, J.; Zhou, W.; Guan, C.; Shen, J.; Ouyang, C.; Lei, M.; Shi, S.; Tang, W. *China. Phys. Mech.* **2012**, *55*, 1376–1382.

[163] Shao, X.; Wang, K.; Pang, R.; Shi, X. *J. Phys. Chem. C* **2015**, *119*, 25860–25867.

[164] Demiroglu, I.; M. Peeters, F.; Gülseren, O.; Çakır, D.; Sevik, C. *J. Phys. Chem. Lett.* **2019**, *10*, 727–734.

[165] Dall'Agnese, Y.; Taberna, P.-L.; Gogotsi, Y.; Simon, P. *J. Phys. Chem. Lett.* **2015**, *6*, 2305–2309, PMID: 26266609.

[166] Sun, S.; Liao, C.; Hafez, A. M.; Zhu, H.; Wu, S. *Chem. Eng. J.* **2018**, *338*, 27 – 45.

[167] Piper, D. M.; Travis, J. J.; Young, M.; Son, S.-B.; Kim, S. C.; Oh, K. H.; George, S. M.; Ban, C.; Lee, S.-H. *Adv. Mater.* **2014**, *26*, 1596–1601.

[168] Luo, B.; Wang, B.; Li, X.; Jia, Y.; Liang, M.; Zhi, L. *Adv. Mater.* **2012**, *24*, 3538–3543.

[169] Mahmood, N.; Hou, Y. *Adv. Sci.* **2014**, *1*, 1400012.

[170] Nigar, S.; Zhou, Z.; Wang, H.; Imtiaz, M. *RSC Adv.* **2017**, *7*, 51546–51580.

[171] Wang, A.; Kadam, S.; Li, H.; Shi, S.; Qi, Y. *Npj Comput. Mater.* **2018**, *4*, 15.

[172] Thinius, S.; Islam, M. M.; Heitjans, P.; Bredow, T. *J. Phys. Chem. C* **2014**, *118*, 2273–2280.

[173] Larson, D. T.; Fampiou, I.; Kim, G.; Kaxiras, E. *J. Phys. Chem. C* **2018**, *122*, 24535–24541.

[174] Huie, M. M.; Bock, D. C.; Takeuchi, E. S.; Marschilok, A. C.; Takeuchi, K. J. *Coord. Chem. Rev.* **2015**, *287*, 15–27.

[175] Yoo, H. D.; Liang, Y.; Dong, H.; Lin, J.; Wang, H.; Liu, Y.; Ma, L.; Wu, T.; Li, Y.; Ru, Q. e. a. *Nat. Commun.* **2017**, *8*, 339.

[176] Li, Y.-M.; Guo, Y.-L.; Jiao, Z.-Y. *Curr. Appl. Phys.* **2020**, *20*, 310 – 319.

[177] Wang, Y.; Zhou, M.; Xu, L.-C.; Zhao, W.; Li, R.; Yang, Z.; Liu, R.; Li, X. *J. Power Sources* **2020**, *451*, 227791.

[178] Xie, Y.; Dall'Agnese, Y.; Naguib, M.; Gogotsi, Y.; Barsoum, M. W.; Zhuang, H. L.; Kent, P. R. C. *ACS Nano* **2014**, *8*, 9606–9615, PMID: 25157692.

[179] Meng, Q.; Ma, J.; Zhang, Y.; Li, Z.; Zhi, C.; Hu, A.; Fan, J. *Nanoscale* **2018**, *10*, 3385–3392.

[180] Lee, S.; Jung, S. C.; Han, Y.-K. *Nanoscale* **2020**, –.

[181] Wang, Y.; Shen, J.; Xu, L.-C.; Yang, Z.; Li, R.; Liu, R.; Li, X. *Phys. Chem. Chem. Phys.* **2019**, *21*, 18559–18568.

[182] Mehta, V.; Saini, H. S.; Srivastava, S.; Kashyap, M. K.; Tankeshwar, K. *J. Phys. Chem. C* **2019**, *123*, 25052–25060.

[183] Gandi, A. N.; Alshareef, H. N.; Schwingenschlögl, U. *Chem. Mater.* **2016**, *28*, 1647–1652.

[184] Champagne, A.; Shi, L.; Ouisse, T.; Hackens, B.; Charlier, J.-C. *Phys. Rev. B* **2018**, *97*, 115439.

[185] Sun, X.; Gao, Y.; Zhao, C.; Deng, S.; Zhong, X.; Zhuang, G.; Wei, Z.; Wang, J.-g. *Adv.Theory Simul. 2*, 1800158.

[186] Shannon, R. D. *Acta Cryst. Section A* **1976**, *32*, 751–767.

[187] van de Walle, A. *Calphad* **2009**, *33*, 266–278.

[188] van de Walle, A.; Asta, M. D.; Ceder, G. *Calphad* **2002**, *26*, 539–553.

[189] van de Walle, A.; Ceder, G. *J. Phase Equilib.* **2002**, *23*, 348–359.

[190] Kurahashi, S.; Arabnejad, S.; Ushiyama, H.; Yamashita, K. *Journal of Computer Chemistry, Japan* **2019**, *18*, 84–94.

[191] Çakır, D.; Sevik, C.; Gülseren, O.; Peeters, F. M. *J. Mater. Chem. A* **2016**, *4*, 6029–6035.

[192] Eames, C.; Islam, M. S. *J. Am. Chem. Soc.* **2014**, *136*, 16270–16276, PMID: 25310601.

[193] Xie, Y.; Naguib, M.; Mochalin, V. N.; Barsoum, M. W.; Gogotsi, Y.; Yu, X.; Nam, K.-W.; Yang, X.-Q.; Kolesnikov, A. I.; Kent, P. R. C. *J. Am. Chem. Soc.* **2014**, *136*, 6385–6394, PMID: 24678996.

[194] Zhao, T.; Zhang, S.; Guo, Y.; Wang, Q. *Nanoscale* **2016**, *8*, 233–242.

[195] *Materials Today* **2015**, *18*, 252 – 264.

[196] Shukla, V.; Jena, N. K.; Naqvi, S. R.; Luo, W.; Ahuja, R. *Nano Energy* **2019**, *58*, 877 – 885.

[197] Zhu, J.; Chroneos, A.; Eppinger, J.; Schwingenschlögl, U. *Appl. Mater. Today* **2016**, *5*, 19 – 24.

[198] Yang, Z.; Choi, D.; Kerisit, S.; Rosso, K.; Wang, D.; Zhang, J.; Graff, G.; Liu, J. **2009**,

[199] Luo, J.; Zhang, W.; Yuan, H.; Jin, C.; Zhang, L.; Huang, H.; Liang, C.; Xia, Y.; Zhang, J.; Gan, Y.; Tao, X. *ACS Nano* **2017**, *11*, 2459–2469.

[200] Simon, P. *ACS Nano* **2017**, *11*, 2393–2396.

[201] Rao, C. N. R.; Pramoda, K.; Kumar, R. *Chem. Commun.* **2017**, *53*, 10093–10107.

[202] Pomerantseva, E.; Gogotsi, Y. *Nat. Energy* **2017**, *2*, 17089.

[203] Xu, M.; Lei, S.; Qi, J.; Dou, Q.; Liu, L.; Lu, Y.; Huang, Q.; Shi, S.; Yan, X. *ACS Nano* **2018**, *12*, 3733–3740.

[204] Boota, M.; Pasini, M.; Galeotti, F.; Porzio, W.; Zhao, M.-Q.; Halim, J.; Gogotsi, Y. *Chem. Mater.* **2017**, *29*, 2731–2738.

[205] Hu, T.; Li, Z.; Hu, M.; Wang, J.; Hu, Q.; Li, Q.; Wang, X. *J. Phys. Chem. C* **2017**, *121*, 19254–19261.

[206] Xie, Y.; Naguib, M.; Mochalin, V. N.; Barsoum, M. W.; Gogotsi, Y.; Yu, X.; Nam, K.-W.; Yang, X.-Q.; Kolesnikov, A. I.; Kent, P. R. C. *J. Am. Chem. Soc.* **2014**, *136*, 6385–6394.

[207] Byeon, A.; Zhao, M.-Q.; Ren, C. E.; Halim, J.; Kota, S.; Urbankowski, P.; Anasori, B.; Barsoum, M. W.; Gogotsi, Y. *ACS Appl. Mater. Interfaces* **2017**, *9*, 4296–4300.

[208] Come, J.; Black, J. M.; Lukatskaya, M. R.; Naguib, M.; Beidaghi, M.; Rondinone, A. J.; Kalinin, S. V.; Wesolowski, D. J.; Gogotsi, Y.; Balke, N. *Nano Energy* **2015**, *17*, 27 – 35.

[209] Er, S.; Suh, C.; Marshak, M. P.; Aspuru-Guzik, A. *Chem. Sci.* **2015**, *6*, 885–893.

[210] Monkhorst, H. J.; Pack, J. D. *Phys. Rev. B* **1976**, *13*, 5188–5192.

[211] Tang, W.; Sanville, E.; Henkelman, G. *J. Phys.: Condens. Matter* **2009**, *21*, 084204.

[212] Sanville, E.; Kenny, S. D.; Smith, R.; Henkelman, G. *J. Comp. Chem.* **2007**, *28*, 899.

[213] Henkelman, G.; Arnaldsson, A.; Jónsson, H. *Comput. Mater. Sci.* **2006**, *36*, 254.

[214] Parrinello, M.; Rahman, A. *Phys. Rev. Lett.* **1980**, *45*, 1196–1199.

[215] Parrinello, M.; Rahman, A. *J. Appl. Phys.* **1981**, *52*, 7182–7190.

[216] Hernandez, E. *J. Chem. Phys.* **2001**, *115*, 10282–10290.

[217] Wang, A.; Kadam, S.; Li, H.; Shi, S.; Qi, Y. *Npj Comput. Mater.* **2018**, *4*, 15.

[218] Ohzuku, T.; Iwakoshi, Y.; Sawai, K. *J. Electrochem. Soc* **1993**, *140*, 2490–2498.

[219] Aydinol, M. K.; Kohan, A. F.; Ceder, G.; Cho, K.; Joannopoulos, J. *Phys. Rev. B* **1997**, *56*, 1354–1365.

[220] Çakır, D.; Sevik, C.; Gulseren, O.; Peeters, F. M. *J. Mater. Chem. A* **2016**, *4*, 6029–6035.

[221] Zhang, H.; Fu, Z.; Zhang, R.; Zhang, Q.; Tian, H.; Legut, D.; Germann, T. C.; Guo, Y.; Du, S.; Francisco, J. S. *Proc. Natl. Acad. Sci. U. S. A.* **2017**, *114*, E11082–E11091.

[222] Thinius, S.; Islam, M. M.; Heitjans, P.; Bredow, T. *J. Phys. Chem. C* **2014**, *118*, 2273–2280.

[223] Tritsaris, G. A.; Zhao, K.; Okeke, O. U.; Kaxiras, E. *J. Phys. Chem. C* **2012**, *116*, 22212–22216.

[224] Lunell, S.; Stashans, A.; Ojamae, L.; Lindstrom, H.; Hagfeldtm, A. *J. Am. Chem. Soc.* **1997**, *119*, 7374–7380.

[225] Lindstram, H.; Sadergren, S.; Solbrand, A.; Rensmo, H.; Hjelm, J.; Hagfeldt, A.; Lindquist, S.-E. *J. Phys. Chem. B* **1997**, *101*, 7710–7716.

[226] Olson, C. L.; Nelson, J.; Islam, M. S. *J. Phys. Chem. B* **2006**, *110*, 9995–10001.